Numerical Study of Flow Alteration Techniques and High Temperature Effects at Supersonic/Hypersonic Speeds

A Thesis Report Submitted in Partial Fulfillment of the Requirements

for the Degree of

DOCTOR OF PHILOSOPHY

by

SIDDESH DESAI

Roll No : 146103026

Department of Mechanical Engineering

Indian Institute of Technology Guwahati

Guwahati - 781039

March 2019

CERTIFICATE

It is certified that the work contained in the thesis entitled, "**Numerical Study of Flow Alteration Techniques and High Temperature Effects at Supersonic/Hypersonic Speeds**", submitted by Siddesh Desai, in the Department of Mechanical Engineering, Indian Institute of Technology Guwahati, India, for the award of degree of Doctor of Philosophy has been carried out under our supervision and that this work has not been submitted elsewhere for the award of any other degree or diploma.

Dr. Vinayak Kulkarni
Associate Professor
Department of Mechanical Engineering
Indian Institute of Technology Guwahati

Dr. Ganesh Natarajan
Associate Professor
Department of Mechanical Engineering
Indian Institute of Technology Guwahati

DECLARATION

I declare that,

1. The work contained in this thesis is original and has been done by me under the guidance of my supervisors.
2. The work has not been submitted to any other institute for any degree or diploma.
3. I have followed the guidelines provided by the institute in preparing this thesis.
4. I have confirmed to the norms and guidelines given in the ethical code of conduct of the institute.
5. Whenever I used materials (data, theoretical analysis, figures and text) from other sources, I have given their detail in references.

Signature of student
Siddesh Desai

ACKNOWLEDGEMENT

"Starting something can be easy; it is finishing that is the highest hurdle". The journey of doctoral study is always a difficult and challenging task. Throughout this long journey, I have gained a lot by learning to persevere despite hardship. I would never have successfully completed this thesis without the assistance of numerous people who I am indebted to. Their direction, advice, support and contributions have proved invariable along the way.

First and foremost, I would like to express my special appreciation and respect to my supervisors, Dr. V. Kulkarni and Dr. G. Natarajan, who have been a tremendous mentors for me. I appreciate all their contributions of time, ideas and funding to make my PhD experience productive and stimulating. I am also thankful to them for the excellent example he has provided as a successful research scientist and professor. The joy and enthusiasm they have for their research were contagious and motivational for me, even during the tough times in my PhD pursuit. A very special gratitude goes to them for encouraging my research. Thank you very much, sir, for your advice on my research, my career, as well as my personal life, has always been priceless.

I offer my sincere thanks to my doctoral committee members, Professor A. K. Das, Dr. D. N. Basu, Dr. B. Mehta and Dr. H. Sharma for their insightful comments and encouragement, and also for the hard questions which incented me to widen my research from various perspectives.

I am also fortunate and grateful to receive guidance from Professor Dr. N. Sahoo and Dr. H. Gadgil (IIT Bombay). It was fantastic to have the opportunity to work with them through various collaborations and their valuable suggestions and concise comments have always been a source of inspiration to me. With their expertise and in-depth knowledge in my field of research, they had given various suggestions which brought my thesis work in good shape.

My sincere gratefulness to past and present departmental heads Professor A. K. Dass and Professor S. K. Dwivedy for their kind permission for enrollment, registration and several important supports at IIT Guwahati.

"A good friend is like a four leaf clover hard to find and lucky to have", I have been fortunate to be surrounded myself by some amazing friends, Mukesh, Jitendra, Kalpa, Parag, Arun, Shyam, Sumit, Shuvayan, Snehasish, Saoumya, Saibal, Himanshul, Saurabh, Anshul, Shatrughan, Vaibhav and Rajendra. Thank you all for your support and encouragement. Special thanks are also due to Anamika mam, Swapnali mam, Professor S.N. Bora, Das Sir, Bhola, Pratik, Praveen, Naman, Nayan, Rachit, Prashant, Shahnawaz, Purushottam, Uttam, Yashwardhan who made my PhD journey a memorable

one. Also, I am grateful to few amazing talented friends Subrat, Anand, Shaym, Basant, Pankaj, Pandey, Kishor, Shatru, Rajendra, Mukul, Anand and all other group members of Badminton Freaks for the beautiful evenings and keeping me healthy and physically fit.

It is my pleasure to acknowledge the help provided by my seniors, juniors and internship students, especially, Bibin, Prabhash, Vishnu, Jubajyoti, Jay, Shobhit, Piyush, Shailendra and all other lab members from our lab.

"The love of a family is life's greatest blessings". In this precious moment of my life, I would like to express my deep sense of gratitude to my parents, Late Mr. Satish Kumar Desai and Mrs. Sarita Desai for their love, blessings and constant encouragement throughout my life. I would like to thanks my sister Suchita Desai Mone and brother in law Nikhil Mone for their love and best wishes. Without their support it would have been very difficult to finish my PhD work. I am deeply in debt to my family and friends for the sacrifices they have borne to ensure the fulfillment of my dreams. Next, I would like to express my special sense of gratitude to my grand parents Mr. Manohar Deodhar and Mrs. Nalini Deodhar. I am also greatful to Shrikant Mone, Kalpana Mone, Sudhir Deodhar, Bhageshri Deodhar, Padmini Godse, Abhay Godse, Hrishikesh Khare, Yogesh Khare, Agrawal uncle, Varsha vaidya, Pramod Vaidya, Prasad Deodhar, Teju Deodhar, Vidyanand Deodhar, Bharti Deodhar, Nisha Desai, Neelam Korde, Ujwala Desai, Milind Barway and Rajeshri Barway. I want to offer my sincere gratitude to all of you. You have always been inspiring, supporting and teaching me to understand the true value of human life.

Siddesh Desai

ABSTRACT

The flying object encountering supersonic/hypersonic stream would commonly deal with issues like excessive wave drag force, shock wave boundary layer interaction and high-temperature effects. Hence, efficient high-speed structure design demands the solution for such flow complexities. Computational fluid dynamics is evolved as an efficient tool to achieve it. Hence, present work is focused on the numerical investigation of above mentioned flow problems and subsequent implementation of flow alteration techniques to mitigate their adverse effect. Therefore, a finite-volume based multi-species reacting gas unstructured solver is developed in-house. It solves coupled 2-D axisymmetric Navier-Stokes equations along with the species continuity equations. Additionally, perfect and frozen versions of this solver have also been wielded to highlight the role of high-temperature effects in the flowfield alteration as well as to simulate low enthalpy flowfield. Prior to the detailed investigations, the solver is validated for the variety of literature reported cases including flow past a cylinder, flow over a sphere, unsteady shock tube flow problem, counter jet drag reduction technique and ramp induced shock wave boundary layer interaction.

The initial study deals with the examination of real gas effects for the cases of unsteady shock tube flow and steady flow over a cylinder/sphere. It is found that, for a given driver to driven pressure ratio real gas effects modified the shock propagation speed in the shock tube. These effects also alter the shock stand-off distance and shock shape for flow past a cylinder/sphere at same freestream Mach number but at high enthalpy condition. Hence, the study portrays the limitation of the different governing parameters in deciding the flow features for both the cases in the presence of high-temperature effects.

Further, the investigation is continued to asses the energy deposition based flow alteration technique for drag reduction. Perfect gas, frozen and reacting flow solvers are employed to simulate hypersonic flow past a blunt body. The study shows that deposited energy offers more power effectiveness in case of perfect gas flow while degradation in power is seen for reacting gas flow model which is attributed to real gas effects. Apart from these, the deviation in drag obtained for frozen and reacting flows is also noted only for higher absolute energy deposition. Moreover, the study also reveals that required non-dimensional critical energy to obtain the maximum power effectiveness at different enthalpies lies in a narrow range. Further, prominent real gas effects with increment in freestream stagnation enthalpy have shown up to 74 % reduction of power effectiveness for the reacting gas case as compared to the perfect gas case.

In further studies, the aerodynamics of drag reduction using steady-state counter jet is investigated. Here, efforts are made to review the various literature reported aerodynamic

influencing parameters like jet to freestream total pressure ratio, jet to body area ratio, the combination of the jet to freestream total pressure ratio and flux etc. The study revealed the limitations of these parameters in deciding various key features like shock stand-off distance, shock reattachment location, Mach disk location, its size etc. In view of this, a new non-dimensional number is suggested which is jet to freestream momentum ratio. The rigorous theoretical and numerical examination demonstrated that the jet to freestream momentum ratio is the vital deciding number which governs the various flow characteristics of steady-state opposing jet based drag reduction technique.

Later, efforts are also given towards mitigating the boundary layer separation in the presence of shock wave boundary layer interaction. In order to do that, flow alteration techniques like pressure feedback as well as blunt leading edge are considered herein. The studies showed significant reduction of separated region size using pressure feedback technique (PFT). It is also found that cooling of the feedback channel can further increase its potential of separation control. Here, cooling of the channel up to 175 K reduced the separation size by 18.18 % while 50 K channel provided 30 % reduction. Studies with different ramp angle showed that high ramp angle leads to the lower effectiveness of PFT albeit higher mass flow rate through the feedback channel. Apart from these, more controllability is obtained at high freestream enthalpy simulations performed using reacting gas flow solver compared to low freestream enthalpy. Later, the blunt leading edge is integrated along with the cooled PFT to improve its effectiveness. It is found that the integrated arrangement reduced the value of critical blunt radii (inversion and equivalent) without altering the entropy layer.

The investigations are extended to study the passive control of SWBLI using the leading edge bluntness alone for perfect and reacting gas models. For precise computation of blunt critical radii (inversion and equivalent), the in-house developed solvers are integrated with the gradient-based optimization algorithm. Here, the perfect gas simulation estimated inversion and equivalent radii to be 0.84 mm and 1.95 mm while same for the reacting case are 0.781 mm and 1.85 mm. At any blunt radius value, real gas effects reduced SWBLI induced boundary layer separation size compared to perfect gas flow. This assistance provided by real gas effects also reduced the requirement of high entropy layer thickness and over-pressure region ahead of the interaction zone. In the investigation, the criteria of inversion radius about having high entropy layer thicker than the boundary layer, around the upstream influence location, is marked independent of gas flow model to achieve inversion blunt leading edge radius. Thus, it can be concluded that only perfect gas simulations are sufficient to predict the critical radii to ensure separation control.

CONTENTS

LIST OF FIGURES

LIST OF TABLES

ABBREVIATIONS

BWT	-	Blast wave theory
CFD	-	Computational fluid dynamics
FVM	-	Finite volume method
GM	-	Gradient based method
HEL	-	High entropy layer
LPM	-	Long penetration mode
PFT	-	Pressure feedback technique
R-SWBLI	-	Ramp induced shock wave boundary layer interactions
SPM	-	Short penetration mode
SWBLI	-	Shock wave boundary layer interactions
USHAS	-	Unstructured solver for hypersonic aerothermodynamic simulations

NOMENCLATURE

A_s - Projected area of sphere (m^2)
A - Jet exit to body area ratio
C_d - Drag coefficient
C_f - Skin-friction coefficient
C_i - Mass concentration of species i (kg/m^3)
C_p - Pressure coefficient
C_{pi} - Specific heat of species i at constant pressure (J/kmolK)
D - Drag (N)
D_O - Drag for the case of without energy addition (N)
dx - Feedback channel size (mm)
D_{im} - Effective binary diffusivity of species i (5×10^{-5} m^2/s)
E - Total energy (J/kg)
e - Internal energy (J/kg)
e_i - Internal energy of species i (J/mol)
E_I - Convective flux vector in x direction
F_I - Convective flux vector in y direction
E_v - Viscous flux vector in x direction
F_v - Viscous flux vector in y direction
h^0_{fi} - Heat of formation of species i (J/mol)
h_i - Specific enthalpy of species i (J/(kg))
H_o - Free stream stagnation enthalpy (J/kg)
k - Conductivity (W/(m K))
L - Location of energy spot from stagnation point (mm)
MW_i - Molecular weight of species i
P - Power effectiveness
p - Pressure (N/m^2)
P_1 - Pressure feedback technique injection pressure (N/m^2)
P_2 - Pressure feedback technique suction pressure (N/m^2)
Q - Strength of energy spot (W)
Q_n - Non dimensional strength of energy spot ($Q/\rho_\infty A_s U_\infty H_o$)
q_x - Heat flux in x direction (W/m^2)
q_y - Heat flux in y direction (W/m^2)

r	-	Radius of energy spot (mm)
R, R_b	-	Leading edge radius or radius of sphere (mm)
Re	-	Reynolds number
R_{mA}	-	Jet to freestream momentum ratio
R_P	-	Jet to freestream pitot pressure ratio
R_u	-	Universal gas constant (J/kmolK)
S_I	-	Inviscid axisymmetric source term
S_i	-	Species production rate (kg/m^{3}s)
S	-	Source term vector
S_v	-	Viscous axisymmetric source term
t	-	Time (s)
T	-	Temperature (K)
t	-	Time (s)
T_c	-	Pressure feedback channel wall temperature (K)
T_R	-	Reference temperature for thermodynamic properties (K)
T_{wall}	-	Ramp wall temperature (K)
T_∞	-	Free stream temperature (K)
X	-	X-coordinate (m)
Y	-	Y-coordinate (m)
Y_i	-	Mass fraction of species i
U	-	Conserved variable vector
u	-	Velocity in x direction (m/s)
U_∞	-	Freestream velocity (m/s)
v	-	Velocity in y direction (m/s)
$\overline{u}_{\ i}$	-	Diffusion velocity in x direction (m/s)
$\overline{v}_{\ i}$	-	Diffusion velocity in y direction (m/s)
α	-	Constant ($\alpha = 1$ for 2-D axisymmetric, $\alpha = 0$ for 2-D problem)
ρ	-	Density (kg/m^3)
ρ_∞	-	Freestream density (kg/m^3)
Δ_s	-	Shock layer thickness (mm)
$\tau_{xx}, \tau_{xy}, \tau_{yy}, \tau_{\theta\theta}$	-	Shear stress components (N/m^2)
θ	-	Angle (deg)
μ	-	Viscosity (N s/m^2)

Dedicated to my Father

CHAPTER 1

INTRODUCTION

The past vision to fly like a bird revolutionized today's meaning of civil transport. This dream not only changed the old false notions but also guided the human being to reach out to other planets and explore the life possibilities on them. In the past, the desire to mimic the bird flight motivated human being to attach the feather like wings to hands. Soon after many flying failures, lack of comprehension of fundamentals was realized. Later, the right direction to the aspirations was provided by Aristotle, Archimedes and various others by developing different theories. All the present achievements are possible only after years of devotions and efforts of many researchers.

A realistic thought of designing the flying machines began with the creation of "Ornithopter" drawings of Leonardo da Vinci. His foresight provided an extra thrust to research in this realm. Nevertheless, the first manned flight was registered with the invention of balloons in 1783. This advancement was followed by the introduction of Glider. Later on, Sir George Cayley proposed the concept of modern fixed-wing aircraft and he was the first person to recognize the need of a separate propulsion system for flight. Following this, on December 17, 1903, the first successful flight of powered aircraft was recorded which was developed by Wilbur and Orville Wright. This milestone helped to gain the confidence of flying, however, the thirst to fly faster was still unquenched. As an outcome, the first supersonic flight took off in 1947. This also fueled the human aspiration to reach out of the earth atmosphere and the moon mission was accomplished in 1969.

These achievements required the conceptual understanding of various flow regimes like the subsonic, transonic, supersonic and hypersonic flow in order to develop a superior space vehicle. Each of these flow regimes has different flow characteristics and dynamics. These regimes can be well differentiated by the value of flow Mach number. Conventionally supersonic flows have Mach number more than 1. But, the hypersonic

flow is said to be attained only when certain flow features become prominent. Still, in general, if freestream Mach number is more than 5 then flow is regarded as hypersonic. The main features of this flow regime are viscous interaction, entropy layer, thin shock layer, high-temperature flows etc. All high-speed vehicles, missiles, rockets have to encounter some or all of these zones during a flight between launching station and destination. It involves many formidable complications like shock wave boundary layer interaction, excessive drag force, high-temperature effects, surface heating problem etc. Each phenomenon is equally important and may lead to complete design failure if neglected. Therefore, these concerns are important not only to study but also to design a safe and cost-effective flight. Hence, these complications are discussed in the following sections in detail.

1.1 High temperature effects

High temperature effects may play a decisive role in the flowfield modifications. But in the most simplified modeling, gas is treated as perfect gas with negligible inter-molecular forces. In addition, the gas is also termed as a calorically perfect at low temperatures where its specific heat ratio remains constant. This approximation holds good in the prediction of flowfield parameters for many aerospace applications like a missile, reusable launch vehicle, supersonic aircraft etc. However, the deviation from calorically perfect gas behaviour can be noticed for the temperature higher than 800 K (at 1 atm). This deviation crosses another stage mostly in hypersonic streams encountered by space vehicles. In this stage, the acquired high temperature, due to strong shock wave leads to extreme viscous dissipation, dissociation, ionization and even radiation.

Here, the high kinetic energy of the freestream gets converted into the internal energy and results in huge post-shock temperature. Further, it leads to vibrational excitation of the gas molecules. Then, the sufficient number of collisions also initiate the dissociation reactions in order to break the molecules to form new atoms or molecules at a finite rate. It means fluid requires time to complete the reactions and to acquire a final chemical composition at the equilibrium state. But, in this phase, the gas may remain in a chemical non-equilibrium state, downstream of the shock, and may reach to equilibrium state far downstream of the space vehicle. Thus it results in the variation of the thermophysical properties like specific heat, viscosity, thermal conductance in conjunction with gas species composition. Moreover, the presence of free electrons attributed to the ionized air may even cause the blackout situation where communication from the space vehicle is too difficult. All these effects are collectively referred to "real gas effects" or "high-temperature effects". The importance of considering the high temperature effects

can be illustrated by taking an example of Apollo lunar reentry vehicle for normal shock calculations corresponding to 53 km altitude. The predicted shock layer temperature is 58,128 K using calorically perfect gas assumption at freestream Mach number of 32.5 and temperature of 283 K. However, this estimation considering real gas effects is 11,600 K which is very close to realistic temperature. Therefore, these effects must be accounted for precise estimation of various essential flowfield parameters. The range of dissociation and ionization reactions for air at 1 atm pressure is illustrated in Fig. 1.1.

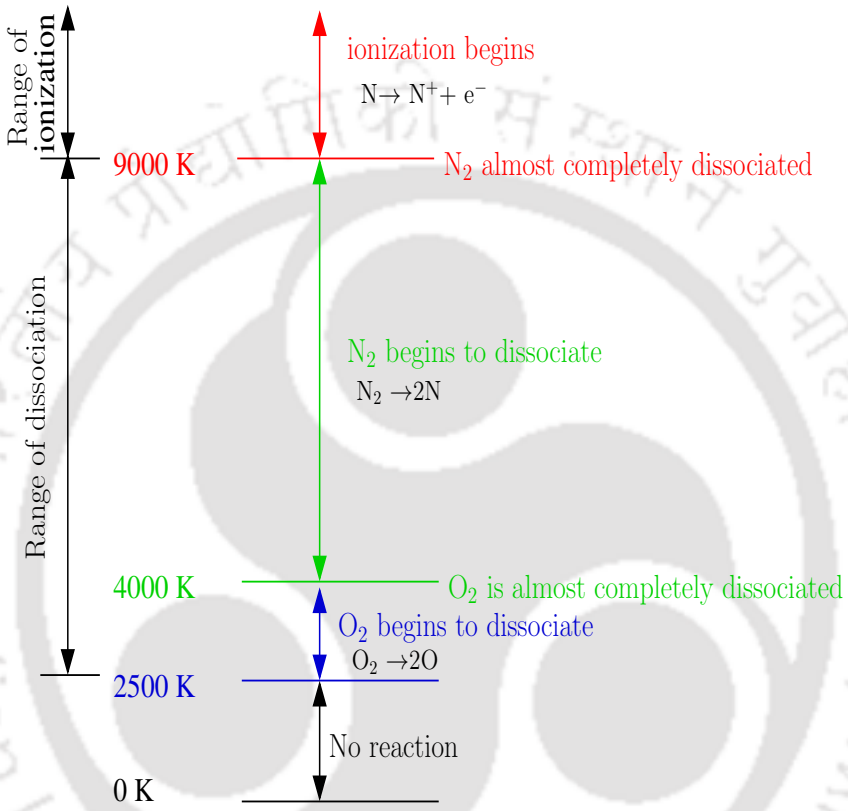

Figure 1.1: Ranges of various high temperature aspects of air (1 atm)

It clearly depicts that the air becomes chemically reacting with the increment in temperature. In particular, different types of reacting flow are possible which can be categorized by the response of chemical reactions in a gas. These are specified as:-

Frozen flow

In the frozen flow, the reaction rates are very slow and hence, the fluid does not experience any change in chemical composition while flowing. Therefore, fluid may pass over the vehicle before reactions get triggered.

Equilibrium flow

Here, very fast reaction rates cause the flowing fluid to attain the equilibrium composition at a local temperature and pressure condition. Thus, fluid shows immediate change in the properties in the flowfield. In other words, reactions in a fluid flow get activated and

end over a very small distance of travel. Here, forward and backward reaction rates of chemical reactions are equal.

Non-equilibrium flow

Previously classified flows are two extreme conditions and phenomenon in between these are too complicated. The flow is referred as a chemical non-equilibrium flow when the forward and backward reaction rates are not equal in certain portions of flowing fluid. In other words, the flowing fluid continues to chemically react while flowing over the space-craft and hence the initiated reactions remain incomplete in the flowfield. On the other hand, if different energy modes are in non-equilibrium and therefore, the nonunique temperature is present then flow is called to be in thermal non-equilibrium. Hence, the flow could be in thermal as well as in chemical non-equilibrium in the flowfield.

1.1.1 Different reactions in external hypersonic aerodynamics

Following are different possible reactions in the high temperature flow of air:-

Dissociation reaction

Dissociation is an endothermic reaction in which a molecule breaks into one or more than one smaller atoms or molecules or both. For example, when temperature of air reaches 2500 K (1 atm pressure), molecule of O_2 breaks and forms atoms of O.

$$O_2 + O_2 \rightarrow 2O + O_2$$

Ionization reaction

Ionization can result from collision of an atom or molecule with the other atom or molecule, or by interaction with light. It is the process in which molecule acquires positive or negative charge by loosing or gaining electrons. In air when temperature is more than 9000 K at 1 atm pressure then reactions like ionization of nitrogen can be noticed.

$$N \rightarrow N^+ + e^-$$

1.2 Drag mitigation

High wave drag and immense surface heating rate are another conventional hurdles in achieving the cost-efficient hypersonic flight. In the 1950s, it was found in studies that the stagnation point heat flux is inversely related to the square root of the nose radius. Hence, to alleviate heating, blunt nose shape was proposed. Therefore, many reentry vehicles like VOSTOK and Apollo Command Module (Apollo-CM) were designed with blunt nose shape. However, the penalty was paid in terms of increased wave drag. In fact,

rendering bluntness keeps the shock away from the object. Thus, high shock strength and low stand-off distance lead to dissipation of a large amount of kinetic energy of gas to the shock layer gas. As an outcome of this, more energy gets invested in heating the shock layer rather than the body. Consequently, wall heat flux gets reduced at the cost of high drag force. Here, a significant part of the drag is contributed by the wave drag. Therefore, many active and passive wave drag reduction techniques have been proposed by various research groups. All these methods adjust the external flowfield and change the effective body shape such that it reduces not only the wave drag but the heat transfer as well. Hence, by implementing these methods, the aim of economical flight can be achieved by increasing the payload, reducing fuel consumption and by boosting the range in the same flowfield. Some of the drag mitigation approaches are briefly described in the following section.

Aero-spike

In this method, a spike structure is mounted on the nose of the blunt body/space vehicle that protrudes out as shown in Fig. 1.2. This simple passive structural modification leads to the replacement of strong bow shock by weak conical shocks and formation of the recirculation region ahead of the body. Here, recirculation region results in a significant fore-body pressure reduction in the nose region and hence the overall wave drag. An example of the effectiveness of this method is UGM-96 Trident I ballistic missile in which increment in the range was registered up to 530 km. Moreover, aero-spike can be retracted any time on the body as per the aerodynamic requirement. However, extreme viscous dissipation may cause severe heating of spike such that it can ablate. Thus, although it is simple to implement, it is less favoured by various research groups.

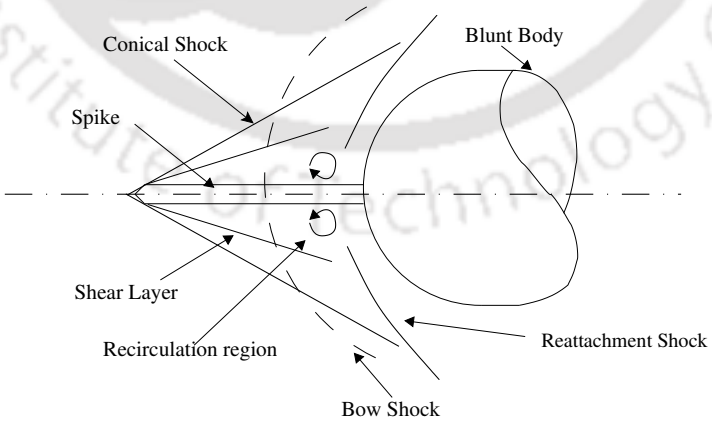

Figure 1.2: Schematic of aero-spike based drag reduction technique

Energy deposition

In order to meet the drag mitigation challenges, another technique was proposed. It is an active method which may use energy in the form of the electromagnetic wave, laser, microwave, electric arc discharge etc. In this method, upstream energy deposition acts as a source of disturbance in the supersonic stream as shown in Fig. 1.3. Consequently, it leads to shock recasting and further lowering of the surface pressure. Using this method, propulsive power can be markedly saved at the cost of some power required to deposit in the freestream. It is also helpful in controlling the vehicle and sonic boom mitigation.

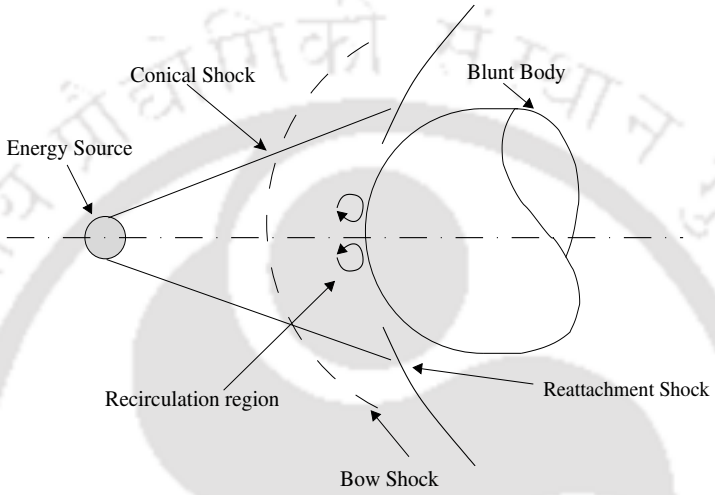

Figure 1.3: Schematic of energy deposition based drag reduction technique

Counter jet injection

Another convincing drag reduction approach is the counter jet injection. As the name suggests, in this active method, a secondary flow opposing the supersonic or hypersonic mainstream is introduced from the stagnation point of the body as shown in Fig. 1.4. The resultant interaction between the opposing jet and the incoming stream leads to shock reframing. Thus a low-pressure dead air region surrounds the body. Moreover, the deflected jet also acts as a heat blanket for the space vehicle and subsequently reduces surface heating rate. The performance of this method is highly dependent on the jet exit to freestream total pressure ratio. For low total pressure ratio, the flow structure turns unsteady while high total pressure ratio is required to attain a steady state.

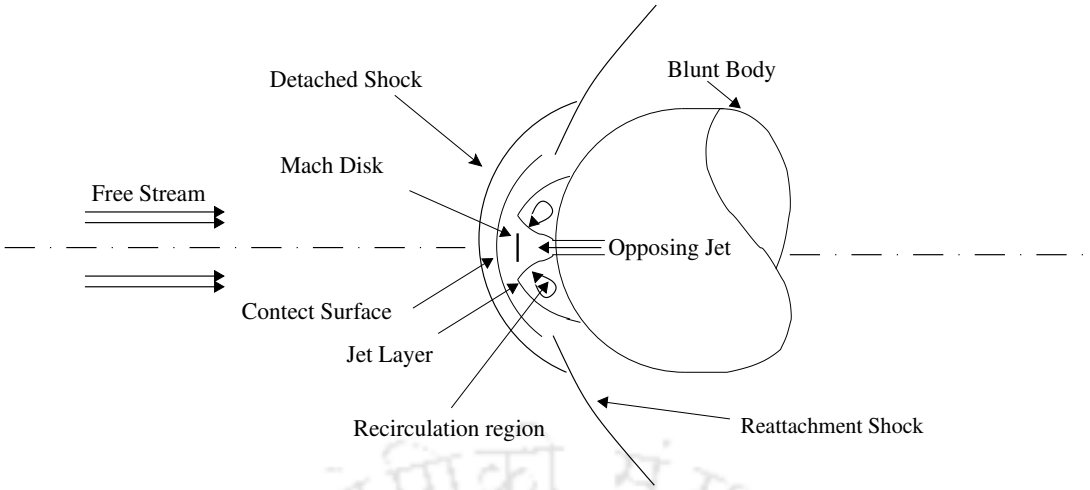

Figure 1.4: Schematic of counter jet drag reduction technique

1.3 Shock wave boundary layer interaction (SWBLI)

Inevitable appearance of the shock wave and boundary layer interaction is one of the prime concerns to the aerodynamicist. This phenomenon may arise in many internal and external regions of the high-speed vehicle like air-breathing engine's intake, turbine, wing-body junction, after-body tail, nozzle, compressor, deflected control surface and also in helicopter blades, missile components etc. The SWBLI may harm the overall safety and performance of high-speed object as it has a detrimental impact on various design parameters. These include severe heat flux, wall pressure redistribution, transition to turbulence, unsteadiness, boundary layer readjustment etc.

Therefore, it is vital to unleash its flow physics which begin from the study of the boundary layer formation. It is known that the boundary layer gets formed when fluid comes into contact with the surface as a result of near wall viscous action. Apart from the boundary layer, supersonic or hypersonic flows have shock wave due to turning the stream into itself in presence of the obstruction. Across the shock wave, flow properties like pressure, temperature, density, Mach number etc. experience abrupt jump. The inviscid shock may interact with the boundary layer by means of shock impingement, ramp obstruction, normal shock etc. Among these, ramp induced SWBLI resembles various shock induced separated flow regions of the hypersonic vehicle, therefore, it is undertaken herein for the explanation. Essentially for supersonic/hypersonic inviscid flow, placing a ramp obstruction generates the oblique shock wave from the ramp foot as depicted in Fig. 1.5(a). However, the presence of viscous effects in the boundary layer entangles the flow dynamics due to the interaction of shock wave and boundary layer adjacent to the wall. A general schematic of the ramp induced SWBLI is demonstrated in Fig. 1.5(b) which includes important flow features like reattachment shock, triple point

and separation shock. Thus, shock structure is completely different from the inviscid flow shock arrangement.

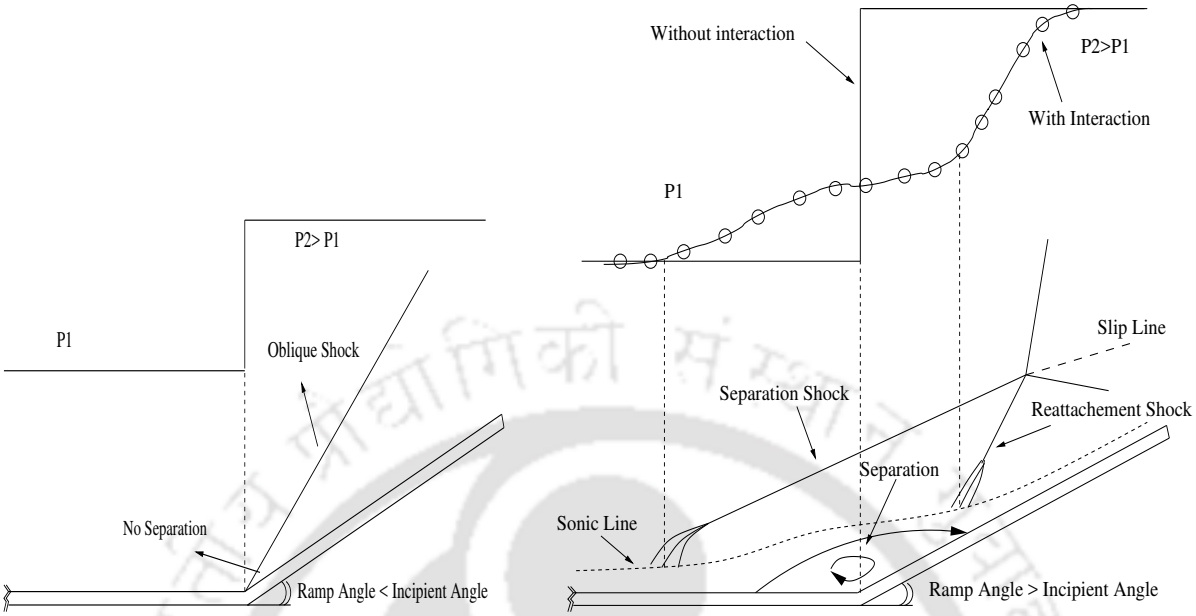

(a) Without SWBLI (b) With SWBLI

Figure 1.5: Schematic of ramp induced shock structure at different conditions

Here in fact, an introduction of adverse pressure gradient for fluid flow leads to dilatation of the boundary layer and subsequent formation of the thicker subsonic region. As a consequence, supersonic flow adjacent to wall turns into itself and results in a generation of compression waves which coalesce to form the separation shock. Downstream of the separation bubble, flow reattaches and introduces a reattachment shock. Further, both separation and reattachment shocks may interact and form a new shock. Apart from this, the subsonic region of boundary layer propagates the information of increased pressure at the ramp foot towards its upstream side. Due to this, pressure rises well ahead of the ramp foot and it is called as upstream influence phenomena. In the interaction zone, pressure rise happens in two phases. Initially, it is felt at separation shock and later at the reattachment point. In between these two points, a nearly constant pressure region is present and this pressure is called as plateau pressure. Further, all these features will occur only if the slope of a ramp is more than the incipient angle which is the minimum angle to introduce flow separation for a given supersonic/hypersonic freestream condition.

1.4 Literature review

Considering the importance of earlier discussed topics for high speed flows, this section deals with the literature survey of high temperature effects, wave drag reduction methods

and shock wave boundary layer interaction (SWBLI).

1.4.1 High temperature effects

As explained in the earlier section, high temperature effects have a prominent role on the aerodynamics of high speed vehicle. The most pioneered work to study the high temperature effects was done by Lobb [5]. He performed the series of experiments to calculate the shock stand-off distance on spheres propelled with hyper-velocity. Later, Rose and Stankevic [6] performed experiments in an arc-driven shock tube to estimate the stagnation point heat flux in a partially ionized stream. Hornung [7] experimentally presented the nitrogen dissociating flow over a blunt body. Subsequently, Kewley and Hornung [8] also experimentally studied the dissociation of nitrogen flow past a wedge. The shock curvature at the wedge leading edge was used to predict the dissociation rate.

Later on, various numerical investigations have been reported in this field to perform more detailed aerothermodynamic analysis [9, 10]. Grossman and Cinnella [11] performed the numerical computation of non-equilibrium chemistry and thermodynamics. They presented a flux splitting procedure for fully coupled inviscid equations and tested in 1-D computations including high temperature nozzle and shock tube flows. Further, Shuen et al. [1] also worked to derive several inviscid flux computation schemes like Steger-Warming, Van Leer and the Roe. The chemical non-equilibrium simulations were performed for 1-D shock tube and nozzle flows to assess these methods. Moreover, Tchuen et al. [12] extended the AUFS scheme to numerically simulate a 2-D hypersonic viscous flowfield of Mach number ranging between 6.4-25.9. The computational test cases included flow past compression corners and blunt bodies. Moss and Bird [13] simulated the hypersonic flow around the nose of the space shuttle using Direct Simulation Monte Carlo method (DSMC) with a chemistry model to account 5 species. The results were in fairly good agreement with the findings from experiment and viscous shock layer equations for low altitude freestream conditions. Moreover, no change in the composition of freestream gas behind the shock was observed at higher altitudes. Furthermore, Candler et al. [14] numerically simulated the radiative flowfield by undertaking two approaches; one was the continuum with rarefaction effects and the other one was DSMC. The comparison was made between two approaches for the same chemical kinetics and thermal relaxation models. Differences were observed in the concentration of nitric oxide captured by both approaches. Shuen [15] developed a robust upwind method to solve the chemical non-equilibrium Navier-Stokes equation. The numerical method was presented for the finite-volume based discretization of the Navier-Stokes equations. Encouraging numerical efficiency was shown for a hypersonic blunt body, SWBLI, divergent nozzle and ramped-duct flows.

Efforts have also been made to simulate and understand the chemical equilibrium flow. The calculation method of thermophysical properties of numerous species was documented by Gupta et al. [16] for temperature range up to 30000 K. Gordon and Mcbride [17] investigated the equilibrium compositions of the gas mixture for application of shock, rocket and detonation wave. In their work, the transport and thermodynamic properties of a variety of species were obtained by solving temperature dependent polynomial equation. Likewise, Yu et al. [18] presented a Helmholtz free energy minimization approach to figure out an equilibrium composition of chemically reacting flows. The proposed method was also tested in hypersonic internal flows for Mach number 10 and 13. Later on, Sawada et al. [19] validated their chemical equilibrium solver for hypersonic flowfield over a sphere with the available experimental data on shock stand-off distance. In this validation, an adaptive mesh was applied for better capturing of the shock wave. Recently, Pimentel and Annibal Hetem Jr. [20] developed an algorithm to obtain the chemical equilibrium composition of air based on the equilibrium constant method. They considered 5 as well as 7 species model to obtain the equilibrium composition for a wide range of temperatures and pressures. The presented algorithm was found easy to couple with any solver.

Many theoretical studies have been performed to pre-quantify the vital aerodynamic parameters. In 1972, Hurnung [7] shown that shock detachment distance and upstream flow patterns of dissociating nitrogen flow can be correlated in terms of reaction rate parameter. Later on, Wen and Hornung [21] improved the earlier correlation by accounting additional parameters of the non-dimensional freestream kinetic energy in order to extend its validity for complex multi-species reacting flows. In another study, Olivier [22] developed a theoretical model for frozen and equilibrium flows to predict the shock stand-off distance for flow past an axisymmetric blunt body. In addition, Belouaggadia at el. [23] also calculated the shock stand-off distance of blunt objects placed in hypersonic non-equilibrium flows. They also complimented the theoretical results with numerical data.

Different chemical models have been presented in the earlier studies [24–28]. Tchuen and Zeitoun [29] examined the influence of chemical kinetic models in a variety of cases including a wide range of Mach numbers. The attention was mainly towards the backward reaction rates in those studies. Further, Wang et al. [30] carried out similar numerical assessments by measuring surface heat flux on the hypersonic vehicles. Predictions were done for ELECTRE vehicle, Space Shuttle Orbiter and Apollo command module cases for Mach numbers between 13 to 20.5.

The non-equilibrium flow has also been examined in various aerodynamic applications. Hassan et al. [31] carried out a numerical study to investigate the real gas effects on blunt body aerodynamics. They incorporated 5 species reaction gas models in the

solver to simulate the flow over Apollo command module. It was found that the real gas effects may lower the trim angle and lift to drag ratio compared to non-reacting perfect gas flow. Later on, Mallinson et al. [32] performed experiments in the free piston driven shock tube to examine the high enthalpy and high Mach number effects on flat plate boundary layer flow. The effect of real gas was found to be small on density profile. The estimation of velocity boundary layer thickness was noted to be comparable with a theoretical prediction. Another study was reported by Mallinson et al. [33] for high enthalpy flow over a compression corner and flat plate. It was observed that the flow behaves as a frozen flow for all the conditions. The heat transfer and pressure data obtained from experiments were in good agreement with the theoretical estimation. Further, the expressions for high enthalpy separated region and upstream influence length were developed which also correlated with the earlier experiments. The pressure in the experiments was found to be matched well with the free interaction theory. Likewise, Grasso et al. [34] numerically analyzed the SWBLI in the presence of non-equilibrium phenomena. In addition, the influence of wall temperature and flap angle was studied on separation length, heat load and flap efficiency. The prominence of turbulence effects was noticed for flap angles more than a critical angle (15^o). Sagnier and Verant [35] performed high enthalpy wind tunnel experiments to investigate the influence of real gas effects. Moreover, the problem of validation was discussed through the analysis of typical experimental results obtained for ELECTRE sphere cone and Hyperboloid-flare induced separation. Further, Nonaka et al. [36] experimentally measured the shock shapes for various models like a cone, spheres and double cones in a ballistic range and compared with the theoretical results. The experiments were carried out in the air stream of velocity between 2.43-3.85 km/s where ambient pressure was kept between 600 and 10000 Pa. They also compared the shock shape of frozen, reacting and perfect gas flows. Apart from these, Knight et al. [37] developed the numerical model to study the microwave energy deposition based drag mitigation technique. In that study, 23 species and 238 reactions were taken into account to simulate flow past a cylinder. Significant dissociation of O_2 was observed whereas a rapid decay of NO was also noticed. Later on, Xiao-yuan et al. [38] simulated the flow through scramjet nozzle by solving the conservative Reynolds-averaged Navier-Stokes equations along with the RNG k-ϵ model. They demonstrated that, the expansion wave induced recombination reaction, inside the nozzle, is responsible to enhance its performance. Recently, Ajith et al. [39] developed a numerical methodology to simulate high temperature flows by considering chemical non-equilibrium and thermally equilibrium flows for two dimensional/axisymmetric models. In their work, fully catalytic nature of the wall was considered. They also demonstrated that dissociation of gas results in more surface heat flux. Further, Boyd [40] presented the numerical results for

ionization of hypersonic flowfield using direct simulation Monte Carlo. The simulations were performed for RAM-C II hypersonic flight conditions of velocity 8 km/s to precisely calculate the electron number density.

In recent years, interest has been shown to explore the aerodynamics in Martian environment [41, 42]. The numerical study for Mars atmospheric entry was reported by Candler [43]. For same, CO_2-N_2 chemistry model was incorporated into the 2-D computational fluid dynamic solver. He also emphasised the importance of thermal radiation as it could be useful for flow cooling. Mitcheltree and Gnoffo [44] computationally examined the Martian entry aerodynamics for a space vehicle. They considered non-ablating and ablating boundary conditions to analyze its effect on surface heating. Further, Sharma et al. [45] presented the experimental and numerical works to study the high enthalpy carbon dioxide flows. The experiments were performed in hyper-velocity expansion tube for aero-shell to do various measurements. The heat transfer and shock stand-off measurements agreed well with theoretical and numerical estimations for three different angles of attack. Recently, Hao et al. [46] numerically simulated the Mars flight conditions to compare the two different transport property models. It was found that, both the models provide similar translational-rotational and vibrational heat fluxes. Further collision integral model was noted to have better prediction capability to estimate the heat flux by chemical diffusion. Moreover, wake structure was found unaffected by the transport models.

1.4.2 Drag reduction methods

The aim of cost-efficient flight mandates drag mitigation which began around 1950s [47]. Many researchers introduced numerous methods to alleviate the wave drag by upstream flowfield alteration and subsequent formation of recirculation region ahead of the object. One of them is an energy deposition method which was proposed by Miller and Carlson [48]. They were the first to test its feasibility to change effective body shape of the aircraft using 1-D inviscid model. However, the adopted method was to reduce the shock noise. Myrabo and Raizer [49] performed the blast wave analysis to anticipate the restructured shock shape by energy spot along with power requirement and location of energy source for drag reduction. The study showed the decrement in power requirement at higher altitudes. This technique has also been used by Macheret et al. [50] to form a virtual cowl to turn the streamlines into scramjet inlet to control fluid spillage.

Later on, Riggins et al. [51] carried out a numerical examination for 2-D and axisymmetry blunt models at Mach number 6.5 and 10 conditions. The parametric investigation was carried out for various locations and strengths of power supply where up to 30% drag reduction was estimated. Additionally, they explained the role of fluid dynamics and ther-

modynamics behind the drag reduction technique. Subsequently, Levin et al. [52] studied the effect of energy source intensity on drag as well as surface heating of blunt sphere. The higher amount of drag reduction was obtained with the reduction in heat source size and increment in Reynolds number and Mach number. Further, they also pointed out considerable drag reduction with the small increment in the surface thermal load.

Zheltovodov et al. [53] carried out numerical analysis of steady and unsteady flow characteristics for blunt and sharp axisymmetric bodies at Mach number of 3.45 and two conditions. Furthermore, microwave energy interaction with shock layer was reported by Lashkov et al. [54]. The interaction led the vortex generation and its effect on the blunt models including a cylinder and hemisphere was explained. This study also suggested the use of microwave for effective flight control. Later on, Hartley et al. [55] numerically and experimentally studied the use of electric arc in air for drag mitigation in case of low enthalpy Mach number 10 flow. They noted 60–70% drag reduction in numerical as well as experimental investigations. Kremeyer et al. [56] examined experimentally the drag force of cone flying at supersonic/hypersonic streams. Experiments were performed over a range of Mach numbers from 2-8 and 15^o-45^o half angles of the cone. The interaction of low-density air and shock resulted in the 96% of drag reduction. Moreover, the ratio of energy saved to energy invested was recorded up to 65. Further, obtained results were also confirmed by presenting numerical results of higher order accurate finite difference based Euler solver. Satheesh and Jagadeesh [57] carried out experiments in short duration impulse test facilities for electric arc discharge ahead of a 60^o half angle blunt cone using air and argon test gases. They reported up to 50% unsteady drag reduction in the argon environment. Here, drag reduction was more in argon environment than the air at freestream Mach number of 7 in which electric arc was placed at a location 1.17 times body diameter, upstream of the stagnation point, along the stagnation streamline. Later on, Kulkarni et al. [58] reported the remarkable wave drag reduction up to 47% in Mach 8 stream by heat addition into the shock layer. Here, heat addition was obtained as a result of exothermic reactions activated by the ablation of coated chromium atoms from the stagnation region of a 60^o apex angle blunt cone. Further, Ogino et al. [59] documented the detailed physical explanation of an unsteady interaction of low-density core created by energy deposition with shock wave. The numerical study demonstrated the temporary low-entropy shock generated by Richtmyer–Meshkov like instability had led to low wave drag on a sphere. Apart from this, the reduced drag was found linearly dependent on the square of freestream Mach number and proportional to the low-density core radius. In the study, it was assumed that baroclinic vortex consumes the deposited energy and advects downstream without the shock layer thermalization.

Recently, many optimization studies have been reported for energy deposition tech-

niques. Markhotok [60] performed numerical study for the uniform, exponential and the power law plasma distributions in supersonic flow ahead of a blunt object. They also attempted to provide a better insight on the plasma based wave drag reduction technique by explaining various phenomena like shock deformation, reorganization of gas pressure, density upstream of the body, shock extinction in plasma region etc. The analytical expressions used in the models helped to separate wave drag influencing parameters to optimize the use of thermal energy input. Later on, Ganesh and John [61] carried out numerical optimization using high precision in-house inviscid flow solver. They identified the most optimum energy addition point among the multiple minimum drag points in their exhaustive study. Further, Gutiérrez and Poggie [62] performed the computational study for upstream volumetric energy deposition at freestream Mach number of 3 ahead of a slender body. This object was a combination of 15^o blunt cone and a cylindrical after-body. They also examined the thermal choking, optimization of important parameters and power requirements. Here, the thermal choking condition was referred where the power requirement reaches to twice the power saved by drag reduction.

Apart from energy deposition technique, the counter jet method has also been found to show encouraging drag decrement. The efforts to alter the oncoming flow using counter jet were earlier made by McMahon [63]. He introduced the secondary flow from the stagnation point of the blunt body against the mainstream. The study was performed to reduce the surface heat flux by injecting two different coolant gases including nitrogen and helium. Here, helium was found to be more effective than nitrogen for the same jet mass flow rate condition. Similarly, Warren [64] performed experiments to investigate the swirl and straight patterns of gas injection into the Mach number 5.8 flow. In this study, it was noticed that, high jet flow rate leads the coolant gasses to act like a spike and disturb the bow shock shape. This alteration resulted in a considerable surface pressure drop while no significant heat flux reduction was observed. Finley [65] documented the analytical and experimental studies for counter jet drag reduction. It was noted that the aerodynamic characteristics were mainly dependent on jet Mach number and flow force coefficient. Further, the sufficient condition required to attain a steady flow was also defined.

Later on, the short penetration modes (SPM) and long penetration (LPM) of issuing jet were examined in detail by Jarvinen and Adams [66]. They observed SPM had a stable shock structure with small shock detachment distance. Further, the distinct bow shock, Mach disk and free stagnation point were also the important characteristics. On contrary, larger shock stand-off distance with the diamond shock pattern consisting sufficient oscillation was spotted for LPM. Apart from these, transition appeared between LPM and SPM at critical pressure ratio which was found difficult to capture. Likewise, in

many other findings, the discussion was centred around different injection modes [67, 68].

Fox [69] presented the computational results on opposing jet for various conditions. However, no analysis was reported on an unstable flow regime. Later on, Fujita [70] numerically studied the sonic opposing jet, against the Mach number 2.5 freestream, from the nose of a hemisphere. In this study, a range of total pressure ratios, corresponding to stable and unstable flows, were considered. The aim was to obtain a more detailed interpretation of oscillation mechanism and transition from unstable to stable region computationally. Moreover, Debiéve et al. [71] noticed the strong dependence of flow characteristics on turbulence fluctuation. Further, Chen et al. [72] numerically investigated the issue of a supersonic jet from a blunt nose against the mainstream flow of Mach number 2.5. The study demonstrated enhancement of turbulence and it was attributed to the shear layer as well as shock interaction. They also used the feedback mechanism to explain the unsteady motion by disturbance propagation through various regions.

Venukumar et al. [73] reported the huge drag mitigation about 30%–45% for large angle blunt cone placed in the hypersonic stream. Moreover, the increment in jet total pressure to the pitot total pressure ratio was found to increase the drag reduction. Followed by this, Kulkarni and Reddy [74] investigated the effect of freestream total enthalpies. It was shown that the increment in total enthalpy by 2.5 resulted in the drag reduction by a factor 2 for the same jet to freestream total pressure ratio. The exploration by Yisheng [75] also numerically showed more drag reduction at higher total pressure ratio condition. In the study, they also introduced the new governing parameters R_{PA} for the opposing jet aerodynamics. Here, R_{PA} is defined as the product of jet total pressure to the pitot total pressure ratio and jet exit to body area ratio.

Attention was also directed towards the influence of jet nozzle configuration on drag reduction in many reports. Zhou and Ji [76] performed 3-D numerical computations for Mach 2.5 flow and considered various nozzle pressures, sizes and jet injection angles. They demonstrated the modifications in critical pressure ratio with the nozzle outlet size. Moreover, lower drag reduction was observed at the higher angle of attack. Li et al. [77] also considered various nozzle shapes including pentacle, cirque, square, circle and ellipse in their investigations. They achieved max drag reduction of around 23.6% for a pentacle-shaped nozzle. In a different study, the use of equal polygon opposing jet was also assessed by Li et al. [78]. Recently, Bibi et al. [79] carried out the parametric study to investigate the impact of divergent nozzle geometrical parameters like a divergent angle and nozzle length.

Some of the previous studies were aimed to use opposing jet as thermal protection for the blunt body. In these, Sahoo et al. [80] experimentally studied the effect of coolant

gas injection on heat transfer and drag over a blunt model at 5.75 Mach number. The study showed 30%–45% overall heat reduction with helium gas while in other cases it was between 10%–25%. Additionally, an increment in drag coefficient for helium injection was noted to be 12% whereas for other gases it was about 27%. Later on, Hayashi et al. [81] also studied the cooling effect of counter jets in unstable and stable flowfields. The effect of gaseous thermal protection increased with increment in total pressure ratio for a stable jet condition. However, no reduction in heat load was reported for unstable flowfield. Further, Meyer et al.[82] showed large heat and drag reduction in their numerical study.

The use of spike has also been widely discussed drag reduction method. One of the oldest experiment using it was performed by Stalder and Nielsen [83] on hemisphere-cylinder for Mach number ranging from 0.12 to 5.04. In supersonic flow, about 45% of drag reduction was obtained using spike body. Moreover, the heat transfer was doubled compared to the no-spike case in the study. Further, Maull [84] also performed the experimental investigations of flow past axisymmetric spiked bodies at hypersonic Mach number of 6.8. The unsteadiness was observed for some range of spike length and base body diameter in the study. Menezes et al. [85] experimentally demonstrated the effects of flat-disk spike attached to the nose of 120^o apex-angle blunt cone. This investigation reported about 55% drag reduction.

In recent advancements, numerous alternative techniques have been presented and combination of conventional methods has also been discussed. Shang [86] carried out the experimental and numerical investigation for opposing plasma injection for Mach number 6. Menezes et al. [87] studied the effect of the multi-step base of a missile-shaped body at hypersonic flows. The idea was successful to reduce the total drag up to 8%. They also numerically assessed the flow phenomena to obtain more detailed flow physics. Jiang et al. [88] analyzed the scheme of combining the drag reduction approaches of a physical spike and opposing jet. In this method, it was claimed that, a spike modifies the shock structure and the jet issued from spike protects it from overheating. This approach reduced 70% of reattachment pressure for 4^o angle of attack. Using similar technique, significant flowfield alteration along with the heat reduction was estimated by Gerdroodbary [89]. In the study, two gases including carbon dioxide and helium were used as a coolant. It was found that carbon dioxide removed more heat load compared to helium gas. Recently, Sun et al. [90] also studied the combinational approach where forward facing cavity and opposing jet on the nose were combined. Here, a multi-objective optimization study was done by employing the multi-island genetic algorithm coupled with Isight 5.5 where jet to freestream total pressure ratio and cavity diameter were optimized.

1.4.3 Shock wave boundary layer interaction

The SWBLI is a widely discussed topic among various research groups due to its apparent relevance to the flight performance. It can affect the efficiency of various components like scramjet intake [91], turbine [92], diffuser [93], compressor [94] etc. There are many theoretical [95, 96], experimental and numerical investigations which have been reported in this realm to develop a reliable understanding of SWBLI [97] and to take subsequent action to curb its detrimental effects. In particular, Ackeret et al. [98] laid the foundation for SWBLI research in the late 1940s. The objective of the study was to examine the effect of shock and boundary layer in a wind tunnel. They witnessed surprising shock patterns which were speculated as a consequence of frictional effects. These complicated shock geometries were also captured for the very first time in the history of laminar flow cases. Followed by this, Stewartson [99] presented a theoretical study of a weak shock wave boundary layer interaction where dependency of flow separation on Reynolds number was examined. Later on, Gadd et al. [100] performed a series of experiments to study the influence of various parameters like freestream Reynolds number, Mach number and shock strength on the shock impingement and ramp induced SWBLI. In this investigation, three different types of boundary layer were encountered. In the first one, boundary layer remained purely laminar. In the second type, turbulence was induced before reattachment and at last the turbulence became prominent before interaction region. The study indicated that the interaction mainly depends on local conditions rather than shock and its location. Further, Stewartson and Williams [101] developed a triple deck theory which explained the initial pressure rise and self-induced laminar boundary layer separation caused by moderate strong shock. They divided the region into three parts: boundary layer portion under inviscid forces, boundary layer region close to the wall and the supersonic freestream adjacent to the boundary layer.

Later on, the most appreciated free interaction theory was proposed by Chapman et al. [102] after conducting rigorous experimental and theoretical investigations. The theory provided a suitable insight into SWBLI. Hakkinen et al. [103] noticed that most of the earlier efforts were devoted toward the weak SWBLI. For this reason, they performed the studies for strong interactions between the shock and boundary layer. In the study, separation point was considered at zero value of surface skin friction coefficient. In a different investigation, Kuehn [104] reported hump like surface pressure distribution profile as an identification mark of separation region. Needham [105] also proposed a method to detect the interaction zone using the surface heat transfer criterion. Though it was very difficult to predict the very small dead air region using this method, he observed the smooth minimum of heat flux distribution near the interaction region.

For prior estimation of critical designing parameters, many correlations have also

been proposed. Needham and Stollery [106] empirically correlated the plateau pressure for well-separated flows at freestream Mach number between 2-16. In the document, they also demonstrated the extension of validity of free interaction theory for the hypersonic flow. Subsequently, Anders [107] correlated the plateau pressure for blunt and sharp leading edge configurations using free interaction parameters. Similar, efforts were made by Elfstorm [108] to predict the pressure at the wedge compression corner for turbulent flows. Hung and Barnett [109] analyzed the interface heating and developed a correlation based on available data for the wedge, flat plate and compression corner. The peak heating was correlated in terms of pressure ratio and Reynolds number. This expression was also found useful for full scale supersonic as well as the hypersonic space vehicles.

Along with theoretical and experimental works, significant contributions have also been made by performing numerical investigation by many researchers. The work documented by Carter [110] is considered to be one of the oldest computational studies. Carter [110] examined the supersonic laminar flow over a two-dimensional compression corner using finite difference method. Here, steady solutions were obtained by solving the unsteady Navier-Stokes equations. Similarly, MacCormack and Baldin [111] also solved the unsteady Navier-Stokes equation to examine shock-induced separation. Additionally, the turbulence effects were considered for high Reynolds number flows. Later on, Rizetta et al. [112] also presented numerical solutions for separated and non-separated high Reynold number flows and compared the results with the experimental data for a wide range of compression corner angles.

In the computational study by Hung and MacCormack [113] exponential stretching of mesh near boundary layer was provided to obtain better results. In the report, the leading edge shock was correlated with the peak surface pressure and heat load. Balleur et al. [114] used global and coupled approaches of finite difference method. In the first method, full Navier-Stokes equations were solved, while in other, two sets of equations were solved in their respective domain. The boundary conditions for inviscid flow were provided by the other set of equations considering viscous effects. Katzer [115] numerically analyzed the length and pressure scales of 2-D SWBLI for laminar flow past a flat plate with adiabatic wall condition. In this work, Mach number and Reynolds number ranged from 1.4-3.4 and 10^5 to 6×10^5 respectively were considered. This study also revealed the linear influence of shock strength on separation bubble length. It was found that triple deck theory over-predicts the length scale, so the increase in deviation was noticed at higher Mach number and Reynolds number. Further, new similarity law was also introduced to scale the separation bubble length.

Experimental results of SWBLI are considered to be the benchmark to validate different CFD solvers during 1990s. Rudy et al. [116] performed a numerical validation using

four different codes which include CFL3D, USA-PG2, LAURA, NASCRIN for 15^o and 24^o compression corner cases. It was mentioned that finite-span effects must be considered for stream-wise separation to achieve a precise estimation of separated flows. They demonstrated the quantitative and qualitative results using all four solvers for comparison with experimental data. Likewise, Fay and Sambamurthi [117] used Hanna code to validate for compression corner problem. They simulated for Mach number 14.1 flow and compared various parameters including skin friction coefficient, pressure distribution and heat transfer rates. Results from the numerical solution matched well with 15^o compression corner experimental results. Later on, Reynolds-averaged Navier-Stokes solver was validated for transitional and laminar SWBLI by Grasso et al. [118]. They also highlighted the importance of the grid aspect ratio in capturing important flow features like peak heating, separation extent etc.

Later on, Grasso and Marini [119] numerically studied the hypersonic viscous flows for different test cases including wing-fuselage and wing-flap junction configurations. In those studies, different effects like leading edge shape, viscous interaction parameter and deflection angle on the flowfield were investigated. Additional scaling laws for peak heating, upstream influence and various aerodynamic coefficients were established using theoretical and numerical work. Marini [120] did a valuable contribution by providing a detailed physical interpretation of SWBLI for 2-D ramp and 2-D axisymmetric hollow cylindrical flare models. He studied the influence of wall temperature, ramp angle, finite span and axisymmetry. The results were validated using theoretical analysis, experimental data and correlation laws. Owing to the great importance of real gas effects, Davis and Sturtevant [121] carried out experimental and numerical analysis to examine these effects on recirculation length induced by double-wedge model. They also proposed scaling parameters to account wall temperature effect on separation length for laminar non-reacting boundary layer and arbitrary viscosity law. Further, Deepak et al. [122] also considered the real gas effects in their numerical study. The work was done for high enthalpy flow (19 MJ/kg) past a 24^o ramp. Significant discrepancies were demonstrated in reattachment and recirculation regions compared to perfect gas simulations. John et al. [123] performed investigations using in-house developed 2-D finite volume solver. Their study included the effect of variation of wall and freestream properties along with the geometrical alterations. The study suggested that, wall temperature to freestream stagnation temperature was a decisive parameter. In the same year, John and Kulkarni [124] carried out a numerical study for R-SWBLI in order to explore the various earlier reported correlations. They discussed the best correlations among them for precise estimation of characteristics flow features like separation bubble length, upstream influence, separation point, plateau pressure, peak heat flux. Moreover, attempts were also made

to modify the existing correlations to improve the prediction capability.

Numerous investigations were carried out to diminish SWBLI since it was found undesirable. Many control techniques are available in the literature which include the use of blunt leading edge, injection or suction of mass, vortex generator [125, 126], energy deposition [127, 128], pressure feedback channel etc. The report by Townsend [129] was considered to be the earliest endeavours for SWBLI control. He examined the effect of leading-edge bluntness for flow past a compression ramp. In this study, decrement in separation bubble size and plateau pressure was observed with the increment in bluntness. Moreover, it was concluded that the alteration in upstream local Mach number and Reynolds number had a significant impact on SWBLI. Holden [130] performed the series of experiments for low Reynolds number and high Mach number flow past a wedge. These experiments were performed for sharp and blunt leading edge configurations. An increment in bluntness resulted in wider separation for well-separated flow and on contrary, the decrement in separation for either case was noticed. This study also provided the correlations to predict the plateau pressure and minimum angle required to cause the separation. Gray and Rhudy [131] also conducted tests at different Mach number, Reynolds number and wall to freestream total temperature ratios. They investigated the effect of bluntness and wall cooling on separation of supersonic laminar flow. Here, the upstream extent was greater for intermediate blunt radius than other cases. However, the upstream interaction was more than the sharp leading edge cases. Further, reduction in the interaction extent to a significant degree was noted with a decrement in wall temperature. In another experimental study, Coet and Chanetz [132] had also made the same observations. In the experiment, separation bubble size decrement was noticed with increase in bluntness. The experiment was performed for Mach number 10 flow past a 15^o ramp. The surface heat flux and pressure distribution were measured to calculate separation size. Moreover, Neuenhahn and Olivier [133] analyzed the effect of entropy layer formed by blunt leading edge configuration on compression corner. They concluded that the entropy layer mainly affects the separation bubble size. Since every research group had a different opinion related to the provision of leading-edge bluntness, John and Kulkarni [4] attempted to identify the reasons for same in their numerical study. It was found in the investigation that the separation region widens with an increase in bluntness whereas it starts to reduce after attaining the maximum. Further, the existence of inversion and equivalent radius were noticed. They also provided prediction methodology for two critical blunt radii by explaining entropy layer-boundary layer interaction and blast wave theory. Further, John et al. [134] marked the non-existence of equivalence radius for 2-D axisymmetric configuration. Moreover, John and Kulkarni [135] also documented the influence of wall temperature, freestream Mach number and enthalpy on

values of critical radii.

Apart from these, Lewis et al. [136] analyzed the cooling effect on compression corner induced separation in their experiment in a wind tunnel. The dependence of surface pressure distribution on Reynolds number was observed. This experimental study also confirmed the free interaction concept suggested by Chapman et al. [102] for an adiabatic wall. Another promising approach was dead mass removal and upstream mass injection. Inger and Zee [137] analyzed the effect of mass transfer by suction and blowing. The study showed a significant amount of separation reduction by both the methods. Likewise, Ball [138] studied the effect of the suction slot over a Mach number range of 5.3 to 8 for 2-D laminar separated flow. In this study, the separated region was found sensitive to suction slot as the small percentage of recirculation mass removal led to sufficient reduction in separation length. Recently, Pasquariello et al. [139] used the control technique which uniquely connected the suction underneath separation region and injection at upstream of interaction through a duct. The numerical study was performed for Mach number 3 where an impinging oblique shock on a flat plate was generated by an 8.8^o wedge. The suction position was varied while keeping the blowing location constant. The separation bubble size reduction was more when the suction location was kept in the rear part of it. This method also diminished the turbulence production within the interaction region. A similar approach was earlier implemented by Faulker [140] in wings to reduce the wave drag.

1.5 Objectives of the present study

One of the major objectives of present studies is to simulate the high temperature reacting flows. It is evident from the literature that computations for reacting flows is one of the tough tasks. Hence, it is found essential to develop a higher order accurate reacting viscous compressible flow solver. The proposed solver must be proficient to simulate the low as well as high enthalpy flowfields so as to have wide applicability. Additionally, its capability can be enhanced by incorporating various flux evaluation schemes. Further, validation of solver with the various numerical and experimental results of different benchmark problems is also imperative to authenticate its potential before conducting the numerical study. In particular, vital parameters like skin friction coefficient, mass fraction of various species, boundary layer thickness, entropy layer thickness etc. are either impossible or very difficult and costly to obtain by performing experiments. These problems can be tackled by employing in-house developed solver for investigation and to obtain more detailed flowfield information.

In the literature survey of high enthalpy hypersonic flows, most of the researchers or

research groups have either implemented only one flux computations scheme or schemes of the same family [1, 12]. Thus, efforts are required to extend the well-accepted convective flux calculation schemes and assess their performance in the complex flow situations involving real gas effects. It is also highly desirable to assess the role of conventional non-dimensional numbers like Mach number in deciding the flow characteristic of high enthalpy flows. Further, it has been noted that numerous investigations are reported for energy deposition based drag reduction technique. Most of them are centred on low enthalpy flowfields [51, 52]. However, it is expected that in case of high enthalpy flows the mechanism of flowfield alteration would be strongly influenced by the strong real gas effects even for the small amount of upstream energy deposition. Apart from this aerothermodynamic analysis of this technique by accounting the high temperature effects would help in quantifying the effectiveness more precisely. Therefore, it is extremely important to assess and highlight the role of real gas effects on flowfield modifications at various freestream stagnation enthalpies and strength of deposited energy.

Counter jet drag reduction technique has also been discussed in the literature. It had been observed by the researchers that the effectiveness of the fluidic-spike increases with increase in stagnation enthalpy of the hypersonic flow [74]. Similarly, the influence of various other parameters on opposing jet performance has been discussed which include mass flow rate [64], jet to freestream total pressure ratio [73], jet to body area ratio, jet exit Mach number [65], R_{PA} [75] etc. However, no fluid dynamical insight is given for those studies for the alteration in drag force. Hence, it is essential to carry out detailed computational studies to figure out the universal governing parameter for this active drag reduction technique and to reveal the scientific mystery.

Moreover, in the field of SWBLI, many control strategies have been proposed which include energy deposition, blunt leading edge, vortex generator, mass injection/suction, pressure feedback technique etc. Among these, limited attention is paid towards the use of pressure feedback technique (PFT). It is a combination of upstream mass injection and removal of dead air mass from the interaction region. This interconnected arrangement has proved to have the encouraging scope of controlling the adverse effects of shock impingement based interaction [139]. Therefore, it is required to verify the reliability of PFT in R-SWBLI induced separation. In addition, the influence of vital parameters like ramp angle and wall to freestream total temperature ratio on PFT performance is also needed to be examined. Another widely discussed control technique is the provision of a blunt leading edge. Many researchers have the clashing observations regarding the use of blunt leading edge technique [131–133]. Later, John and Kulkarni [4] revealed the physics through numerical investigations and noted that the separation extent initially increases with the increment in bluntness and attains maximum value at the inversion radius.

Beyond this point, a further increment in bluntness lowers the recirculation region size although it remains larger than the reference sharp leading edge case until an equivalent radius value is reached. Thus, blunt leading edge assures the separation reduction only if it is more than the equivalent radius. This fact clearly illustrates the limitation of this method for separation mitigation. On the other hand, earlier mentioned pressure feedback method also has its own constraint on the alleviation of dead air region. In the literature survey, efforts to improve the performance of both these flow separation control techniques are not evident. Therefore, it would be interesting to combine the PFT and leading-edge bluntness in an attempt to enhance their controllability. This would also be beneficial in lowering the equivalent radius value of a blunt leading edge technique. Further, it is also noted in the literature that the SWBLI has been assessed by very few researchers in the presence of real gas effects [33, 34]. Thus, the literature, in this field, largely lags in computations for high enthalpy conditions. In this case, consideration of high temperature effects would help in precise estimation of all the parameters of SWBLI. Along with this, it is essential to review the blunt leading edge based separation control technique in the presence of high temperature effects. Additionally, it is extremely important to couple the reacting gas flow solver with optimization procedures for accurate estimation of critical radii (inversion and equivalent radius).

In light of these discussions, the development of a Navier-Stokes (NS) solver for supersonic/hypersonic flow studies and its implementation for various applications in this flow regime are listed in the form of objectives:-

1. Development of an unstructured finite volume Navier-Stokes reacting gas flow solver embodying various flux computation schemes of different families.
2. Validation of in-house developed solver with various standard or literature reported results including 2-D and axisymmetric cases.
3. Assessment of various incorporated convective flux calculation schemes in the presence of strong chemical reacting flows.
4. Aerothermodynamic analysis of the energy addition based drag reduction technique for perfect, frozen and reacting gas flows at various energy strength and freestream total enthalpies.
5. Assessment of various influencing parameters of opposing jet flow based drag reduction method at different stable flowfield conditions.
6. Study of pressure feedback technique for R-SWBLI provoked flow separation control.
7. Evaluation of the effect of ramp angle and wall to freestream total temperature ratio on the performance of PFT. Further, investigation of the combined effect of leading edge bluntness and PFT for R-SWBLI.

8. Examination of the performance of blunt leading edge flow separation control technique in the presence of real gas effects and to figure out the critical radii precisely through optimization studies.

Organization of thesis

1. Chapter 2 is devoted to the numerical formulation of the in-house developed reacting gas flow solver.
2. Chapter 3 deals with the investigation of real gas effects at unsteady (shock tube) and steady (cylinder and sphere) high enthalpy cases.
3. Chapter 4 discusses the effect of different gas models on the performance of energy deposition based drag reduction techniques.
4. In Chapter 5, the examination of various influencing parameters of counter jet drag reduction is discussed in order to understand the aerodynamics of this technique.
5. Chapter 6 demonstrates the effectiveness of the pressure feedback technique for separation mitigation provoked by ramp based shock wave boundary layer interaction.
6. Chapter 7 focuses on the passive control of SWBLI induced separation using the leading edge bluntness alone for perfect and reacting gas flow models.
7. The thesis ends with conclusions and future scopes in Chapter 8.

CHAPTER 2

NUMERICAL METHODOLOGY

Overview

This chapter discusses the numerical strategies considered to simulate the low and high enthalpy compressible flows. Cell-centred finite volume based solution procedures for governing equations are explained herein. The technique to compute viscous and inviscid fluxes and the implementation process of different boundary conditions are also part of this chapter. Further, details of temporal discretization method along with source term treatment procedure are also provided. Apart from these, various gas models considered for numerical investigations are presented in the chapter.

2.1 Governing equations

Computational fluid dynamic (CFD) is a methodology to solve the governing mathematical models for fluid flow using suitable numerical technique. It is an efficient approach to simulate the variety of fluid problems in an economical way as compared to costly experimental procedures. Therefore, it has been integral part of designing supersonic/hypersonic aircraft like reentry vehicles, missiles etc. Simulation for these compressible flows involves the solution of Navier-Stokes equations for low enthalpy conditions. However, consideration of reacting gas flow is important for precise prediction of high enthalpy flowfield. Therefore, species continuity equations also need to be solved along with the Navier-Stokes equations. The source term of these added equations accounts for the species production rate which is insignificant in the low enthalpy non-reacting gas flow. The coupled Navier-Stokes and species continuity equations for 2-D axisymmetry laminar viscous compressible flows in vector form are presented as follows:-

$$\frac{\partial U}{\partial t} + \frac{\partial E_I}{\partial x} + \frac{\partial F_I}{\partial y} + S + \alpha(S_I - S_v) = \frac{\partial E_v}{\partial x} + \frac{\partial F_v}{\partial y} \tag{2.1}$$

Where,

$$U = \begin{pmatrix} \rho \\ \rho u \\ \rho v \\ \rho E \\ C_1 \\ . \\ . \\ C_{N-1} \end{pmatrix}, E_I = \begin{pmatrix} \rho u \\ \rho u^2 + p \\ \rho uv \\ (\rho E + p)u \\ uC_1 \\ . \\ . \\ uC_{N-1} \end{pmatrix}, F_I = \begin{pmatrix} \rho v \\ \rho uv \\ \rho v^2 + p \\ (\rho E + p)v \\ vC_1 \\ . \\ . \\ vC_{N-1} \end{pmatrix}, E_v = \begin{pmatrix} 0 \\ \tau_{xx} \\ \tau_{xy} \\ u\tau_{xx} + v\tau_{xy} - q_x - \sum_{i=1}^{N} h_i C_i \overline{u}_{\ i} \\ -C_1 \overline{u}_{\ 1} \\ . \\ . \\ -C_{N-1} \overline{u}_{\ N-1} \end{pmatrix},$$

$$\mathrm{F}_v = \begin{pmatrix} 0 \\ \tau_{xy} \\ \tau_{yy} \\ u\tau_{xy} + v\tau_{yy} - q_y - \sum_{i=1}^{N} h_i C_i \overline{v}_{\ i} \\ -C_1 \overline{v}_{\ 1} \\ . \\ . \\ -C_{N-1} \overline{v}_{\ N-1} \end{pmatrix}, \; S = - \begin{pmatrix} 0 \\ 0 \\ 0 \\ 0 \\ S_1 \\ . \\ . \\ S_{N-1} \end{pmatrix}, S_I = \frac{1}{y} \begin{pmatrix} \rho v \\ \rho uv \\ \rho v^2 \\ (\rho E + p)v \\ vC_1 \\ . \\ . \\ vC_{N-1} \end{pmatrix},$$

$$\mathrm{S}_v = \frac{1}{y} \begin{pmatrix} 0 \\ \tau_{xy} - \frac{2}{3} y \frac{\partial(\mu v/y)}{\partial x} \\ \tau_{yy} - \tau_{\theta\theta} - \frac{2}{3}\mu(\frac{v}{y}) - \frac{2}{3} y \frac{\partial(\mu v/y)}{\partial y} \\ u\tau_{xy} + v\tau_{yy} - q_y - \frac{2}{3}\frac{\mu v^2}{y} - \frac{2}{3} y \frac{\partial(\mu v^2/y)}{\partial y} - \frac{2}{3} y \frac{\partial(\mu uv/y)}{\partial x} - \sum_{i=1}^{N} h_i C_i \overline{v}_{\ i} \\ -C_1 \overline{v}_{\ 1} \\ . \\ . \\ -C_{N-1} \overline{v}_{\ N-1} \end{pmatrix}$$

where, U is the conserved variable vector, E_I and F_I are convective flux vectors in x and y directions and S is source term vector. The inviscid and viscous axisymmetric source terms are represented as S_I and S_v respectively, α is a constant ($\alpha = 1$ for 2-D axisymmetric, $\alpha = 0$ for 2-D problem) while E_v and F_v are viscous flux vectors in x and y directions. Further, the physical variables are density (ρ), velocity (u) in x direction, velocity (v) in y direction, pressure (p), temperature (T), internal energy $\left(e = \sum_{i=1}^{N} e_i \frac{C_i}{\rho M W_i}\right)$ and total energy $\left(E = e + \frac{1}{2}(u^2 + v^2)\right)$. The total number of species is N

and $e_i = h^0_{fi} + \int_{T_R}^{T} C_{pi} dT - R_u T$ is the molar internal energy of i^{th} species for which C_i , MW_i , h^0_{fi} , and C_{pi} are the mass concentration, molecular weight, heat of formation, and specific heat at constant pressure, respectively. Here, R_u is the universal gas constant and T_R is the reference temperature. The shear stress components are $\tau_{xx} = \mu(\frac{4}{3}\frac{\partial u}{\partial x} - \frac{2}{3}\frac{\partial v}{\partial y})$, $\tau_{xy} = \mu(\frac{\partial u}{\partial y} + \frac{\partial v}{\partial x})$, $\tau_{yy} = \mu(\frac{4}{3}\frac{\partial v}{\partial y} - \frac{2}{3}\frac{\partial u}{\partial x})$ and $\tau_{\theta\theta} = \mu\Big[\frac{-2}{3}(\frac{\partial u}{\partial x} + \frac{\partial v}{\partial y}) + \frac{4}{3}\frac{v}{y}\Big]$. Further, $\overline{u}$ and $\overline{v}$ are the diffusion velocities in x and y directions which can be calculated as using Fick's law: $Y_i\overline{u} = -D_{im}\frac{\partial Y_i}{\partial x}$, $Y_i\overline{v} = -D_{im}\frac{\partial Y_i}{\partial y}$, where D_{im} is constant and its value is taken constant [2] (5×10^{-5} m^2/s).

Present form of the solver is equipped with the polynomial fits for specific heat, viscosity and thermal conductivity as described by Gordon and McBride [17]. The closure to the system is provided by using the equation of state in which the mixture pressure is assumed to be the sum of partial pressures of individual species.

$$p = R_u T \sum_{i=1}^{N} \frac{C_i}{MW_i} \tag{2.2}$$

Temperature in the above equation is obtained from internal energy iteratively by using Newton-Raphson method.

$$\rho e = \sum_{i=1}^{N} \frac{C_i}{MW_i} \left(\int_{T_R}^{T} C_{pi} dT + h^0_{fi} \right) - p \tag{2.3}$$

Details of the chemical kinetics are given in the following section.

2.2 Chemical kinetics

A set of N_R elementary reversible reactions involving N species may in general be represented as:-

$$\sum_{j=1}^{N} \nu'_{ij} n_j \rightleftharpoons \sum_{j=1}^{N} \nu''_{ij} n_j \tag{2.4}$$

where i = 1,2,...,N$_\text{R}$, ν'_{ij} and ν''_{ij} are the stoichiometric coefficients for species j appearing as a reactant in the i^{th} forward and backward reactions respectively and $n_j = \frac{C_j}{MW_j}$ is the molar concentration for species j. The Arrhenius rate expression is used for rate constant of a reaction i which is given as,

$$k_i = A_i T^{m_i} e^{\frac{-E_i}{R_u T}} \tag{2.5}$$

Here, E_i represents the activation energy and A_i and m_i are constants. A five species (N_2, O_2, N, O, NO) model involving eleven elementary reactions is employed in all the cases presented in subsequent chapters. The rate of change of molar concentration of species j is then given by summing up the changes due to all reaction steps,

$$S_j = MW_j \sum_{i=1}^{N_R} (\nu_{ij}^{''} - \nu_{ij}^{'}) \left(k_{fi} \prod_{l=1}^{N} n_l^{\nu_{il}^{'}} - k_{bi} \prod_{l=1}^{N} n_l^{\nu_{il}^{''}} \right) \tag{2.6}$$

where k_{fi} and k_{bi} are the forward and backward rate constants for reaction i. The reactions and the corresponding rate constants are given in Table 2.1.

Table 2.1: Chemical reactions and specific reaction-rate constants for chemical reaction calculations (Shuen et al. [1])

No.	Forward reaction	k_{fi} (cm^3/mole sec)	k_{bi} (cm^3/mole sec) or (cm^6/$mole^2$ sec)
1	$O_2 + M -> 2O + M(N)$	$3.6 \times 10^{18} T^{-1.0} e^{-5.95\times10^4/T}$	$3.0 \times 10^{15} T^{-0.5}$
2	$N_2 + M -> 2N + M(O)$	$1.9 \times 10^{17} T^{-0.5} e^{-1.13\times10^5/T}$	$1.1 \times 10^{16} T^{-0.5}$
3	$NO + M -> N + O + M(O_2)$	$3.9 \times 10^{20} T^{-1.5} e^{-7.55\times10^4/T}$	$1 \times 10^{20} T^{-1.5}$
4	$O + NO -> N + O_2$	$3.2 \times 10^{9} T^{1} e^{-1.97\times10^4/T}$	$1.3\times10^{10} T^{1.0} e^{-3.58\times10^3/T}$
5	$O + N_2 -> N + NO$	$7.0 \times 10^{13} e^{-3.8\times10^4/T}$	1.56×10^{3}
6	$N + N_2 -> N + N + N$	$4.085\times10^{22} T^{-1.5} e^{-1.13\times10^5/T}$	$2.27 \times 10^{21} T^{-1.5}$
7	$O_2 + O -> 2O + O$	$9.0 \times 10^{19} T^{-1.0} e^{-5.95\times10^4/T}$	$7.5 \times 10^{16} T^{-0.5}$
8	$O_2 + O_2 -> 2O + O_2$	$3.24 \times 10^{19} T^{-1.0} e^{-5.95\times10^4/T}$	$2.7 \times 10^{16} T^{-0.5}$
9	$O_2 + N_2 -> 2O + N_2$	$7.2 \times 10^{18} T^{-1.0} e^{-5.95\times10^4/T}$	$6 \times 10^{15} T^{-0.5}$
10	$N_2 + N_2 -> 2N + N_2$	$4.7 \times 10^{18} T^{-0.5} e^{-1.13\times10^5/T}$	$2.72 \times 10^{16} T^{-0.5}$
11	$NO + M -> N + O + M(O)$	$7.8 \times 10^{22} T^{-1.5} e^{-7.55\times10^4/T}$	$2.0 \times 10^{20} T^{-1.5}$

2.3 Finite volume method (FVM)

Finite volume method (FVM) is widely used discretization method for the variety of fluid flow simulations. In this method, space is divided into a number of arbitrary control volumes in which integral form of governing equations are solved. This method is based on conservation laws as well as it does not require any coordinate transformation, unlike finite difference method. It is also suitable for the complex geometrical problems as it works perfectly on both structured and unstructured grids. Moreover, the

non-overlapping criteria of control volumes allow FVM to perform straightforward integration of equations. There are two different approaches to implement FVM, which are categorized on control volume arrangements; first is cell-centred approach and other is a cell-vertex approach. Present thesis work is based on the cell-centred scheme due to simplicity in its implementation. In this approach, flow variables are stored at cell centroids as shown in Fig 2.1. The present solver can handle both structured and unstructured grids for numerical simulation as it is written in an unstructured format.

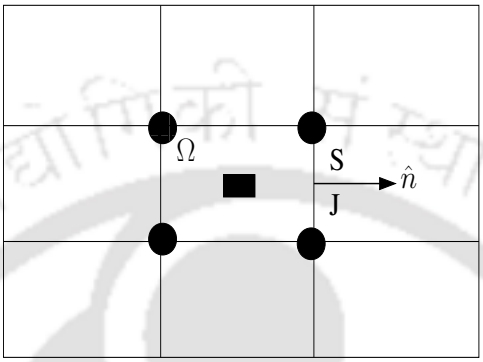

Figure 2.1: Representation of cell centered FVM scheme

2.4 Theoretical formulation of cell centered FVM

The integration of Eqn 2.1 over control volume (Ω) can be done as:-

$$\int_{\Omega}\left(\frac{\partial U}{\partial t}+\frac{\partial E_I}{\partial x}+\frac{\partial F_I}{\partial y}-\frac{\partial E_v}{\partial x}-\frac{\partial F_v}{\partial y}+S+\alpha(S_I-S_v)\right)\mathrm{d}\Omega=0 \tag{2.7}$$

This equation can be rewritten as:-

$$\int_{\Omega}\frac{\partial U}{\partial t}\mathrm{d}\Omega=-\int_{\Omega}\left(\frac{\partial E_I}{\partial x}+\frac{\partial F_I}{\partial y}-\frac{\partial E_v}{\partial x}-\frac{\partial F_v}{\partial y}+S+\alpha(S_I-S_V)\right)\mathrm{d}\Omega \tag{2.8}$$

Considering only left hand side of Eqn 2.8:-

$$\begin{aligned}\int_{\Omega}\frac{\partial U}{\partial t}d\Omega&=\frac{\partial}{\partial t}\int_{\Omega}U d\Omega\\&=\frac{d}{dt}(\bar{U}\Omega)\\&=\Omega\frac{d}{dt}\bar{U}\end{aligned} \tag{2.9}$$

Here, $\bar{U}=\frac{\int_{\Omega}U d\Omega}{\int_{\Omega}d\Omega}$.

Now, taking right hand side of Eqn 2.8:-

$$\int_{\Omega}\Big(\frac{\partial E_I}{\partial x}+\frac{\partial F_I}{\partial y}-\frac{\partial E_v}{\partial x}-\frac{\partial F_v}{\partial y}+S+\alpha(S_I-S_v)\Big)d\Omega=0 \tag{2.10}$$

This equation can be rewritten as:-

$$\int_{\Omega}\Big(\nabla.(H_I-H_v)+S+\alpha(S_I-S_v)\Big)d\Omega=0$$

Here, H_I= $[E_I\ F_I]$, H_v = $[E_v\ F_v]$ and ∇= $[\frac{\partial}{\partial x}\ \frac{\partial}{\partial y}]$.

Now, considering $H = (H_I - H_v)$ and applying Gauss divergence theorem to first term of Eqn 2.10:-

$$\int_{\Omega}\nabla.H d\Omega=\int_{S}H.\hat{n}dS$$

$$\int_{S}H.\hat{n}\,\mathrm{d}S=\sum_{J=1}^{n_f}H_J.\hat{n}_J\,\Delta S_J=\sum_{J=1}^{n_f}H_{\perp J}\,\Delta S_J \tag{2.11}$$

where, $\hat{n}$ unit control surface normal pointing outward of the control volume, n_x and n_y are the x and y components of the unit vector $\hat{n}$. For 2-D case ΔS_J is the length of the face of a control volume. Here, $H_\perp$ is the summation of inviscid (H_I) and viscous normal (H_v) fluxes crossing the faces of a control volume. Hence, it can be written as:-

$$H_\perp = H_{I_\perp} - H_{V_\perp} \tag{2.12}$$

where,

$$\mathrm{H_{I_\perp}}=\begin{bmatrix}\rho u_\perp\\ \rho u u_\perp+pn_x\\ \rho v u_\perp+pn_y\\ (\rho e+p)u_\perp\\ C_1u_\perp\\ .\\ .\\ C_{N-1}u_\perp\end{bmatrix},\ \mathrm{H_{V_\perp}}=\begin{bmatrix}0\\ n_x\tau_{xx}+n_y\tau_{xy}\\ n_x\tau_{yx}+n_y\tau_{yy}\\ n_x\Theta_x+n_y\Theta_y\\ 0\\ .\\ .\\ 0\end{bmatrix}$$

The contravariant velocity $u_\perp$ can be shown as:-

$$u_\perp = u.n_x + v.n_y \tag{2.13}$$

In energy equation, work done by viscous force and heat transfer are written as:-

$$\begin{aligned}\Theta_x &= u\tau_{xx} + v\tau_{xy} - q_x - \sum_{i=1}^{N} h_i C_i \overline{u}_{\ i} \\ \Theta_y &= u\tau_{yx} + v\tau_{yy} - q_y - \sum_{i=1}^{N} h_i C_i \overline{v}_{\ i}\end{aligned} \tag{2.14}$$

Similarly, source terms in Eqn (2.9) can be treated as:-

$$\int_{\Omega} \Big(S + \alpha(S_I - S_v) \Big) d\Omega = \Omega \overline{S}_c + \alpha \Omega \overline{S} \tag{2.15}$$

where,

$$\overline{S} = \overline{S}_I - \overline{S}_v \tag{2.16}$$

Therefore from Eqn (2.9), (2.11) and (2.15) the final integral form of the governing equation (2.8) is:-

$$\begin{aligned}\Omega_{\mathrm{i}} \frac{\mathrm{d}\overline{\mathrm{U}}_{\mathrm{i}}}{\mathrm{dt}} + \sum_{\mathrm{J}=1}^{\mathrm{n_f}} \mathrm{H}_{\perp \mathrm{J}}\, \Delta \mathrm{S}_{\mathrm{J}} + \Omega_{\mathrm{i}} \overline{\mathrm{S}}_{\mathrm{ci}} + \alpha \Omega_{\mathrm{i}} \overline{\mathrm{S}}_{\mathrm{i}} = 0 \\ \frac{\mathrm{d}\overline{\mathrm{U}}_{\mathrm{i}}}{\mathrm{dt}} = -\frac{1}{\Omega_{\mathrm{i}}} \sum_{\mathrm{J}=1}^{\mathrm{n_f}} \mathrm{H}_{\perp_{\mathrm{J}}}\, \Delta \mathrm{S}_{\mathrm{J}} - \overline{\mathrm{S}}_{\mathrm{ci}} - \alpha \overline{\mathrm{S}}_{\mathrm{i}} = \mathrm{R}(\overline{\mathrm{U}}_{\mathrm{i}})\end{aligned} \tag{2.17}$$

2.5 Spatial discretization

The solution of semi-discretized governing equation mentioned in Eqn 2.17 requires evaluation of the residual $R(\overline{U}_i)$. This can be done by calculating the convective and viscous fluxes at faces of the control volume. Hence, the accuracy of the solution is dependent on flux calculation methodologies. The various flux evaluation schemes incorporated in present solver are mentioned in the following subsections.

2.5.1 Flux computation schemes

In the present finite volume cell centered formulation, convective fluxes are computed using various schemes and the formulation of each scheme used in present work is given in the Appendix. The schemes chosen here are Van Leer [141], AUSM [142], AUSM+ [143] and Rusanov [144]. It may be noted that the concentrations of different species change due to chemical reactions resulting in limitations in estimating the equation of state a priory. The flux vector loses its homogeneity and certain changes must be incorporated in the formulations of some schemes while applying them to reacting gas flows. These modified flux formulations are adapted from various sources as mentioned in Table A.

2.5.2 Solution reconstruction for spatial accuracy

Upwind schemes demand flow variables to be assigned on left and right side of the face of a control volume. In case of first order spatial accuracy, these variables can be computed by simply providing left and right side flow quantities of the face. However, first order solution may lead to unreasonable shear layer growth and thicker shock. Therefore, higher order spatial discretization is required for present study. Herein, second-order accuracy is achieved by embodying Barth and Jespersen [145] piece-wise linear reconstruction method. This method assumes piece-wise linearly distributed solution over the control volume. Thus left and right state variables are calculated as follows:

$$U_{left} = U_{I_{cell}} + \psi(\nabla U_{I_{cell}}.\vec{r}_{left})$$
$$U_{right} = U_{J_{cell}} + \psi(\nabla U_{J_{cell}}.\vec{r}_{right})$$

Here, $\nabla U_{I_{cell}}$ is the gradient of U at the cell center I, which is calculated as:-

$$U_{I_{cell}} = \left[\frac{\partial U}{\partial x}, \frac{\partial U}{\partial y}\right]^T$$

In the expression, $\vec{r}_{left}$ and $\vec{r}_{right}$ represent the vectors pointing from the cell-centroid towards the face centroid as shown in the Fig 2.2. Further, ψ is a limiter function which is used to ensure the monotone second-order solution near discontinuity. The second order solution often shows oscillation in high gradient regions like shock. This monotonicity loss can be limited using limiter functions. It produces non-increasing maxima and non-decreasing minima and restricts to generate new local extrema. Limiter function ascertains that, reconstructed left and right flow variables do not exceed the maximum and minimum of the corresponding cell centroid value. In the present solver, Venkatakrishnan's limiter is incorporated as it assures better convergence along with the oscillation free solution. According to this methodology the limiter function is calculated as:-

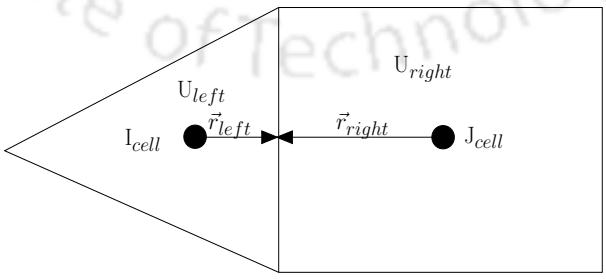

Figure 2.2: Linear reconstruction for the cell centered scheme

$$\psi = \begin{cases} \left[\frac{(\Delta_{1,max}^2+\epsilon^2)\Delta_2+2\Delta_2^2\Delta_{1,max}}{\Delta_{1,max}^2+2\Delta_2^2+\Delta_{1,max}\Delta_2+\epsilon^2}\right] & if \Delta_2 > 0 \\ \left[\frac{(\Delta_{1,min}^2+\epsilon^2)\Delta_2+2\Delta_2^2\Delta_{1,min}}{\Delta_{1,min}^2+2\Delta_2^2+\Delta_{1,min}\Delta_2+\epsilon^2}\right] & if \Delta_2 < 0 \\ 1 & if \Delta_2 = 0 \end{cases}$$

where $\Delta_{1,max} = U_{max} - U_{I_{cell}}$ and $\Delta_{1,min} = U_{min} - U_{I_{cell}}$. Here, U_{max} and U_{min} are the maximum and minimum values of all surrounding cells J, including the cell I itself, and are expressed as:-

$$U_{max} = max(U_{I_{cell}}, max_J U_{J_{cell}})$$
$$U_{min} = min(U_{I_{cell}}, min_J U_{J_{cell}})$$

The term Δ_2 is calculated as $\Delta_2 = \nabla U_{I_{cell}}.\vec{r}_{left}$. Further, the quantity ϵ^2 is defined as $\epsilon^2 = (K\Delta h)^3$. Here, K is a constant of order one (generally taken as 2) and Δh is square root of area in 2-D and cube root of volume in 3-D.

2.5.3 Calculation of viscous fluxes

The calculation of viscous fluxes on the face of a control volume needs knowledge of the flow variables and their derivative at the same location. In the present numerical study, consistency and simplicity in spatial discretization are maintained by keeping same control volume of viscous flux as in case of convective flux evaluation. The flow variables at the faces are estimated by averaging left and right cell values for that face which is attributed to its elliptic nature. Here, the first derivative of flow variable is initially calculated at the cell centre using discrete Gauss divergence theorem [146]. Subsequently, these values are assigned to the nodes of the cell and then they are evaluated at the face by averaging the node values. This procedure avoids the decoupling of evaluated gradients at the boundaries as it usually happens in the simple cell averaging method.

$$U_{IJ_{face}} = U_{I_{cell}} + U_{J_{cell}}$$

2.6 Boundary conditions

The proper implementation of boundary conditions is essential as it may lead to non-physical numerical results. Therefore, care is required for handling of boundary conditions to ensure the well-posed problem. In the present work, different boundary conditions are considered which are mentioned in the following subsection:-

2.6.1 Supersonic inlet

As per characteristics theory [147], all eigenvalues have the same sign for the supersonic inlet. Therefore, all conservative variables are fixed in the inlet according to the freestream primitive variable as the supersonic stream is entering the computational domain.

2.6.2 Supersonic outlet

This boundary condition also has the same sign of eigenvalues. In this case, it is assumed that the flow exits the computational domain with supersonic speed and hence it has no upstream influence. Thus, flow variables at the boundary faces are obtained from the adjacent interior cell using zeroth order extrapolation.

2.6.3 Wall boundary

In the present study, isothermal and adiabatic wall boundary conditions are considered. For both the cases, no-slip condition is implemented at the wall by providing zero normal and tangential velocity relative to the wall surface. Further, wall temperature and mass concentrations are fixed at a known value in isothermal condition while for an adiabatic case, temperature gradients are kept zero and as so the gradients of concentration of any species. The pressure at the wall faces is obtained from the immediate interior cell.

2.6.4 Inviscid wall or symmetry boundary

In this boundary condition, viscous forces adjacent to the wall are neglected and hence fluid freely slips over the surface. The tangential component is non-zero while normal component of velocity is considered zero and as a consequence, wall acts as impermeable. On the other hand, no flux crosses the wall boundary in symmetry condition. Thus, mathematically both boundary conditions are similar although their physical meanings are different. In the present solver, mirror cell approach is used to implement these boundary conditions.

Mirror or Ghost cell approach

This approach provides the freedom to implement interior inviscid flux computation scheme on the wall as it accounts propagation of waves. In this approach, thermodynamic properties and tangential velocity are obtained from the interior flow. However, normal velocity is handled differently. The graphical representation of the approach is shown in Fig. 2.3 and the mathematical formulation is as follows:-

$$u_{normal_{ghost}} = -u_{normal_{interior}}$$

$$u_{parallel_{ghost}} = u_{parallel_{interior}}$$

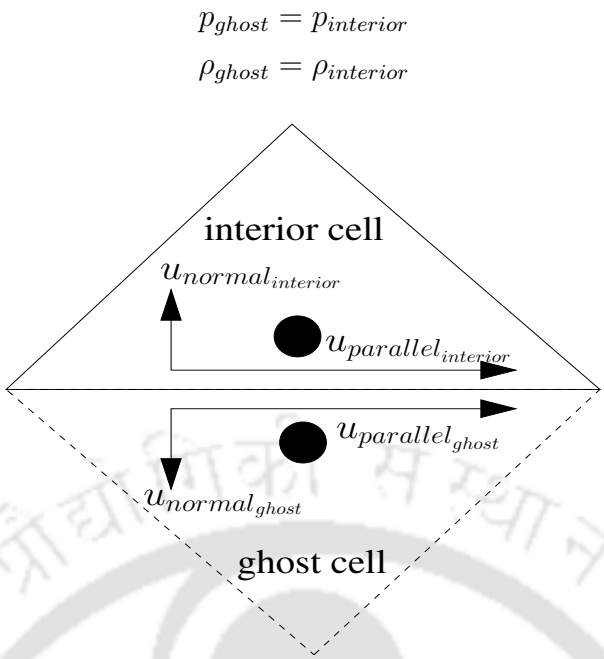

Figure 2.3: Mirror or Ghost cell approach

2.7 Temporal discretization

The temporal discretization is required to get the system of algebraic equations from the ordinary differential equations obtained by the spatial discretization. There are two types of time discretization techniques: one is an explicit method and other is an implicit method. Among these, explicit method is easy to implement where the magnitude of the time step is computed using Courant-Friedrichs-Levy (CFL) condition to obtain the stable numerical solution. Hence, this method has a smaller magnitude of the time step. On the other hand, implicit methods are unconditionally stable and have bigger time step magnitude. Thus, it reduces the overall computational time compared to an explicit method. The present solver is based on semi-implicit time discretization method where source term is treated implicitly. In reacting flows, the time scale of chemical reactions is very low while comparing the flow time scale. Hence, to capture flowfield efficiently, very small time steps are required for explicit simulation. Thus, convergence to steady flow is very slow. Therefore, only source term implicitization is done to increase the time step as given by Bussing and Murman[148]. To illustrate this recalling the Eqn 2.17:-

$$\frac{d\overline{U}_i}{dt} = -\frac{1}{\Omega_i}\sum_{J=1}^{n_f} H_{\perp_J}\,\Delta S_J - \overline{S}_{ci} - \alpha\overline{S}_i = R(\overline{U}_i)$$

It can be written as:-

$$\frac{U_i^{n+1} - U_i^n}{\Delta t} = -\frac{1}{\Omega_i}\Big(\sum_{J=1}^{n_f} H_{\perp_J}\,\Delta S_J\Big)^n - \overline{S}_{ci}^{n+1} - \alpha\overline{S}_i^n \tag{2.18}$$

Here, chemical source term is linearized using Newton's method as:-

$$\overline{S}_{ci}^{n+1} = S_{ci}^n + \left(\frac{\partial S_{ci}}{\partial U}\right)^n \Delta U + O(\Delta U)^2 \tag{2.19}$$

After putting this value in Eqn 2.18, sequential mathematical operations are given from Eqn 2.20 to Eqn 2.23:-

$$\frac{U_i^{n+1} - U_i^n}{\Delta t} = -\frac{1}{\Omega_i}\Big(\sum_{J=1}^{n_f} H_{\perp_J}\,\Delta S_J\Big)^n - \left[S_{ci}^n + \left(\frac{\partial S_{ci}}{\partial U}\right)^n \Delta U + O(\Delta U)^2\right] - \alpha\overline{S}_i^n \tag{2.20}$$

$$\frac{U_i^{n+1} - U_i^n}{\Delta t} - \left(\frac{\partial S_{ci}}{\partial U}\right)^n \Delta U = -\frac{1}{\Omega_i}\Big(\sum_{J=1}^{n_f} H_{\perp_J}\,\Delta S_J\Big)^n - S_{ci}^n - \alpha\overline{S}_i^n \tag{2.21}$$

$$\frac{U_i^{n+1} - U_i^n}{\Delta t} - \left(\frac{\partial S_{ci}}{\partial U}\right)^n (U_i^{n+1} - U_i^n) = -\frac{1}{\Omega_i}\Big(\sum_{J=1}^{n_f} H_{\perp_J}\,\Delta S_J\Big)^n - S_{ci}^n - \alpha\overline{S}_i^n \tag{2.22}$$

$$\frac{U_i^{n+1} - U_i^n}{\Delta t}\left[I - \Delta t\left(\frac{\partial S_{ci}}{\partial U}\right)^n\right] = -\frac{1}{\Omega_i}\Big(\sum_{J=1}^{n_f} H_{\perp_J}\,\Delta S_J\Big)^n - S_{ci}^n - \alpha\overline{S}_i^n \tag{2.23}$$

Here, I is the identity matrix and $\frac{\partial S_{ci}}{\partial U}$ is the Jacobian matrix. The Jacobian matrix $\frac{\partial S_{ci}}{\partial U}$ can be evaluated using below expression:

$$\frac{\partial S_{ci}}{\partial U} = \begin{bmatrix} 0 & 0 & 0 & 0 & 0 & 0 & 0 & 0 \\ 0 & 0 & 0 & 0 & 0 & 0 & 0 & 0 \\ 0 & 0 & 0 & 0 & 0 & 0 & 0 & 0 \\ 0 & 0 & 0 & 0 & 0 & 0 & 0 & 0 \\ \frac{\partial S_1}{\partial \rho} & \frac{\partial S_1}{\partial (\rho u)} & \frac{\partial S_1}{\partial (\rho v)} & \frac{\partial S_1}{\partial (\rho E)} & \frac{\partial S_1}{\partial C_1} & \cdot & \cdot & \frac{\partial S_1}{\partial C_{N-1}} \\ \frac{\partial (.)}{\partial \rho} & \frac{\partial (.)}{\partial (\rho u)} & \frac{\partial (.)}{\partial (\rho v)} & \frac{\partial (.)}{\partial (\rho E)} & \frac{\partial (.)}{\partial C_1} & \cdot & \cdot & \frac{\partial (.)}{\partial C_{N-1}} \\ \frac{\partial (.)}{\partial \rho} & \frac{\partial (.)}{\partial (\rho u)} & \frac{\partial (.)}{\partial (\rho v)} & \frac{\partial (.)}{\partial (\rho E)} & \frac{\partial (.)}{\partial C_1} & \cdot & \cdot & \frac{\partial (.)}{\partial C_{N-1}} \\ \frac{\partial S_{N-1}}{\partial \rho} & \frac{\partial S_{N-1}}{\partial (\rho u)} & \frac{\partial S_{N-1}}{\partial (\rho v)} & \frac{\partial S_{N-1}}{\partial (\rho E)} & \frac{\partial S_{N-1}}{\partial C_1} & \cdot & \cdot & \frac{\partial S_{N-1}}{\partial C_{N-1}} \end{bmatrix}$$

Here, off-diagonal terms of matrix $\frac{\partial S_{ci}}{\partial U}$ are neglected to make easy to inverse the matrix and to save computational time. The elements in the Jacobian matrix, can be evaluated

via following steps from from Eqn 2.25 to Eqn 2.28-:

$$\left.\frac{\partial S_j}{\partial T}\right|_{Ci,i=1...,N-1} = W_j \sum_{i=1}^{N_R} (v_{ij}^{''} - v_{ij}^{'}) \left[\frac{K_{fi}}{T} \left(m_{fi} + \frac{E_{fi}}{R_u T} \right) \prod_{l=1}^{N} n_l^{v_{il}^{'}} - \frac{K_{bi}}{T} \left(m_{bi} + \frac{E_{bi}}{R_u T} \right) \prod_{l=1}^{N} n_l^{v_{il}^{''}} \right] \tag{2.24}$$

$$\left.\frac{\partial S_j}{\partial \rho u}\right|_{\rho,\rho E,C_{i,i=1...,N-1}} = -\frac{u}{\rho C_v} \left.\frac{\partial S_j}{\partial T}\right|_{C_{i,i=1...,N-1}} \tag{2.25}$$

$$\left.\frac{\partial S_j}{\partial \rho E}\right|_{\rho,\rho E,C_{i,i=1...,N-1}} = \frac{1}{\rho C_v} \left.\frac{\partial S_j}{\partial T}\right|_{C_{i,i=1...,N-1}} \tag{2.26}$$

$$\left.\frac{\partial S_j}{\partial C_i}\right|_{\rho,\rho E,C_{i,i=1...,N-1}} = W_j \sum_{k=1}^{N_R} \left[(v_{ki}^{''} - v_{ki}^{'}) \left(\frac{v_{ki}^{'} K_{fk}}{C_i} \prod_{l=1}^{N} n_l^{v_{kl}^{'}} - \frac{v_{ki}^{''} K_{bk}}{C_i} \prod_{l=1}^{N} n_l^{v_{kl}^{''}} \right) \right] - \frac{e_i - e_N}{\rho C_v} \left.\frac{\partial S_j}{\partial T}\right|_{Ci,i=1...,N-1} \tag{2.27}$$

Finally, if all the variables are known at n^{th} time instant then their value can be calculated at $(n+1)^{th}$ time instant with subsequent time marching in Eqn 2.23.

2.8 Gas models

In the present studies, different gas models are wielded to simulate low as well as high enthalpy flowfields and to demonstrate the role of real gas effects in the flowfield modifications. The brief discussion of these models are presented in the following subsections:-

2.8.1 Perfect gas model

This gas model holds calorically perfect gas assumption. This solver is as the one considered by John et al. [4, 123, 134, 135]. Here, specific heat ratio remains constant with temperature which is considered 1.4 for air. This gas model only solves Navier-Stokes equations and can precisely simulate the low enthalpy non-reacting flow. It follows the ideal gas equation of state which is as follows:-

$$p = \rho R T \tag{2.28}$$

Here, p is the pressure, R is the characteristic gas constant, ρ is gas density and T represents the temperature. Further, the expressions to calculate specific internal energy and speed of sound are:-

$$e = RT/(\gamma - 1), a = \sqrt{\frac{\gamma p}{\rho}} \tag{2.29}$$

The viscosity of the fluid is calculated considering Sutherland's viscosity model [149]. The dynamic viscosity can be related to temperature as:-

$$\mu = \mu_{ref}\left(\frac{T}{T_{ref}}\right)^{3/2}\left(\frac{T_{ref}+S}{T+S}\right) \tag{2.30}$$

Here, T_{ref} is the reference temperature and its value is taken 273.15 K. Further, μ_{ref} is viscosity of air at reference temperature which is equal to $17.16\times\ 10^{-6}$ N s/m^2 and S represents Sutherland's constant which is considered as 110.56. The Prandtl number of the fluid is assumed constant in this gas model.

2.8.2 Reacting gas model

As it is known now, the hypersonic flight often encounters high temperature zones where calorically perfect gas consideration turns invalid and high-temperature effects becomes prominent. Thus, the perfect gas model is inappropriate for simulations and hence reacting gas model must be employed to accurately predict the high enthalpy flowfield. This model solves coupled Navier-Stokes and species continuity equations. Further, the thermodynamic and transport properties are calculated as mentioned in section 2.1. The solver discussed in this chapter and exclusively developed for present studies is the reacting gas solver.

2.8.3 Frozen gas model

This gas model accounts for the frozen flows in which reactions do not initiate and process. In this model, thermo-physical properties are calculated similarly to reacting gas models while the chemical reactions are made silent. Hence, only Navier-Stokes equations are solved for efficient simulation of hypersonic frozen flowfield. However, if the freestream is dissociated then it solves all the equations of species continuity without accounting their source term. Necessarily, this solver is part of present solver development. Further, the gas model can also be used for simulation of air flow with the change in specific heats.

CHAPTER 3

DELUSIVE INFLUENCE OF NON-DIMENSIONAL NUMBERS IN CANONICAL HYPERSONIC NON-EQUILIBRIUM FLOWS

Overview

Prime objective of this chapter is validation of the inviscid part of present reacting flow solver. Therefore, four different inviscid flux computation schemes are tested for literature reported test cases like unsteady wave motion in a shock tube and high enthalpy flow over cylinder/sphere. During the assessment, encouraging agreement has been noticed in capturing all the essential flow features in the reacting media. Here, the Rusanov scheme is noticed to be computationally cheaper among all the schemes with noticeable diffusion around the strong gradients. Further analysis of each test case gave exciting information about the flow physics. Shock tube test case revealed the existence of various shock Mach numbers for a given driving pressure ratio in the presence of reactions. Similarly, freestream Mach number is found to have limitations in representing the shock standoff distance in case of high enthalpy flow over cylinder and sphere. In line with this, real gas effects are prominently observed for the case of the cylinder in comparison with the sphere while predicting the complete shock shape using Billig's correlation. Present chapter also portrays the limitations of conventional non-dimensional numbers in predicting flow features and flow properties in the presence of reactions in all the dimensionalities.

3.1 Introduction

Hypersonic aerodynamics retains interest in the research community due to the requirement of faster civil and military transport as well as the need of reusable space vehicles.

Desai, S., Kulkarni, V., Gadgil, H., 2016, "Delusive influence of non-dimensional number in canonical hypersonic non-equilibrium flows", ***Journal of Aerospace Engineering***, vol. 25, 04016030.

Computational fluid dynamics has proven its importance in this flow regime for the design of engines [150, 151] and reentry vehicle aerodynamics [152–154]. However, the presence of high-temperature reacting fluid in the vicinity of the spacecraft adds to the complexities for predicting the flowfield or aerodynamic coefficients using this evolving engineering tool. Although Mach number five is usually considered to segregate this flow regime from others, existence of the special flow features justifies the definition of this flow regime [155]. Hence freestream total enthalpy or kinetic energy is invariantly used to label the freestream variables either in the test section of a ground-based test facility or for a flight test. Such high-temperature hypersonic or hypervelocity flows exhibit presence of two time scales. The first time scale corresponds to fluid convection, and the other one to the reactions. If both the scales are of the same order then such flows are titled hypersonic non-equilibrium flows. Analysis of such flows is highly desirable for proper prediction of aerodynamic coefficients, heating rates, and freestream conditions in test facilities. However, an equilibrium assumption has been invariantly considered to arrive at an engineering estimate due to simplicity of the prediction methodology [156–159]. Besides, development of algorithms and solution procedures for reacting hypersonic flows have been the topics of investigations to improve the prediction ability of this highly desirable tool [160–166]. Sarma [167] has consolidated the efforts of various research studies in this field. Therefore, this chapter is dedicated to validation of currently built reacting flow solver. However, only inviscid part of the solver is accounted for the validation test case discussed herein. The prime objective of these studies is also to understand the possible extension of existing, well appreciated convective flux computation schemes for simulating the reacting flows. Application of these convective flux computation schemes has been reported for supersonic Mach numbers or for non-reacting hypersonic flows [141–144]. Therefore it is highly desirable to consider such widely accepted schemes for hypersonic reacting flows. Comparative study of such flux computing schemes, which is unseen in the literature, is necessary to decide about the choice of scheme for reacting flow applications. Apart from this, the present solver, which is planned to account for structured as well as unstructured grids, can also provide judgment about performance of those schemes in different forms of grid. These efforts would essentially overcome the void in the literature where reported results for standard test cases are found to be with structured grids only. In view of this, simulations are performed to study the high-temperature effect in the canonical problems for planar and axisymmetric flow domains. Benchmarking and validation of present solver are the planned outcomes of this validation studies. Beyond this, all the selected test cases are analysed from gas dynamic perspective to receive the better flow physics. Such investigations are indeed essential to portray the limitations of conventional non-dimensional numbers in holding the dependence of their respective

flowfields. Details of test cases, test conditions and results are presented in following sections.

3.2 Results and discussion

3.2.1 Shock tube problem

A one dimensional (1-D) shock tube test case, given by Shuen et al. [1], is used initially to validate the present reacting solver and onwards to study the real gas effects in it. Shock tube of length 1 cm having equal length of driver and driven sections was the choice for computations of Shuen et al. [1]. Same shock tube domain with 5 mm width has been considered herein and it is meshed with uniform mesh of size 2000×50. Free-slip boundary condition is the obvious choice for all the domain boundaries to retain the dimensionality of the problem. Initial conditions considered for this case are,
Driver section (for $0 \leq x \leq 0.5$cm):

$$p_4 = 100 \text{ atm}, T_4 = 9000 \text{ K}, u_4 = v_4 = 0.0$$

Driven section (for $0.5\text{cm} \leq x \leq 1\text{cm}$):

$$p_1 = 1 \text{ atm}, T_1 = 300 \text{ K}, u_1 = v_1 = 0.0$$

Here, equilibrium composition of air corresponding to respective pressure and temperature conditions has been assigned to the driver and the driven sections [17]. Finite rate chemistry model involving eleven elementary reactions, discussed in chapter 2, is used to model this unsteady reacting flow problem. All the convective flux computation schemes described in chapter 2 are employed for this case study. Thus obtained variation of density and temperature along the shock tube length are shown in Fig. 3.1(a) and 3.1(b). It should be noted here that the results obtained from present simulations for two dimensional computations have encouraging agreement with the literature reported results of 1-D simulation. All the flow features like shock, contact discontinuity and expansion fan are correctly captured by all the schemes. Presence of reactions in this shock tube flow is evident from Fig. 3.1(c) and 3.1(d) which give variation of mole fractions of N and NO along the shock tube length. As per this figure, present reaction modeling is in well agreement with the literature reported results which prominently displays the presence of shock driven dissociation reactions and expansion fan based recombination reactions. All the schemes employed for these computations are found suitable for such simulations except the conventional demerit of Rusanov scheme which is more diffusive among the others [168]. It should be noted here that the mole fraction of NO shows sharp raise across the shock. Hence, presence of NO is prominent behind the strong shock. Thus, a

contact or non-contact type sensor which is based on detection of NO for location of the shock in the driven section of the shock tube can be primarily thought for shock speed measurement.

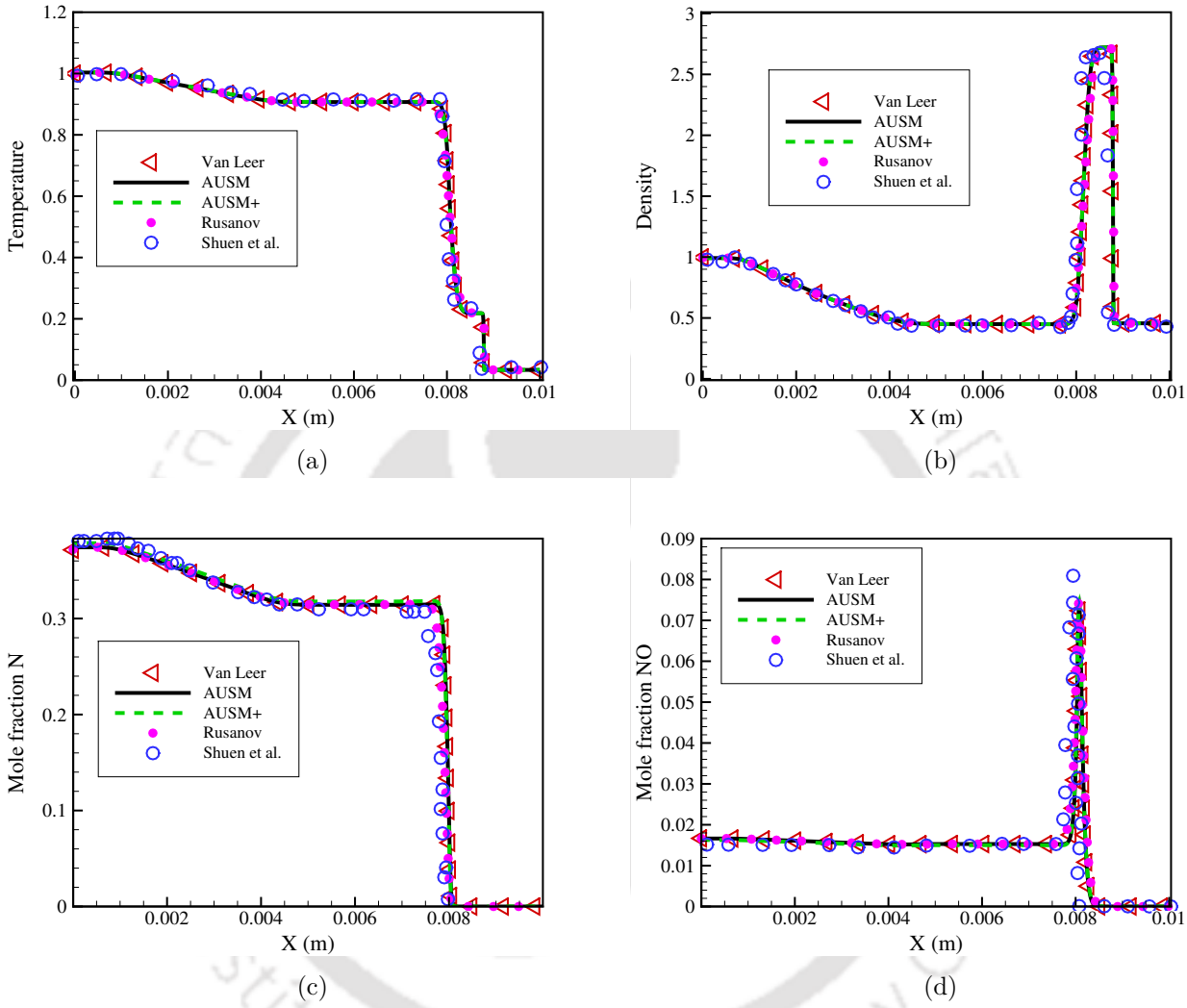

Figure 3.1: Comparison of flow properties in the shock tube with Shuen et al. [1]. The properties in 3.1(a) and 3.1(b) are normalized by the corresponding driver section values and the physical time is 1.9 microseconds.

After successful validation of the present solver, simulations are further extended in the same computational domain to analyse the effect of absolute pressures of driver and driven sections on the shock speed. In this phase, the pressure ratio and temperature ratio between driver and driven sections are maintained constant. The temperatures of driver and driven sections are kept same as mentioned in validation case. However, the absolute pressures on either side of the discontinuity are given in Table 3.1. Here, perfect gas case is referred to the simulations which are carried out for ideal conditions assuming

air with constant specific heat ratio (γ=1.4) in driver and driven sections. For each case, shock speed is obtained in terms of shock Mach number based on the thermodynamic properties in the driven section of shock tube. Location of the shock after fixed time intervals is detected in each case to derive the shock speed. It is observed that the shock speed is constant (non-accelerating) as that for the perfect gas but different in each case, which conflicts with the perfect gas case. Therefore, the value of the shock Mach number is different from what one should get under perfect gas assumptions for a given pressure and temperature ratios. More precisely, the reacting gas case shock Mach number which ranges between 5.76 and 5.9 is found to be more than the one in perfect gas flow which is 5.25 with same pressure and temperature ratios. This shock speed enhancement leads to significant pressure rise (≈33%) and temperature rise (≈12%) behind the shock. Such real gas effects need to be considered while designing such experiments in the shock tube.

Table 3.1: Comparison of shock Mach numbers in perfect gas model and real gas model

Driver section pressure	Driven section pressure	Shock Mach number	Shock Mach number
P_4 (atm)	P_1 (atm)	Reacting gas case	Perfect gas case
100	1	5.74	
10	0.1	5.88	5.25
1	0.01	5.79	

Simulations for the test conditions of Table 3.1 hint about the possible role of the intensity of the chemical reactions in altering the shock speed with change in absolute pressure for same pressure ratio. This is inconsistent with the well-accepted fact for calorically perfect gas that there exists a unique shock Mach number for a given pressure ratio between driver and driven sections. A close look at Fig. 3.2(a) justifies this fact. It shows that the decrease in temperature in the driver section due to expansion promotes recombination reactions (for example N -> N_2) resulting in formation of N_2. Recombination reaction being inherently exothermic releases heat, thereby compensating fall in temperature due to expansion. This recovery of temperature is evident from the elevated plateau regions in Fig. 3.2(a) for all the reacting cases in comparison with perfect gas case. Since the energy in the driver section is responsible for driving the shock, release of heat from recombination reactions provides additional forcing for the shock wave. This physical phenomenon can be seen qualitatively analogous to a detonation wave. This is in complete contrast with perfect gas based shock tube flow wherein the expansion is adiabatic. Therefore the reacting (heat-releasing) driver section, in the present cases, is noticed to be a source to enhance the shock speed in comparison with the perfect gas

htbp]

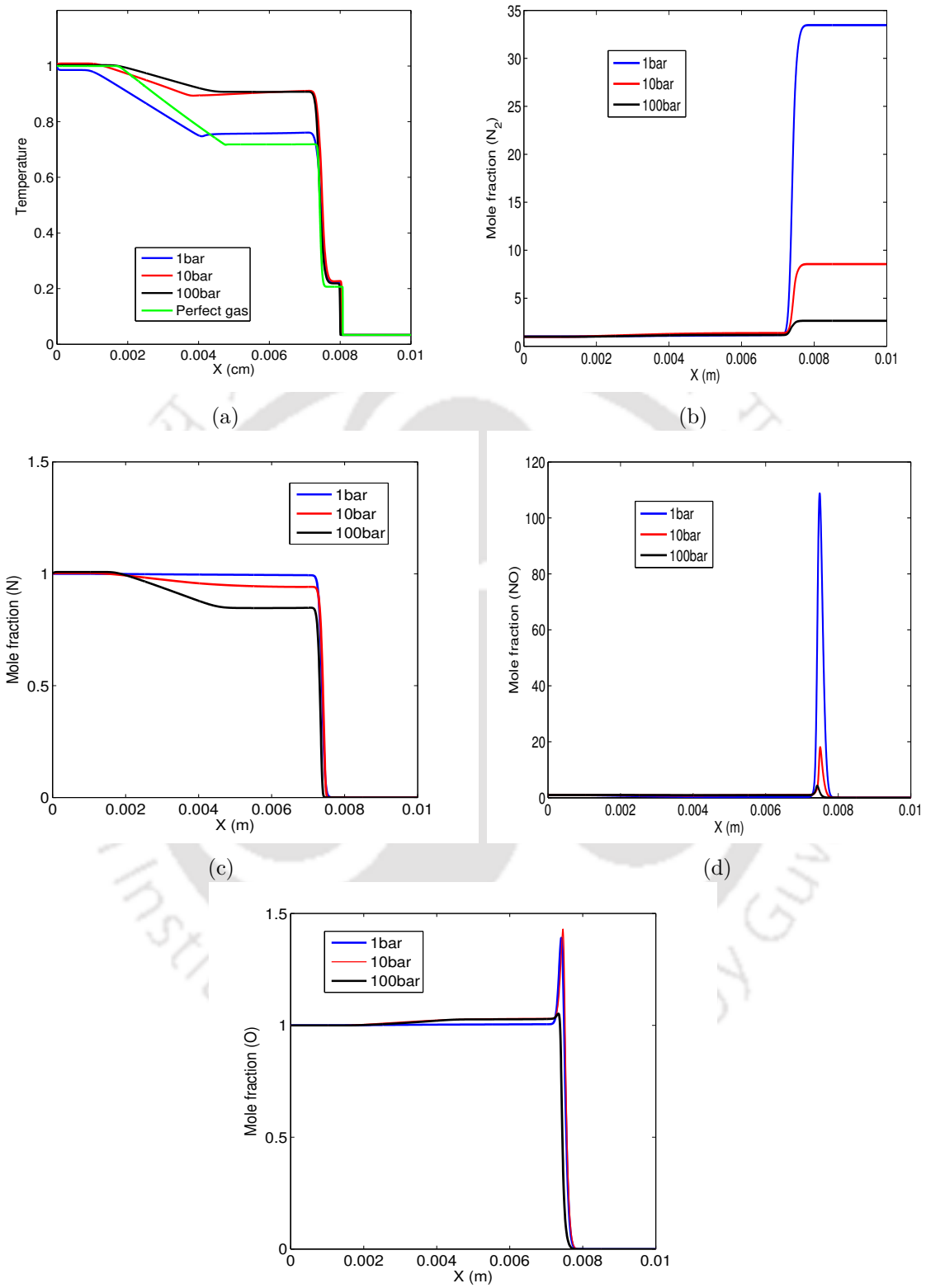

Figure 3.2: Effect of absolute pressures on the variation of properties in the shock tube. The properties are normalized by the corresponding driver section values.

conditions. However, this enhancement is limited by the amount of energy getting consumed behind the shock in endothermic reactions like dissociation (Fig. 3.2). Presence of NO behind the shock justifies this reasoning (Fig. 3.2(d)). From present simulations, highest shock Mach number has been noticed for the driver section pressure of 10 bar and the least shock Mach number for 100 bar condition. Absolute values of driver and driven section pressures influence the relative strengths of the recombination and dissociation reactions. Thus, the absolute values of these pressures are found to be important in deciding the shock speed at a given temperature ratio and not the ratio of theirs as in case of perfect gas. From the mass fractions of NO and N_2, relative dominance between driver section based recombination reactions and shock induced dissociation reactions is noted as the possible reason for this discrepancy. Mole fraction for NO also suggests that the possibility of NO formation increases with decrease in driven section pressure. Therefore the above mentioned 'sensors in thought' for shock speed measurement are going to be prominently useful for low driven section pressure conditions.

3.2.2 Hypersonic reacting flow over cylinder and sphere

Hypersonic flow over cylinder has been considered by Shuen [169] and Ratan [2] as test case in the developmental phase of their solvers. Same test case has been considered herein initially to verify the results obtained from various schemes through the comparison with literature reported results. In this simulation, a half cylinder of 10 cm diameter is considered and the corresponding fluid domain is discretized using mesh of size of 96×62 [2, 169]. The freestream conditions employed for present simulations are Mach 7, temperature 600 K and pressure 1 atm. Literature reported results of Shuen [169] obtained using Van Leer scheme are considered for comparison at stagnation point while the Roe scheme based results of Ratan [2] are considered for surface profile assessment. Cylinder wall properties obtained using various schemes are shown in Fig. 3.3. Excellent agreement in pressure variation obtained from various schemes of the present solver with the reference results [2, 169] is evident from Fig. 3.3(a). Although temperature variation follows the same trend as that of Ratan, it may be noted from Fig. 3.3(b) that the local magnitudes of temperature are scheme dependant. Prediction of lower stagnation temperature by Rusanov scheme reaffirms the diffusive nature of the scheme. Figures 3.3(c) and 3.3(d) depict typical distribution of species mass fractions on the cylinder wall. Although the trend of variation is matching, the species distribution is also found to be scheme dependent particularly in the vicinity of stagnation point. However, the results are self-consistent within the formulation of a particular scheme. For example, lower stagnation temperature in Rusanov scheme also predicts relatively lower NO and O mass fractions. It is worth to mention here that similar agreements have been obtained

for the mass fractions of other species. The comparison of convergence histories of various flux computation schemes is shown in Fig. 3.4. It may be noted that the convergence of AUSM and AUSM+ schemes is oscillatory and require more iterations to converge as compared to other two schemes.

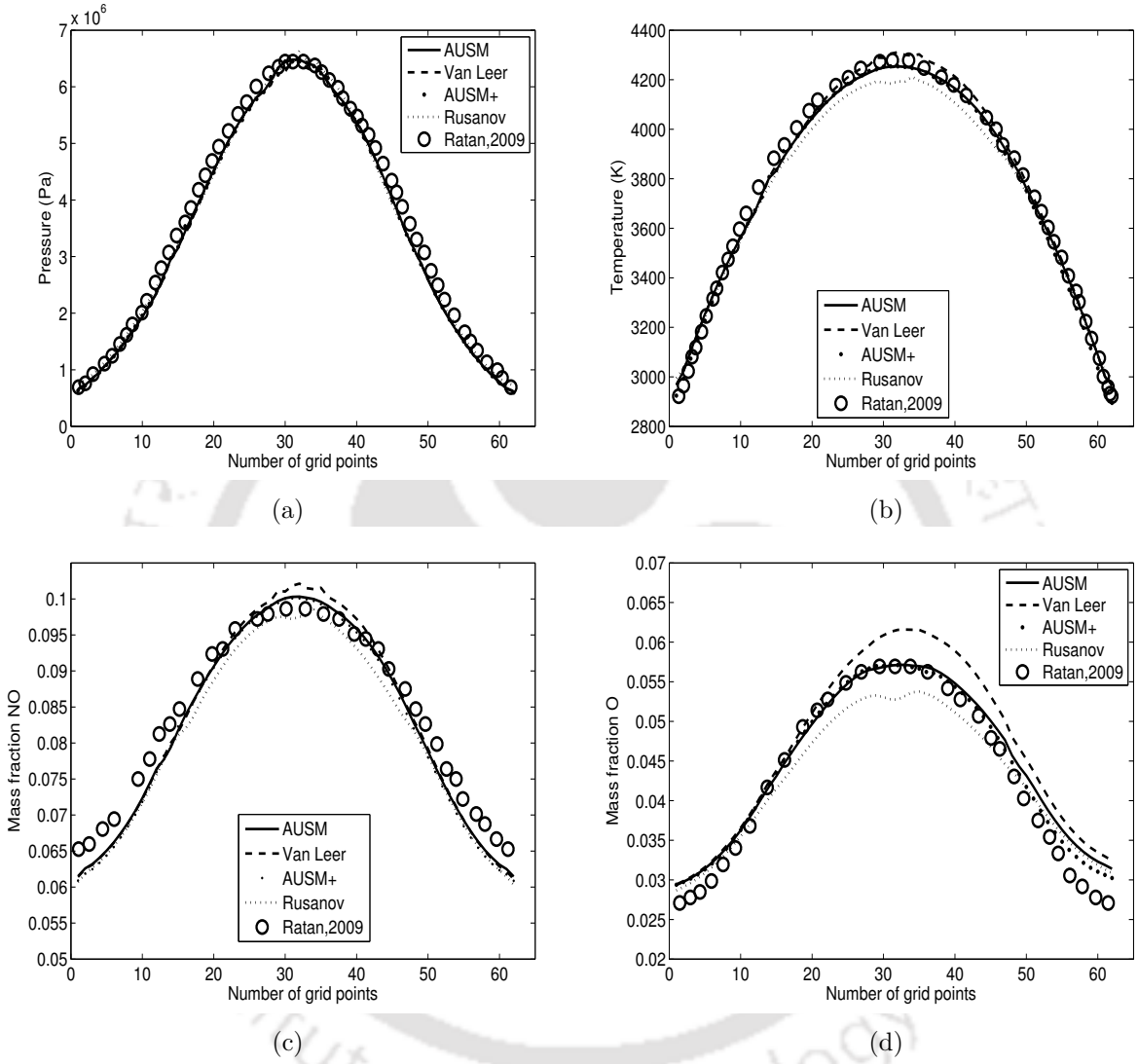

Figure 3.3: Typical variation of flow properties on the cylinder wall (The abscissa denote the grid point locations along the cylinder surface). The comparison is made with the results of Ratan [2].

Same freestream conditions are considered to demonstrate the unstructured mesh handling capacity as well as axisymmetric formulation of the present solver. In view of this, hypersonic flow over only quarter portion of the cylinder is considered to account for the axisymmetricity of the computational domain. In one case, this domain is meshed with structured mesh of size 200×200 while in other case 58088 triangular elements are used to mesh the computational domain in unstructured manner. These two grids are

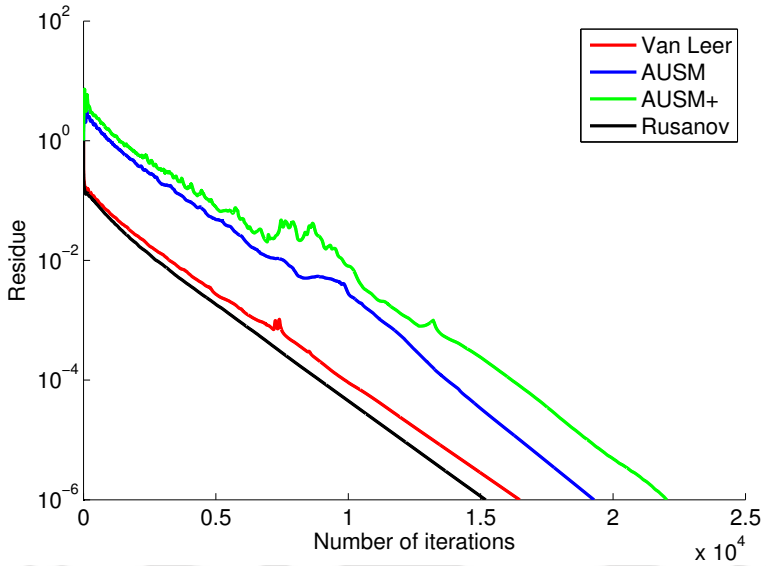

Figure 3.4: Residue history of various schemes for the flow over cylinder with CFL number 0.1. The freestream conditions and grid size are same as those in Fig. 3.3.

shown in Fig. 3.5. Same domains are considered with the same freestream conditions to compute for the hypersonic flow over a quarter sphere by assuming the line of symmetry as the axis of sphere. Thus obtained results for cylinder and sphere cases for unstructured and structured meshes using AUSM scheme are compared in terms of pressure contours in the Fig. 3.6. Solution obtained from the unstructured mesh is seen to be in well agreement with the corresponding one obtained from structured mesh. This comparison strongly supports the unstructured mesh handling capability of the present solver. Three dimensional relieving effect is also clearly evident from this figure since shock is closer to the stagnation point for the sphere than for the cylinder. During the axisymmetric computations as well, encouraging agreement can be depicted between the structured and unstructured simulations.

3.2.3 Real gas effect on shock stand off distance and shock shape

Real gas effects on the shock stand-off distance (δ) and shock shape in case of hypersonic flow over cylinder and sphere have also been part of present investigations. Shock stand-off distance and shock shape are invariantly obtained from the Billig correlations given below [3].

$$x = R + \delta - R_c \cot^2 \beta \left[\left(1 + \frac{y^2 \tan^2 \beta}{R_c^2} \right)^{1/2} - 1 \right] \tag{3.1}$$

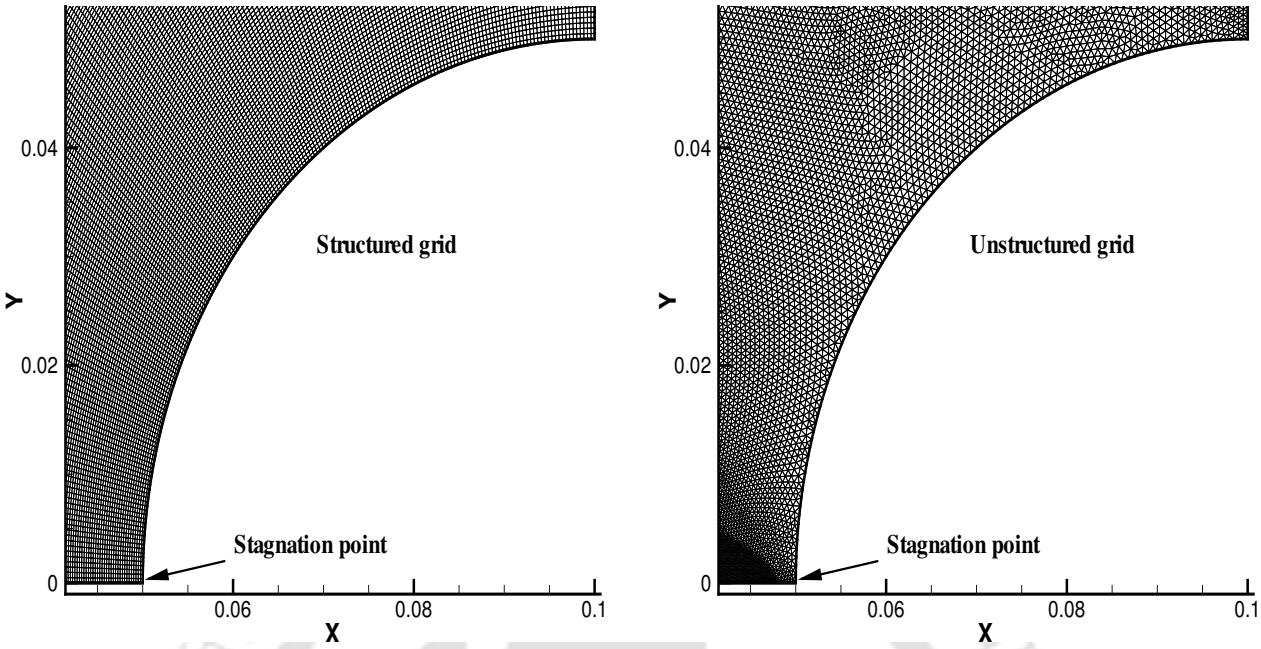

(a) Structured grid (b) Unstructured grid

Figure 3.5: Types of grid used to validate the unstructured formulation of the solver.

where

$\frac{\delta}{R} = 0.143\exp(3.24/M^2)$: Sphere-cone configuration

$\frac{\delta}{R} = 0.386\exp(4.67/M^2)$: Cylinder-wedge configuration

$\frac{R_c}{R} = 1.143\exp[0.54/(M-1)^{1.2}]$: Sphere-cone configuration

$\frac{R_c}{R} = 1.386\exp[1.8/(M-1)^{0.75}]$: Cylinder-wedge configuration

In equation 3.1, R is the radius of cylinder/sphere, R_c is the radius of the curvature of the shock wave at the vertex, x and y are co-ordinates of the shock wave and β is the angle of the shock wave in the limit of an infinite distance away from the nose of the blunt body.

This section deals with real gas effects and associated alterations in shock related parameters. The computational domain and the structured mesh chosen for quarter cylinder/sphere test cases, discussed earlier, have been employed here. Computations are performed for both the configurations (cylinder and sphere) using AUSM scheme for freestream Mach number ranging from 4 to 10. Two freestream temperatures of 100 K and 600 K are chosen to elaborate the real gas effect due to change in freestream total enthalpy of the flow. Perfect gas solver [168] has also been used with freestream temperature of 100 K to obtain the shock standoff distance and shock shape for calorically perfect gas case. Comparison of thus obtained shock stand-off distance and shock shape is carried out using Billig's correlation [3] for cylinder as well as sphere as given in

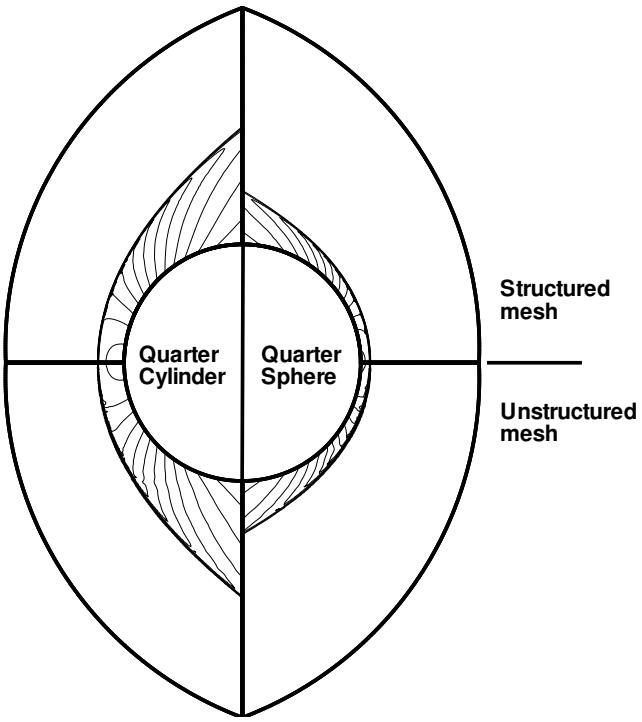

Figure 3.6: Comparison of shock prediction for quarter cylinder/sphere using structured and unstructured formulations.

Eq. (3.1). It is clear from these equations that only freestream Mach number is the governing parameter for predicting the standing shock location and its shape. Hence it is interesting to verify this fact in the presence of reacting flow. Therefore, the variation of shock stand-off distance, measured along the stagnation line, with Mach number for various gas models is shown in Fig. 3.7. It may be observed from figures 3.7(a) and 3.7(b) that the shock stand-off distance for perfect gas (T_∞ = 100 K) case matches well with Billig's correlation. Additionally, results for all the freestream temperatures follow the conventional trend of decrease in shock stand-off distance with increase in Mach number for both configurations. Expected decrement in shock stand-off distance for sphere in comparison with the cylinder of same radius and for same freestream conditions can also be perceived from these figures. Notably, deviation of the present predictions from Billig correlation is prominent as real gas effects are introduced in the simulations. At low freestream temperature (100 K), the maximum temperature behind the shock is not so high as to trigger reactions, but it is high enough to make calorically perfect gas assumption invalid (i.e. C_p,C_v = f(T)) at least at relatively high Mach numbers.

Therefore, deviation in shock stand-off distance from Billig's correlation (Fig. 3.7(a)) and prediction from the prefect gas model is found significant for freestream Mach number of 8 and onwards which can be attributed to temperature dependant specific heats. As the freestream temperature is further increased to 600 K, temperature in the stagnation region is expected to reach to level where air starts dissociating for lower Mach number flows too. Thus the deviation in predictions is expected to encounter at lower Mach number and same is seen in Fig. 3.7(a) from Mach number 4. As a result of this, present simulations assert that the Mach number alone is not sufficient to predict the shock stand-off distance accurately and total enthalpy of freestream plays a significant role in shock stand-off prediction for reacting high enthalpy flows.

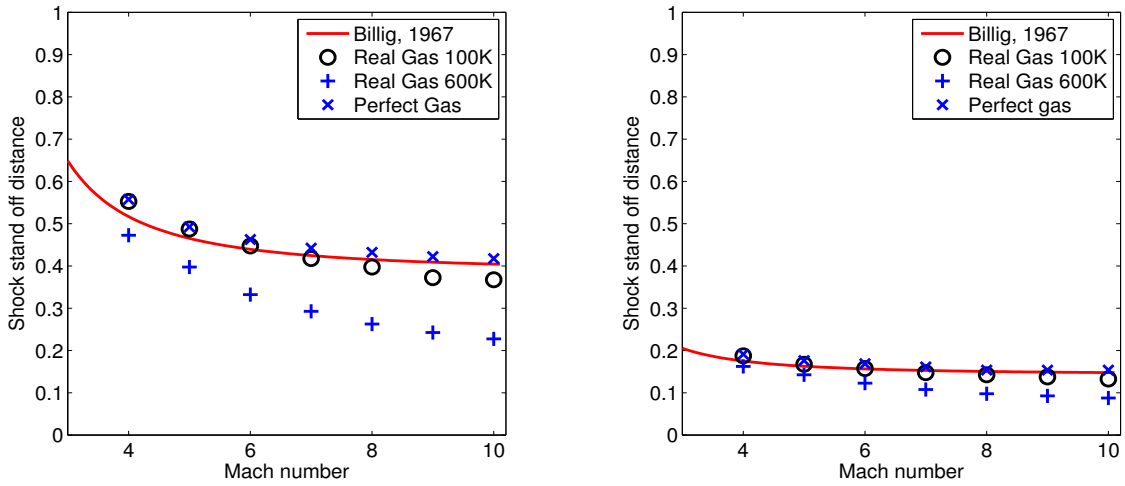

(a) Cylinder (b) Sphere

Figure 3.7: Effect of reacting gas flow on shock stand off distance showing deviation from Billig correlation [3]. The shock stand off distance is normalized by the corresponding radii of cylinder and sphere.

Another important feature of this flow is the shape of the shock for which a comparative study is presented in Fig. 3.8. Shock shape, like shock stand off distance, may be expressed in terms of Mach number only as shown in Eq. (3.1). Two extreme Mach number cases (4 and 10) are chosen for two different freestream temperatures (100 K and 600 K). For a freestream temperature of 100 K, it may be noted that the computed shock shape is in good agreement with the shock shape obtained from Billig correlation (Eq. (3.1)). Chemical reactions are negligible and the real gas effects are also not significantly altering the shock shape. For freestream temperature of 600 K, the real gas effects are not significant for low Mach number of 4 as shown in Fig. 3.8(a) and 3.8(c). However, the strong real gas effects in pulling the shock towards the body may be observed in Fig. 3.8(b) and 3.8(d) where the total enthalpy of freestream is relatively high due to

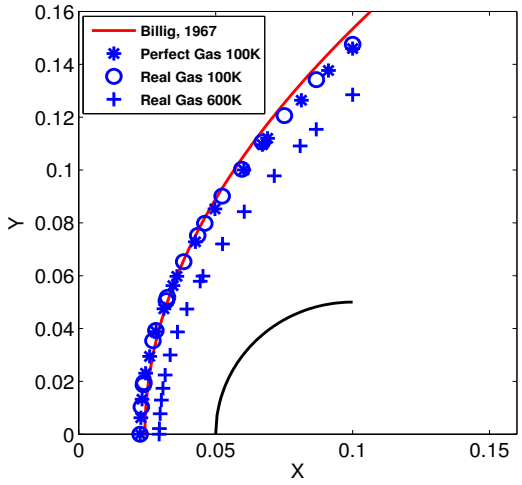

(a) Cylinder Mach 4

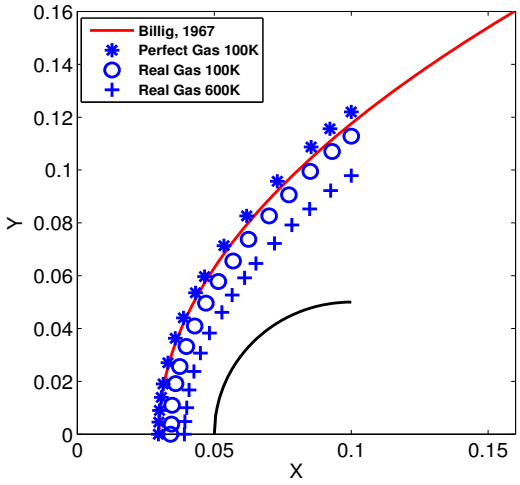

(b) Cylinder Mach 10

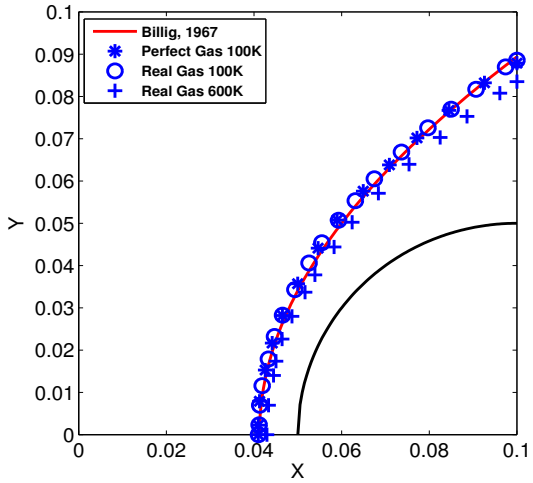

(c) Sphere Mach 4

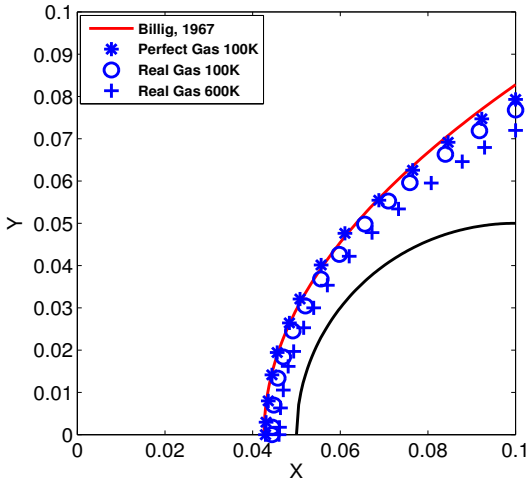

(d) Sphere Mach 10

Figure 3.8: Real gas effect on shock shape in comparison with Billig correlation [3].

high Mach number of 10. Thus, total enthalpy of freestream along with Mach number influences the shock shape prediction in reacting flow. It should not go unnoticed from Fig. 3.7 and 3.8 that the real gas effects on hypersonic flowfield is prominent for cylinder as compared with the flow over sphere.

3.3 Conclusion

Validation of unstructured, finite-volume Euler solver is presented in this chapter for hypersonic flows involving strong chemical reactions. The developed solver is equipped with four different flux computation schemes which are first time tested rigorously. This

in-house solver is validated for canonical test cases like unsteady wave propagation in shock tube, two dimensional and axisymmetric flows. While comparing the results of different schemes, it has been noticed that the Rusanov scheme is more diffusive but has faster convergence. The effects of chemical reaction on the flow features in these canonical flows are further explored to arrive at important insights. The significant underlying principle in all the results is that the chemical reactions, being strongly dependent on the pressure and temperature, alter certain flow features that are known to be insensitive to the absolute thermodynamic properties. In shock tube flow, the shock speed is found to be sensitive to the absolute pressures in driver and driven sections (ratio being constant). In case of cylinders and spheres, the shock stand-off distance and the shock shape are found to be no longer governed by Mach number only, rather the influence of freestream enthalpy is found critical. Thus, the use of conventional non-dimensional parameters in predicting the flow features must be made with caution particularly in chemically reacting flows.

CHAPTER 4

AEROTHERMODYNAMIC CONSIDERATIONS FOR ENERGY DEPOSITION BASED DRAG REDUCTION TECHNIQUE

Overview

In this chapter, investigations are carried out for understanding the real gas effects for energy deposition based drag reduction technique for hypersonic flow over a blunt body. Computations are performed to compare the effectiveness of this active drag reduction technique using perfect, frozen and reacting gas flow models. It has been noticed that the deposited energy gets utilised more effectively in case of perfect gas flow. A loss up to 15% is observed in percentage drag reduction as a consequence of real gas effects over the range of energies considered herein. At low levels of deposited energies, drag predicted for frozen and reacting flows agrees well; however differences are observed at higher energy levels. It is concluded that change in specific heats with temperature plays a dominant role at low energy levels and chemical reactions at higher energy levels. The study is further extended to see the effect of energy density and freestream total enthalpy. A significant reduction (up to 74%) in power effectiveness is noticed as the total enthalpy of freestream increased. The present studies also revealed that requirement of non-dimensional energy for attaining peak power effectiveness has close match at different stagnation enthalpies.

Desai, S., Kulkarni, V., Gadgil, H. and John, B., 2017, "Aerothermodynamics considerations for energy deposition based drag reduction technique", ***Applied Thermal Engineering***, vol. 122, pp. 451-460.

4.1 Introduction

Hypersonic flights through the atmosphere pose distinctive challenges to aerodynamicist. One of those is excessively high aerodynamic heating which is the characteristic feature of hypersonic flights. Therefore it becomes highly desirable to incorporate some cooling techniques for the flight safety [170, 171]. Provision of leading edge bluntness reduces the heat load, hence it is advisable to have blunt-nosed spacecraft. Therefore with different cooling strategies, blunt nosed profiles are invariantly proposed to lower the surface heating rates. But penalty of using such aerodynamic design is significant rise in the wave drag incurred by the spacecraft. Therefore active or passive drag reduction techniques need to be devised to lower the fuel requirement and to reduce the cost per flight. Implementation of spike at the nose [172], multi-step base [87] and surface coating of chromium [58] are some passive drag reduction techniques. Counter-flow sonic or supersonic jet [86] and energy deposition [51] form a group of active drag reduction techniques. It may also be noted that, the energy deposition is implemented for flow control as well [50]. In view of this, it has attracted many researchers to develop associated experimental setups or numerical techniques. Nevertheless, this chapter deals with the drag reduction aspect of energy deposition technique.

Various literature reported findings about energy deposition based drag reduction technique are discussed in the chapter 1. Most of those findings are about quantification of drag reduction, effect of location of energy deposition, assessment of the technique, development of set-up and studying unsteady interactions. However, very few studies consider the real gas effects while investigating for drag reduction with energy deposition, although this effect is one of the important aspects in aerothermodynamics of hypersonic vehicles. In such cases, moderate amount of focused energy deposition can trigger real gas effects by introducing dependence of specific heats on temperature. Furthermore, possibilities of chemical reactions in the region of energy spot and shocks complicate the flowfield in the vicinity of the object. In such scenario, predictions based on perfect gas assumptions tend to produce erroneous estimates of drag reduction and effectiveness of this technique. Moreover effectiveness of this technique is dependent on the absolute energy density and freestream stagnation enthalpy or on the relative strength of deposited energy in reference with the freestream stagnation enthalpy. In view of this, it is highly desirable to explore the real gas effects for various energy densities and also for various freestream stagnation enthalpies independently. Therefore, simulations are performed with reacting, perfect gas and chemically frozen versions of solver. These simulations would also help to compare the results of three gas flow models. Such comparison is required to assess the relative dominance of reacting gas flow on the effectiveness of this technique. Details of CFD simulations, underlying gas dynamics and proposed comparison are discussed in

the following sections of this chapter.

4.2 Validation

Additional, validation of the solver for reacting and perfect gas is carried out using the experimental results of Nonaka et al. [36]. For the same purpose, inviscid version of the reacting and perfect gas solvers are employed for flow past a sphere of radius 15 mm for which freestream parameters are tabulated in the Table 4.1. In the present study, AUSM scheme is used to compute the inviscid or convective fluxes. Numerical simulations are performed in body fitted mesh containing 70×90 number of cells. The shock layer thickness obtained from different solvers are plotted along with experimental result in Fig. 4.1. Encouraging match between results obtained from present reacting solver and the literature reported experiment is evident from this figure. Moreover, this figure highlights the role of real gas effects associated with reacting gas case by demonstrating thinner shock layer compared to perfect gas flow. Here, perfect gas solver also shows good agreement with the Billig correlation [3].

Table 4.1: Details of freestream conditions for validation with the experimental result

Velocity km/s	Pressure atm	Temperature K	Mass fraction (N_2)	Mass fraction (O_2)
2.61	2240	293	0.767	0.233

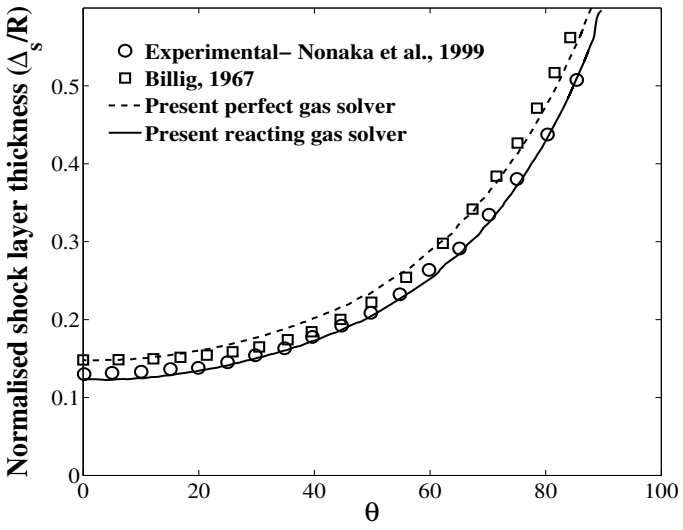

Figure 4.1: Comparison of experimentally and numerically obtained shock layer thicknesses

4.3 Results and discussions

4.3.1 Flowfield with energy deposition

Hypersonic flow over the sphere forms a bow shock wave which remains the source of high pressure and in turn high drag force. Addition of energy upstream of the shock introduces a disturbance in the hypersonic stream. Weak oblique shocks originate from the disturbance and a low pressure recirculation zone gets established ahead the sphere. Such shock-restructuring and associated changes in the flowfield alter the pressure distribution on the surface of the sphere and consequently reduce the drag. However, alterations in the shock structure should be dependent on fluid and flow properties. In view of this, simulations are carried out with three gas flow models viz. perfect gas flow, frozen flow and reacting flow models with and without energy deposition. In this case, a sphere of radius 30 mm is considered in the hypersonic freestream. Details of the hypersonic flow are given in Table 4.2. These conditions were also used by John and Kulkarni [173]. The considered freestream composition in terms of mass fraction of N_2 and O_2 are 0.765 as well as 0.235 respectively for both frozen and reacting gas models. The inviscid flow solver considered in chapter 3 is used for present studies with energy deposition. Here, addition of 7 W of energy is considered uniformly in the sphere of radius 1 mm. Centre of this hot spot or energy spot is chosen on the stagnation streamline at a distance of 60 mm upstream of the stagnation point. The problem configuration is shown schematically in Fig. 4.2. Prior to detailed investigations, a grid independent study is performed using perfect gas solver. Therefore, different grid configurations of size 200×70, 220×100, 250×120, 300×170 are tested herein for conditions described earlier. The drag coefficient (C_d) calculated from these simulations are mentioned in Table 4.3. Here, not much significant change in drag coefficient values are visible after 200×70 grid resolution. Therefore, grid of size 250×120 is chosen for present numerical studies.

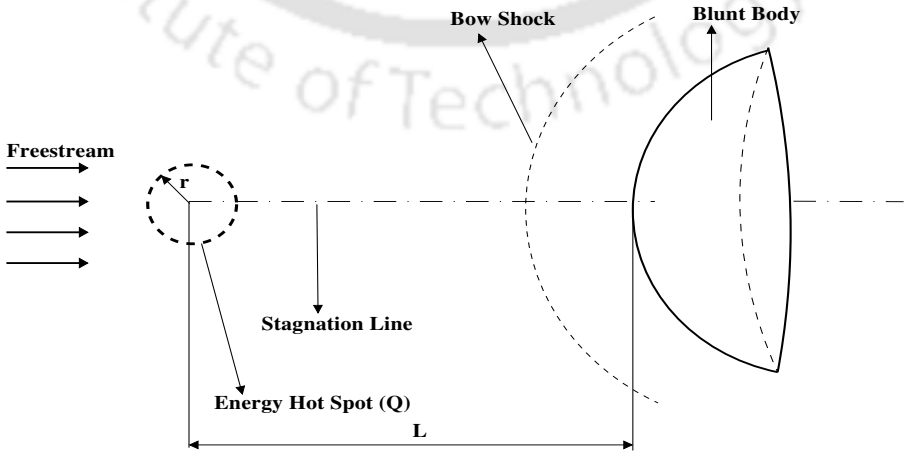

Figure 4.2: Schematics of energy deposition technique

Table 4.2: Details of freestream conditions

Mach number	Pressure Pa	Temperature K	Mass fraction (N_2)	Mass fraction (O_2)
8	89	113	0.765	0.235

Table 4.3: Details of grid independent study (Perfect gas flow- 7 W)

Grid size	$\mathbf{C_d}$
200×70	0.8616
220×100	0.7383
$\mathbf{250 \times 120}$	0.7500
300×170	0.7385

Further, pressure contours for perfect and reacting flow models are shown without energy deposition in Fig. 4.3. Minor decrement in shock stand-off distance is evident here for the undisturbed hypersonic flow over sphere with real gas effects. However addition of energy shows prominent distinctions for these two gas flow models in Fig. 4.4. Flowfield observed for frozen flow model is same as that for the reacting flow model, hence it is not shown in terms of contours. In Fig. 4.4 as well, delayed appearance of oblique shock is evident for the reacting flow model. Apart from this, the shock attachment point on the sphere surface is noted to be upstream for this gas flow model in comparison with the ideal one. Therefore the separation zone formed due to energy addition shrinks in size in case of real gas. As a result of this, the pressure in the separation bubble is found to be higher for this gas flow model. This fact is apparent from the surface pressure distribution shown in Fig. 4.5. Upstream shock attachment and higher pressure at the shock attachment location are evident from this figure. Thus the real gas effects lead to less drag reduction in the presence of this active drag reduction technique. Implications of these real gas effects are discussed in following sections.

4.3.2 Effect of strength of energy spot

Simulations are carried out to study the real gas effects associated with strength of the energy spot. For this, energy deposition is considered at a distance (L) 60 mm upstream of the stagnation point. Hypersonic flow properties, given in Table 4.2, are used for present studies. Strength of the energy spot is varied from 0 W to 150 W in the same location and for same freestream conditions. The maximum strength under consideration is restricted here by validity of polynomial relation between specific heat and temperature [17] in case

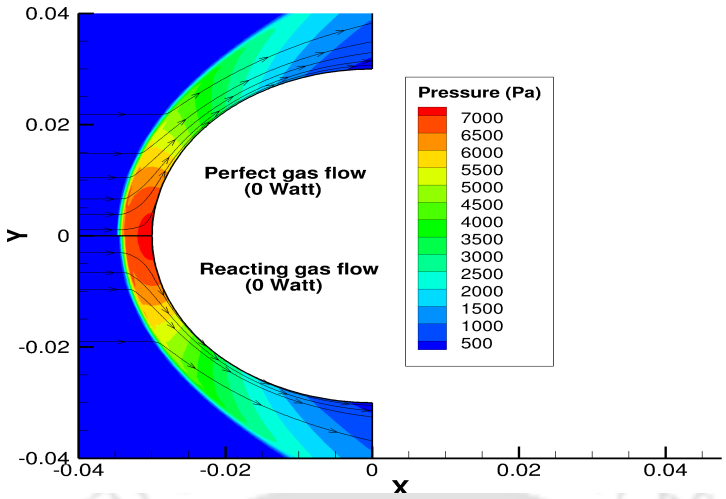

Figure 4.3: Flowfield without energy addition for perfect and reacting gas flow models

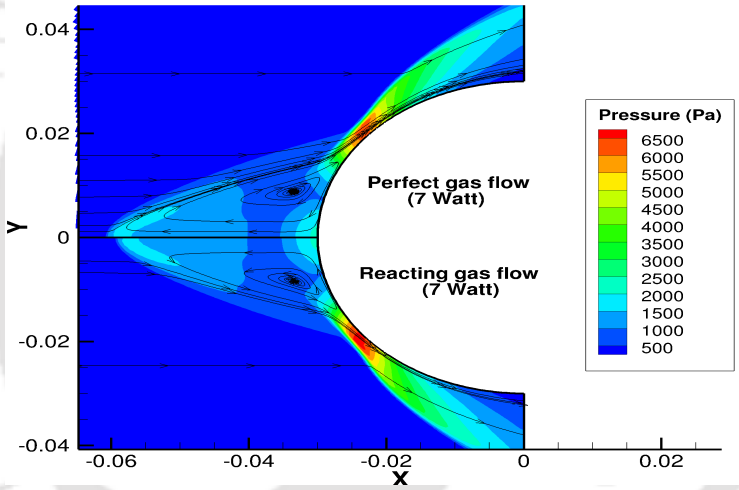

Figure 4.4: Flowfield with energy addition for perfect and reacting gas flow models

of frozen and reacting flows. However such constraint is not applicable for perfect gas flow model. Drag offered by the hypersonic stream to the sphere is evaluated from surface pressure distribution as an outcome of these simulations. Here, Fig. 4.6(a) shows the percentage drag reduction for change in relative strength of the energy source for different gas flow models. It can be seen that amount of drag reduced monotonically increases with increase in amount of energy. Moreover, rate of drag reduction is higher for initial change in energy strengths. It is evident from Fig. 4.6(a) that maximum reduction in drag is obtained for perfect gas flow model for a given amount of energy deposition while the other two gas flow models have marginal difference in their prediction. However, the difference in percentage drag reductions for frozen and reacting flow models increases with the strength of energy deposition. This may be attributed to the fact that chemical

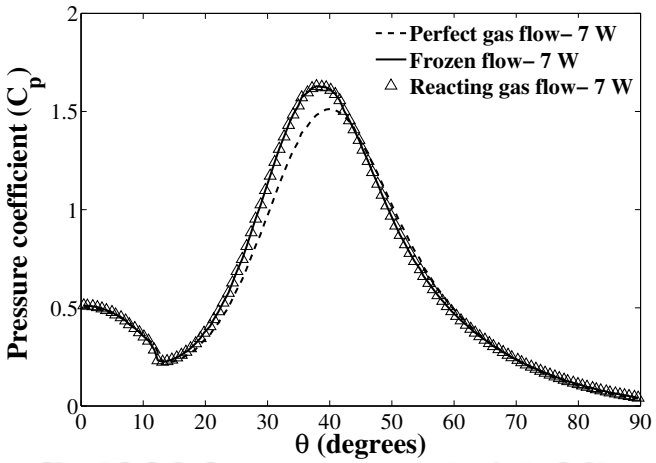

Figure 4.5: Effect of gas flow model on surface pressure distribution on sphere with energy deposition

reactions take over the change in specific heats with the temperature at higher energy densities. Maximum reduction in drag, for any amount of energy deposition, is evident for perfect gas flow model while the other two gas flow models have marginal difference in their prediction. Perfect gas model predicts maximum reduction in drag to be 38.5% while, the same prediction is 35.4% for frozen gas model and 33.8% for reacting gas model for 150 W (Q_n= 9×10^{-3}) of energy. Here, Q_n is the non-dimensional energy deposited and it is the ratio of energy deposited in W to the flow energy ($\rho_\infty A_s U_\infty H_o$). Power effectiveness ($P$), given by Eq. 4.1, is also considered to quantify effectiveness of deposited energy in reducing the drag.

$$P = \frac{(D_O - D)U_\infty}{Q} \tag{4.1}$$

Variation of power effectiveness with relative strength of energy source is shown in Fig. 4.6(b). Observations made from Fig. 4.6(a) can be justified using this figure. For all gas flow models, initial increment in strength of energy source increases the power effectiveness till it attains the maximum value for particular source strength. Beyond this critical point, effectiveness of energy decreases with further increase in strength of energy source. It is seen in Fig. 4.6(b) that 7 W (Q_n= 4.2×10^{-4}) is the most effective energy strength among the given choices, for given freestream conditions and location of energy deposition for all the gas flow models. However, the peak power effectiveness for the perfect gas (315.19) is higher than that for the frozen (263.84) and reacting (263.84) gas flow models. This observation is consistent with the fact noted in Fig.4.6(a) that the percentage drag reduction for same strength of the energy source is higher for the perfect gas flow model than for the frozen or reacting models. Thus the real gas effects

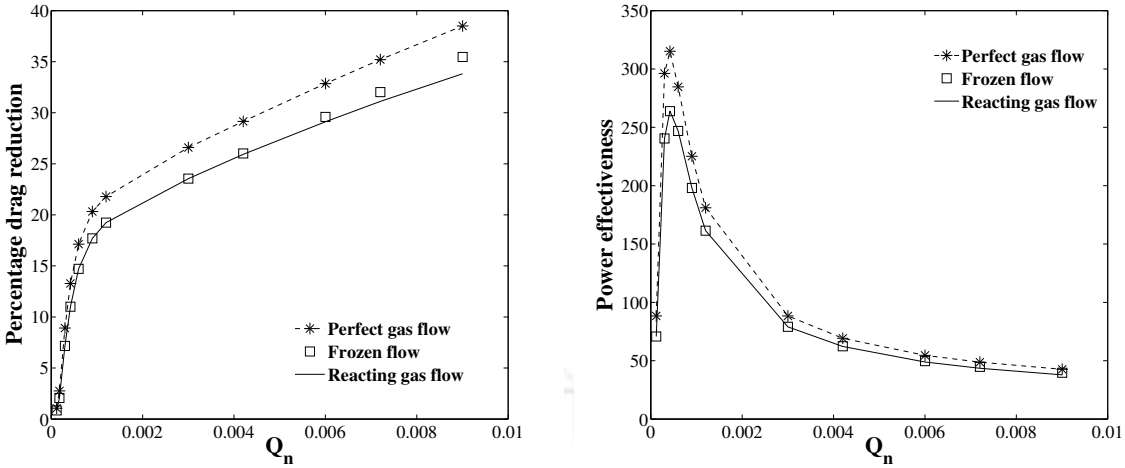

(a) Percentage drag reduction variation with strength of energy spot

(b) Change in power effectiveness with strength of energy spot

Figure 4.6: Effect of strength of energy spot for different flow models

due to temperature dependence of specific heats and possibility of chemical reactions reduce the peak power effectiveness by 16%. Therefore, temperature and specific heat variations of frozen and reacting flow models along the stagnation streamline are shown in Fig. 4.7(a) and Fig. 4.7(b) respectively. These figures help to evaluate the relative dominance of these two reasons related to real gas effects. No change in concentration of any species has been noticed along the stagnation streamline for reacting gas flow model since maximum temperature attained by the flow at the energy spot is lesser and insufficient to trigger any of the reactions modelled herein. Consequently, figures Fig. 4.7(a) and Fig. 4.7(b) show same magnitude and trend for frozen and reacting gas flow models for respective parameters. Match between specific heat values reveals that, concentration of all the species remain unaltered due to 7 W (Q_n= 4.2×10^{-4}) of energy addition. Hence endothermic reactions like dissociation are less dominant to introduce significant real gas effects. Therefore the change in specific heat seems to be predominant in reducing the power effectiveness for real gas flows in comparison with the perfect gas flow. Difference between the power effectiveness magnitudes of perfect and real gas flow models, inferred in Fig. 4.6(b), decreases with increase in strength of energy spot beyond the critical strength corresponding to maximum power effectiveness. Although dissociation of air is noticed in the region of energy deposition, for higher energy values, the corresponding gas mixture is found to recombine before approaching the sphere. Variation of oxygen (O_2) concentration along the stagnation streamline for different energy strengths shown in Fig. 4.8(a), justifies this fact. Thus the lower value of power effectiveness for reacting gas flow model, in comparison with the perfect gas flow model, is not governed by the chemical reactions. Change in specific heat is responsible

for the reduced power effectiveness (Fig. 4.8(b)), since it is same for frozen and reacting gas flow models for higher energy spot strengths as well.

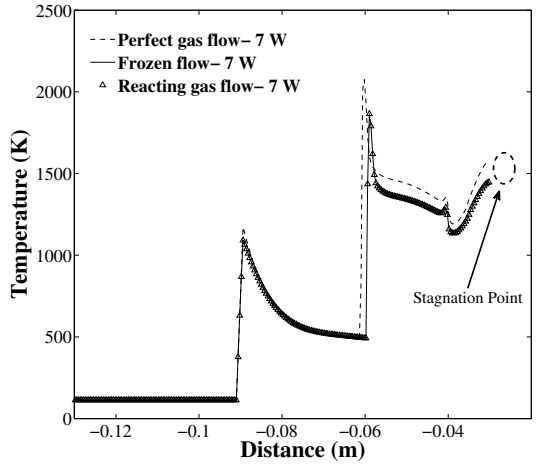

(a) Temperature variation for all gas flow models along the stagnation streamline for energy spot of 7 W strength

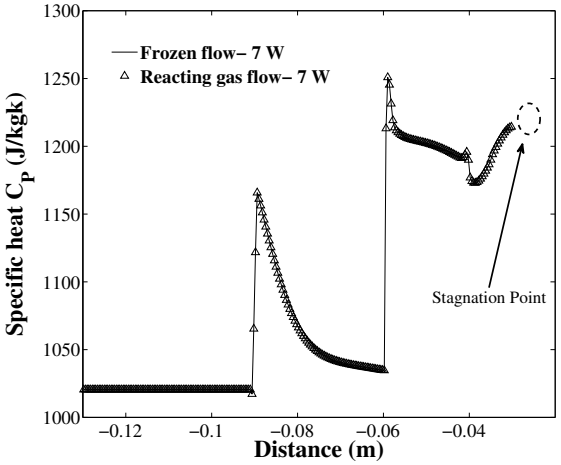

(b) Specific heat variation for frozen and reacting gas flow models along the stagnation streamline for energy spot of 7 W strength

Figure 4.7: Property variation along the stagnation streamline

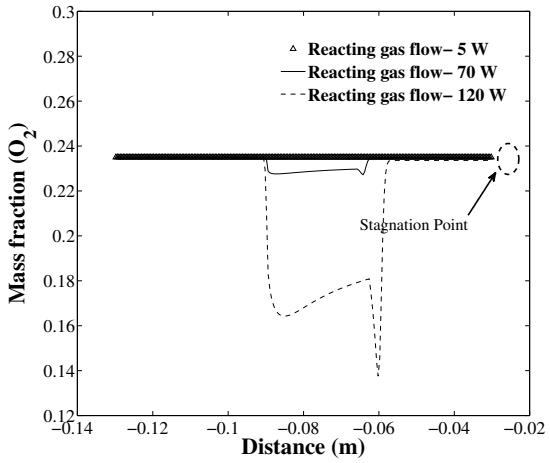

(a) Oxygen mass fraction along the stagnation streamline for various energy strengths

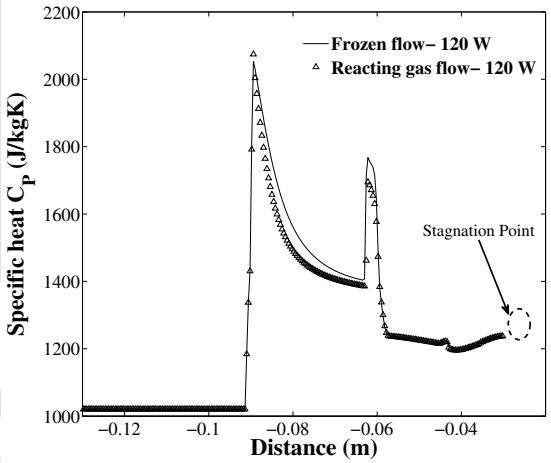

(b) Specific heat variation for frozen and reacting gas flow models along the stagnation streamline for energy spot of 120 W strength

Figure 4.8: Real gas effects with increase in energy strength

4.3.3 Effect of intensity of energy spot

Simulations are continued to study the effect of intensity of energy spot. Here, intensity is varied by changing the radius of energy spot for the same amount of energy (70 W, Q_n=

4.2×10^{-3}). The radius of spherical energy spot is varied between 2 to 14% of the sphere radius. Location of energy spot (L=2R=60 mm) is kept same as mentioned for earlier simulations. Variation of drag coefficient obtained from these simulations is shown in Fig. 4.9(a) and the corresponding power effectiveness in shown in Fig. 4.9(b). Increment in drag coefficient and thus reduction in power effectiveness can be seen from these two figures for all gas flow models with increase in radius of energy spot or decrease in energy density. Alteration in the shock structure and associated wall pressure distribution are the reasons of this lower performance. Wall pressure coefficient for different radii, shown in Fig. 4.10 for reacting flow, justifies this fact. As per this figure, upstream shift of shock hitting location and increment in peak pressure together increase the pressure drag with reduction in energy density. Here as well, perfect gas flow model shows relatively higher drag reduction for all cases and real gas effects lead to lower the effectiveness for this drag reduction technique for any hot spot radius.

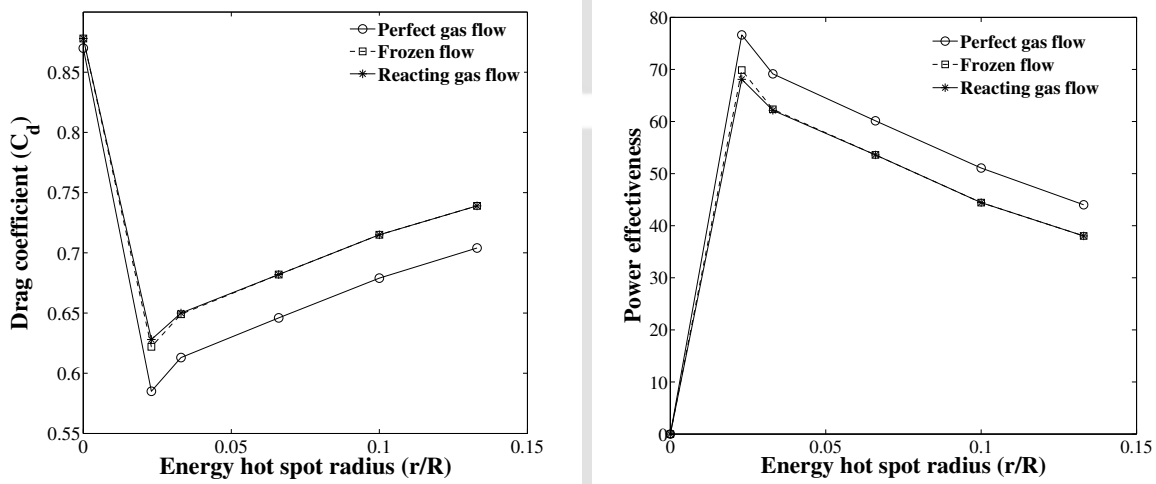

(a) Drag coefficient

(b) Power effectiveness

Figure 4.9: Variation of drag coefficient and power effectiveness with radius of energy spot

As per the Fig. 4.8(b) and Fig. 4.9, except for the highest energy density, frozen and reacting gas flow models have same percentage drag reduction and hence the power effectiveness. In order to inspect the effect of high energy densities, temperature variation along the stagnation streamline for two representative radii of hot spot are shown in Fig. 4.11(a) while the Fig. 4.11(b) shows the specific heat variation along the same line. It is evident from these plots that perfect gas flow model always shows more temperature rise due to energy addition in comparison to frozen and reacting flow, for any hot spot size. There exists limitation for temperature rise in case of real gas flow models due to increase in specific heat at energy deposition locations (Fig. 4.11(b)).

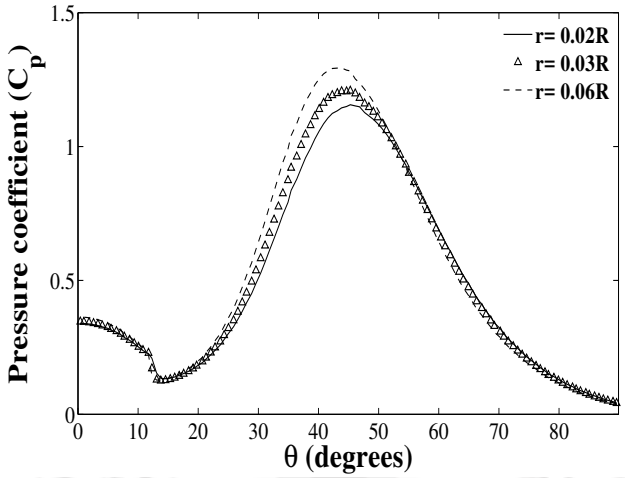

Figure 4.10: Surface pressure distribution for different energy spot radii (reacting flow)

Specific heat variation shows identical trend for frozen and reacting flow models for larger spot sizes, while, for smaller sizes, these gas flow models show different temperature rise. It implies that, the discrimination between reacting and frozen flow models is due to presence of chemical reactions at deposition location. Those dissociation reactions are then followed by recombination reactions in the region downstream of hot spot. Therefore the gap between the temperature profiles (Fig. 4.11(a)) of frozen and reacting model reduces in those regions. However, there remains certain difference in specific heat values close to the stagnation point due to prolonged recombination process. These effects alter the pressure on the surface in case of reacting flow model which in turn lead to different values of drag and power effectiveness than that of frozen flow model. Thus change in specific heats with temperature is prominent in degrading the performance at moderate intensities while the chemical reaction is partially responsible for high intensity energy deposition cases.

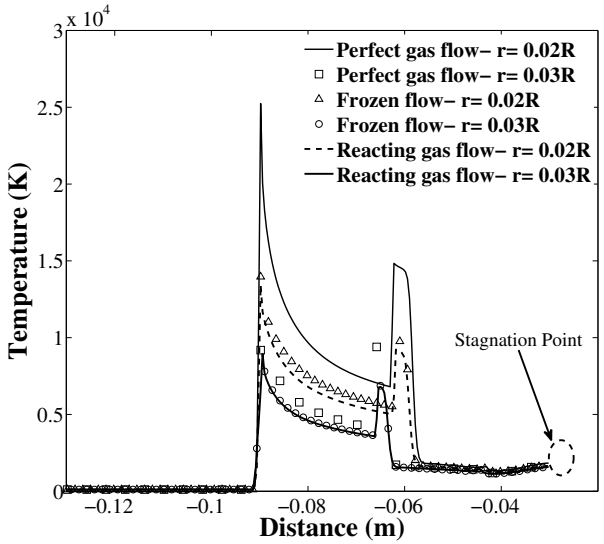

(a) Temperature variation for representative radii of energy deposition along the stagnation streamline

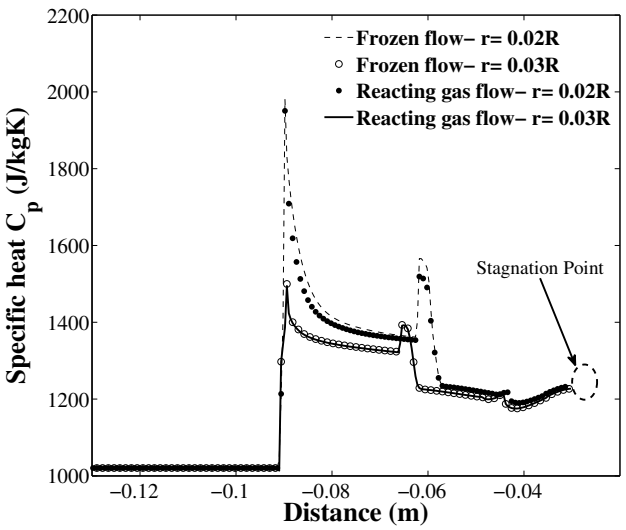

(b) Specific heat variation for representative radii of energy deposition along the stagnation streamline

Figure 4.11: Effect of intensity of energy spot

4.3.4 Effect of freestream stagnation enthalpy

Investigations are then carried out to study the real gas effects on the performance of energy deposition based drag reduction technique for different freestream stagnation enthalpies. In order to perform these simulations, freestream total enthalpy is varied from 1.26 to 10.50 MJ/kg by changing the freestream temperature from 113 K to 800 K. However, other freestream conditions like Mach number and pressure are kept same as in

earlier cases. Radius of the energy spot chosen here is 3% of sphere radius and location as 60 mm upstream of stagnation point. For these studies, absolute quantity of energy deposited has been varied from $0 - 120$ W for each stagnation enthalpy case. As an outcome of this, typical variation in power effectiveness for total enthalpy conditions of 1.26 MJ/kg and 5.92 MJ/kg for different energy strengths is shown in Fig. 4.12(a) and Fig. 4.12(b) respectively. As seen in the Fig. 4.12, both low and high enthalpy flows

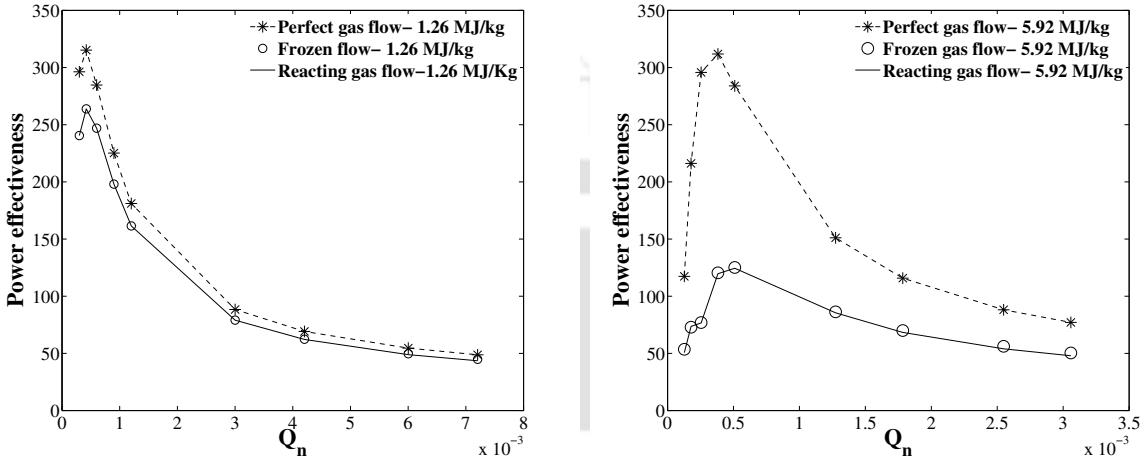

(a) Variation of power effectiveness for stagnation enthalpy of 1.26 MJ/kg

(b) Variation of power effectiveness for stagnation enthalpy of 5.92 MJ/kg

Figure 4.12: Variation of power effectiveness for different stagnation enthalpies

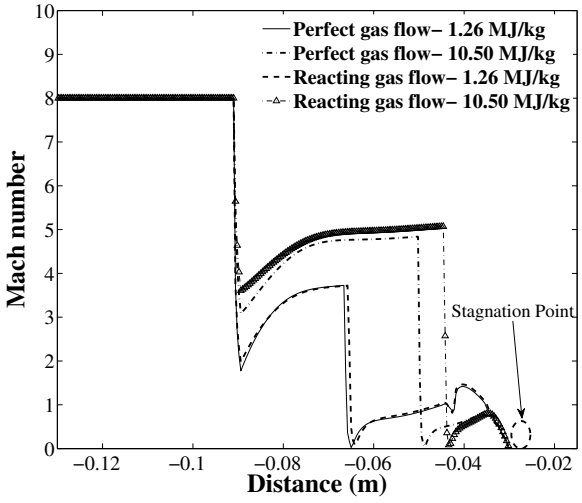

Figure 4.13: Mach number variation along the stagnation streamline

have similar trend for power effectiveness variation with change in the quantity of energy deposited upstream of the sphere. The incidental similarity is that the same amount of energy required for either gas flow models to achieve the maximum power effectiveness

for a given freestream enthalpy. Actually high enthalpy flows require higher absolute strength of energy spot to achieve same power effectiveness. As a result of this, critical absolute energy, associated with maximum power effectiveness, has to be increased with increase in freestream stagnation enthalpy for all the flow models. It is also evident from Fig. 4.12 that absolute energy deposited for maximum effectiveness is 7 W and 15 W for freestream enthalpies of 1.26 MJ/Kg and 5.92 MJ/Kg respectively. Moreover, maximum power effectiveness is different for both the cases. The reason for the different amount of absolute energies lies in the fact that, a disturbance created due to energy deposition loses its strength with increase in stagnation enthalpy of the flow. Therefore, Mach number downstream of the energy spot, or the approach Mach number for the sphere, remains higher as shown in Fig. 4.13. It leads to higher surface pressure and higher drag which necessarily demands higher absolute strength of energy to achieve better power effectiveness. Notable fact from the same figure is that peak power effectiveness would be attained in a narrow band of non-dimensional energy strength for two different stagnation enthalpies. This narrow band is found to be centered around non-dimensional energy of amount 4×10^{-4}. Another important point that is evident from Fig. 4.12 is the significant decrement in the peak power effectiveness for reacting gas flow model with increase in stagnation enthalpy. This is necessarily about the decrement in maximum power effectiveness for same relative strength of energy. Same fact is elaborately shown in Fig. 4.14 that depicts the variation in power effectiveness for 10 W of energy with various freestream total enthalpy conditions from the perspective of relative strength of energy. This figure demonstrates two distinct power effectiveness trends for two gas flow models. Power effectiveness shows monotonic decrement with increase in stagnation enthalpy when same amount of absolute energy is added in case of real gas model, while there is an inversion point for perfect gas flow model which corresponds to maximum power effectiveness for the chosen absolute strength of energy spot. This discrimination can be well understood by plotting different terms in Eq. 4.1 as shown in Fig. 4.15. Here magnitude of drag reduction and freestream velocity are chosen for plotting for various stagnation enthalpies since strength of energy spot is kept constant. Velocity difference between gas flow models is found to be negligible for all enthalpy conditions, so freestream velocity of perfect gas is only plotted in Fig. 4.15. As in Eq. 4.1, denominator is constant and among two terms in the numerator, amount of drag reduction decreases while velocity increases with increase in stagnation enthalpy for both the gas flow models. Therefore, numerator in Eq. 4.1, which corresponds to power saved, initially increases for perfect gas flow model albeit decrement in drag reduction. However, reacting gas flow model experiences lower drag reduction. Hence, decrement in drag reduction in Eq. 4.1 is an important parameter to justify the decrement in power effectiveness for real gas. Its physics can be

illustrated in more detail as shown in Fig. 4.16. As observed in Fig. 4.2, deposited energy in the hot spot creates a disturbance in the flow and changes the streamline pattern which results in wave drag reduction. Therefore the amount of drag reduced depends upon the intensity of the energy spot and hence the strength of disturbance getting created by the virtue of energy deposition. Strength of this disturbance can be quantified in terms of temperature rise at the hot spot location. Figure 4.16 asserts the fact that reduced strength of the disturbance leads to lower increment of temperature at higher stagnation enthalpy conditions for same amount of deposited energy. Thus, potential of given energy intensity decreases with increase in freestream stagnation enthalpy for both the gas flow models. However, perfect gas flow always bears higher efficacy than the real gas, since it has higher temperature rise for same strength of energy spot. In case of perfect gas flow, added energy gets better utilized for increasing the temperature. But for the real gas, temperature dependent specific heat and chemical reactions demand more amount of energy for same temperature rise. Thus, given energy intensity acts as a source of lower strength in real gas flow as compared to that in perfect gas flow.

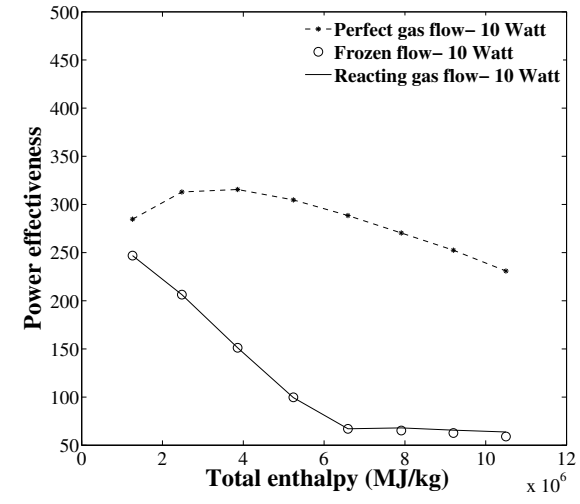

Figure 4.14: Change in power effectiveness for 10 W energy deposition case with change in freestream stagnation enthalpy

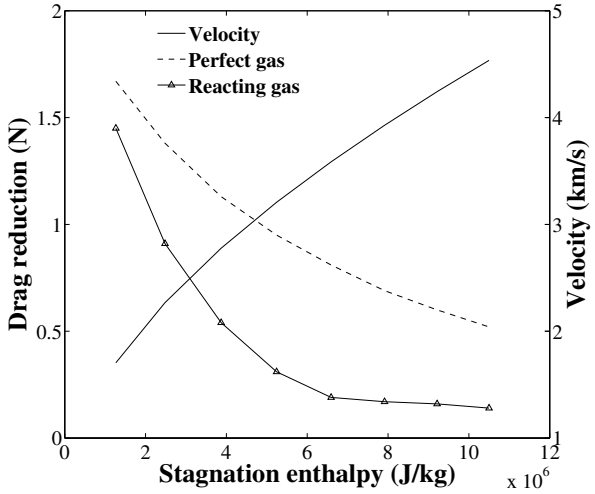

Figure 4.15: Variation of various parameters affecting the power effectiveness with increase in freestream enthalpy

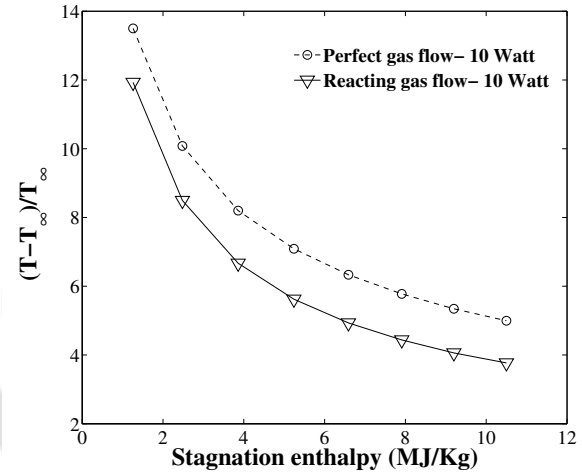

Figure 4.16: Change in non-dimensional temperature at hot spot location for 10 W energy deposition case with change in freestream stagnation enthalpy

4.4 Conclusions

A flow solver for high enthalpy axisymmetric flows has been successfully employed for the aerothermodynamic analysis of energy deposition based drag reduction technique. This active technique is investigated for its performance in reducing drag using perfect gas, frozen and reacting flow models. Critical energy strength corresponding to peak power effectiveness is found to be independent of gas flow models, but the non-dimensional energy is noted to be close for different stagnation enthalpies to attain peak power effectiveness.

Perfect gas flow model is seen to predict higher effectiveness at that critical energy deposition while the rise in specific heats value is found to degrade the performance as predicted by frozen and reacting flow models. Studies with various energy intensities showed that amount of drag reduction decreases with decrease in energy intensity for all gas flow models. Frozen and reacting flow models, which evaluate same performance at moderate energy intensities, have found to deviate in prediction at higher intensities due to presence of chemical reactions. It has been shown that there is significant degradation in peak power effectiveness at higher freestream enthalpies as a consequence of real gas effects. It has also been noticed that the deviation in performance of this technique for perfect gas flow and reacting flow increases with increase in freestream stagnation enthalpy. Thus, present studies clearly demonstrate the importance of real gas effects while evaluating the performance of energy deposition based drag reduction technique.

CHAPTER 5

UNDERSTANDING THE DYNAMICS OF COUNTER JET DRAG REDUCTION TECHNIQUE

Overview

This chapter centres around exploring the main governing number relating the dynamics of counter jet flow based drag reduction technique. Hence, initial numerical studies are performed to review the various literature reported influencing parameters for different steady jet flow conditions. After finding out the limitation of these parameters, a new non-dimensional number (jet to freestream momentum ratio) is suggested and examined by performing detailed theoretical as well as numerical studies at various jet and freestream conditions. These investigations portrayed that the same drag coefficient can be obtained by keeping the same jet to freestream momentum ratio (R_{mA}). It has also been noted that, suggested parameter dictates the intensity of sonic/low supersonic counter jet flowfield more fundamentally and holds good for the estimation of shock stand-off distance, Mach disk diameter, Mach disk location, free stagnation point location, drag coefficient etc. Thus, it is worth to consider the newly introduced momentum ratio as a governing parameter for the prediction of vital flow features of the steady counter jet flow based drag reduction technique.

5.1 Introduction

Higher aerodynamic heating is a fundamental issue of supersonic airborne flights. Further, rendering bluntness in the nose region is a conventional technique to alleviate wall heating for a hypersonic flight. But, it increases the drag force for high speed flights and hinders in managing the cost-efficient flight by increasing the fuel consumption and reducing the payload. Hence wave drag, which contributes to the major aerodynamic load, motivated various researchers to develop many active [59, 174] and passive [84, 175] techniques

for its mitigation. Among these, counter jet injection is regarded as one of the most convincing methods concerning both drag and heat reduction. Here, fluid jet emanates from the stagnation point of the blunt body. Further, it changes the effective body shape and envelops the body to diminish the drag along with the surface heat load. In view of this, extensive studies have been performed in this realm in an attempt to improve the overall performance and efficiency of high-speed vehicles.

Initially, Warren [64] reported the cooling effect of nitrogen and helium upstream injection in Mach 5.8 freestream. This experimental investigation showed that the cooling effect was more efficient for lower mass flow rate which did not affect the bow shock shape formed around the blunt body. Subsequently, Finley [65] presented an experimental and analytical study for blunt body counter jet injection. In this study, critical jet to freestream total pressure ratio was defined as a governing parameter to obtain a steady state flowfield. Later on, Fujita [176] extensively examined the unsteadiness involved with the opposing jet injection for an axisymmetric model. There are many other reports where attention was towards complexities related to turbulence [71, 72]. Further, Shang [86] executed both numerical and experimental investigations for injection of plasma in Mach 6 freestream. In this study, it was noticed that the viscous-inviscid interaction and thermal energy deposition plays an important role to reduce the drag force. Venukumar et al. [73] carried out experimental studies for 60^o apex angle blunt cone model. This investigation was performed in a steady state hypersonic flowfield of Mach number 8, where drag reduction up to 45% was reported with the variation of total pressure ratio. In the same year, Hayashi et al. [81] also analysed the effect of total pressure ratio on wall heat reduction in a supersonic condition. They found a remarkable heat flux decrement with the rise in total pressure ratio for a stable shock structure. Additionally, no relief in thermal load was observed for unsteady flowfield. Later on, the effect of freestream total enthalpy on drag reduction was demonstrated by Kulkarni et al. [74]. In that experimental study, more drag reduction for a fixed total pressure ratio at higher freestream total enthalpy was obtained. Sahoo et al. [177] documented the effectiveness of film cooling for three different injection gasses including air, helium and carbon dioxide for a large angle blunt cone flying at hypersonic Mach number. They observed helium was the most efficient injection gas among them. In this study, 30%–45% overall heat-transfer reduction was achieved at the cost of 12% increment in drag coefficient. For the first time, Yisheng [75] introduced a new parameter accounting flux along with total pressure ratio (R_{PA}) and correlated it with the intensity of the counter jet. It was noted that shock stand-off and drag coefficient remained same for a constant R_{PA}. However, in those studies, only jet exit conditions were altered to test this parameter. In one of the most recent work, Bibi et al. [79] carried out the numerical analysis for various nozzle

geometric configurations considering long as well as short penetration mode of counter jet injection. This report presented the effect of nozzle divergent angle and nozzle length on drag reduction. They noticed up to 56% of drag reduction in their study. In all these literatures, it was commonly observed that the aerodynamic performance of this technique is dependent on various parameters like mass flow rate, total pressure ratio, freestream total enthalpy, R_{PA}, nozzle geometry etc. However, these parameters are valid to characterise the drag and aerothermal load mitigation only under certain flow conditions with certain assumptions. These limitations, mandate the efforts to find out an explicit parameter which dictates flowfield and hence the overall aerodynamics in the presence of counter jet injection.

Thus, the present work aims at understanding the aerodynamics of wave drag reduction using counter jet against the supersonic flow past a blunt body. In this study, literature highlighted counter flow influencing parameters are investigated at different stable flowfield conditions. Further, their limitations in applicability are figured out at various situations. Therefore, a new non-dimensional number, governing the aerodynamics of secondary flow along with its physical interpretation, is proposed. Efforts are also extended to complement the introduced parameter in a CO_2 freestream and subsequently expand its validity. For this numerical study, the in-house developed solver has been used for simulations. Details of geometry and solvers settings are provided in the following sections.

5.2 Flow physics of counter jet injection

The present investigation is carried out to comprehend the dynamics of wave drag reduction using counter flow injection. In this active technique, a gaseous jet is injected opposing the supersonic/hypersonic mainstream from stagnation region of the blunt body. The resulting interaction between the jet and freestream leads to shock reframing which in turn alleviates the aerodynamic load markedly. The schematic of counter jet drag reduction technique is shown in Fig. 5.1. Here, the flowfield primarily depends upon the jet to freestream pitot pressure ratios (R_P=P_{0j}/P_{01}). For the case of $R_P > 1$, an underexpanded jet gets issued from the stagnation region and it provides a shield to the object against the mainstream. Consequently, a new appearance of obstruction, a fluid spike attached to the original blunt body, is sensed by the oncoming stream. The boundary of such a body is defined by interface formed between jet and mainstream. This structured obstruction pushes the bow shock away from the blunt body and rearranges the shock system. As a result, the high-pressure region also remains away from the object of interest and thus wave drag gets reduced. As explained by Finley [65] their is critical

pressure ratio below which injected jet has a multi-celled structure and it is unsteady in nature. But for $R_P > R_{P_{critical}}$, jet emanates radially outward with expansion waves originated at the jet exit location. They merge and form a barrel shock upon reflection from the jet boundary. In the axial direction, expansion gets terminated by a Mach disk. It is a normal shock which raises the pressure and decelerates the flow to subsonic level. After passing through the Mach disk, jet stream turns outward and back to form toroidal recirculation region. Then, the jet layer flows along the body surface and moves downstream. Shear layer gets formed on the jet boundary which entrains the fluid from the toroidal recirculation and fetches it to the reattachment point. In the steady state, jet comes to rest at free stagnation point where the pressure is pitot pressure. Thus, for pressure ratios above critical value, their is a single cell structure in the steady flowfield. Clearly, overall wave drag reduction is achieved by pushing away bow shock and creating low-pressure recirculation region.

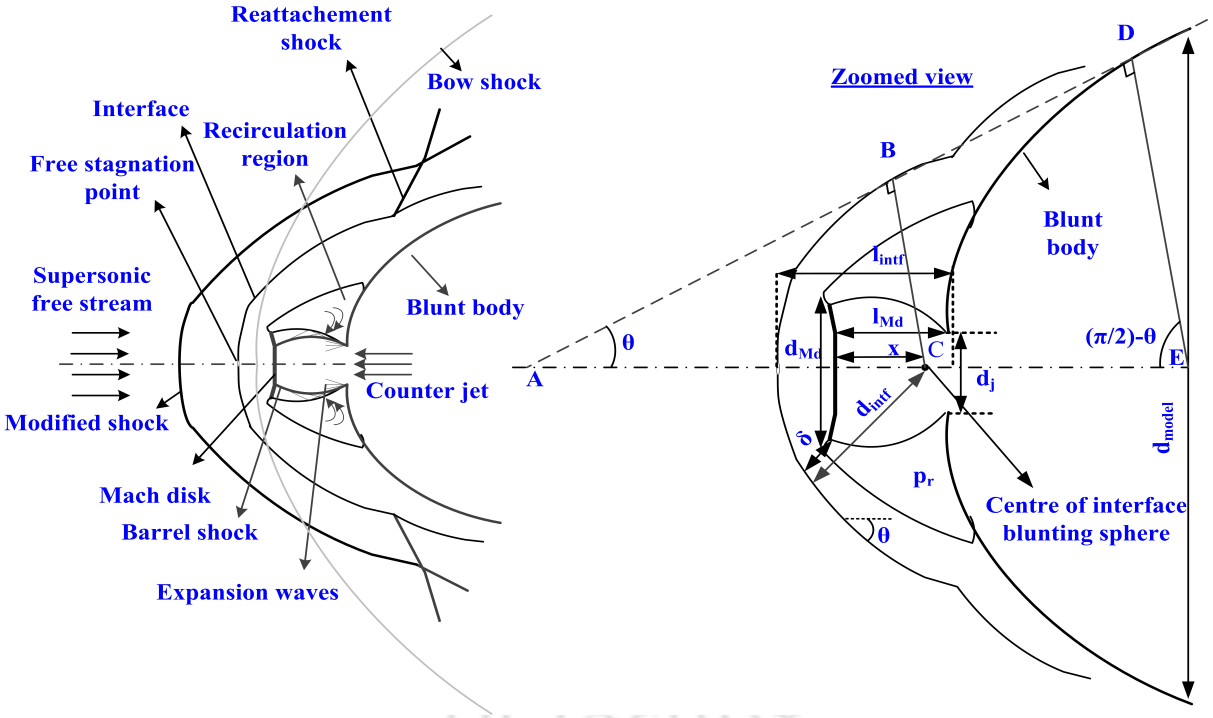

Figure 5.1: Schematic of counter jet drag reduction technique

5.3 Numerical validation

Numerical accuracy of the present solver is illustrated for the experimental case of opposing jet against a supersonic flow over a sphere of 0.0254 m radius. For this, freestream properties and jet exit conditions are listed in Table 5.1 and Table 5.2 respectively as

mentioned by Finley [65]. To simulate this case, a grid containing 200 by 200 quadrilateral cells is explored herein. In the computational domain, injection of secondary flow is provided by fixing the jet flow properties near the stagnation region. The surface pressure distribution obtained from this simulation is plotted and compared with existing experimental data in Fig. 5.2. This figure depicts an excellent match between them and verifies the present solver. Hence, present solver is suitable for further analysis of counter jet injection.

Table 5.1: Details of flow conditions for present investigations

M_∞	P_∞ (Pa)	T_∞ (K)	T_{wall} (K)	Y_{N_2}	Y_{O_2}
2.5	16141.34	130.86	300	0.765	0.235

Table 5.2: Details of jet exit condition for validation

P_{0j}/P_{02}	M_j	A	Gas
2.84	1.0	0.0173	air

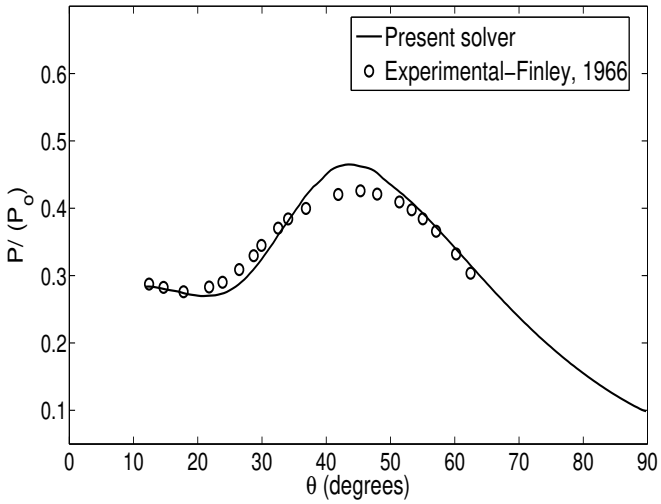

Figure 5.2: Comparison of experimental and numerical result

5.4 Analytical study

In this section, assessment of steady opposing jet based flowfield is carried out analytically to predict the various flow features. These features include distance of Mach disk from

the sphere, diameter of Mach disk, size of dead air region and pressure in the dead air region. For all these, firstly a new parameter, momentum ratio, is introduced and later its role is examined in controlling those critical parameters. Here momentum ratio is defined as:-

$$R_{mA} = \frac{\rho_j v_j^2 A_j}{\rho_\infty v_\infty^2 A_\infty} \tag{5.1}$$

where, ρ_j, v_j and A_j represent jet exit density, velocity and area respectively while ρ_∞ and v_∞ show freestream density and velocity, the model area is A_∞. In study, the interface formed between jet and the freestream is treated as a blunt spherical cone (Fig. 5.1). Therefore, modified Newtonian theory can be used over this interface to evaluate the recirculation region pressure which is as follows:-

$$\left(\frac{P_r}{P_{02}}\right) = sin^2\theta + \left(\frac{P_\infty}{P_{02}}\right).cos^2\theta \tag{5.2}$$

Here, θ is a local inclination angle of interface blunt cone over recirculation region. The recirculation pressure is shown by P_r, P_{02} is freestream pitot pressure and P_∞ represents freestream pressure.

Further, it is assumed that a common tangent passes through the interface blunt cone and the base model sphere at an angle θ from stagnation line as shown in Fig. 5.1. In this figure, a control surface marked with dashed line is considered which includes the interface. The momentum balance on this control surface provides the following equation:-

$$\frac{\pi}{8} d_{intf}^2 cos^4\theta (P_{02} - P_\infty) - \frac{\pi}{4} d_j^2 (P_j - P_r) = m_j v_j + m_l v_l cos\theta \tag{5.3}$$

Here, d_{intf} and d_j are interface and jet exit diameter respectively, P_j and m_j are jet pressure and mass flow rate at exit respectively, m_l and v_l are mass flow rate and velocity of jet leaving the control surface which is considered as surface bounded by interface. Here, various new functions are introduced

$$G = \frac{(pA + mv)}{m(C_p T_o)^{(1/2)}}; W = m(C_p T_o)^{(1/2)}; V = \frac{v}{m(C_p T_o)^{(1/2)}}; Z = \frac{1}{2} cos^4\theta \left(1 - \frac{P_\infty}{P_{02}}\right) \tag{5.4}$$

Putting these variables into Eqn. 5.3 and further rearrangement of it provides the expression for the interface blunt cone diameter in non-dimensional form:-

$$D_{intf}^2 = \frac{P_{oj}}{P_{o2}} I_j \left(1 + \frac{V_l cos\theta}{G_j}\right) Z^{-1} - \left(\frac{P_r}{P_{02}}\right) Z^{-1} \tag{5.5}$$

Here, $D_{intf} = \frac{d_{intf}}{d_m}$ while P_{oj} is the jet exit total pressure. The steady state counter jet expansion of the flow is terminated by a normal shock called Mach disk. The location

of the Mach disk is determined using expression as suggested by Thornhill and Thornhill [178]. However, this relation is valid only for M_j=1.0 (jet Mach number at exit) and γ_j=1.4 (specific heat ratio of jet).

$$L_{Md} = \frac{l_{Md}}{d_j} = 0.77 \frac{P_{oj}}{P_{02}}^{1/2} \tag{5.6}$$

Here, l_{Md} represents the Mach disk location from stagnation point while L_{Md} denotes non-dimensional Mach disk location. Further, diameter of the Mach disk can be evaluated using the equation given by Love [179] which is valid for M_j=1.0.

$$D_{Md}^2 = \left(\frac{d_{Md}}{d_j}\right)^2 = 0.3 + 0.325 \frac{P_{oj}}{P_{02}} . \left(\frac{P_r}{P_{02}}\right)^{-1} \tag{5.7}$$

where, d_{Md} shows the Mach disk diameter while D_{Md} is Mach disk diameter in non-dimensional form. Here, it is assumed that the jet passing through the Mach disk has uniform pressure P_{02} and it gets choked while passing through the annulus of thickness δ as shown in figure 5.1. As suggested by Love [180] it is assumed that flow through the annulas region would pass in the tangential direction to the the interface. If the mean diameter of annulas is taken d_{Md} then continuity equation for M_j=1 provides the following equation:-

$$\pi d_{Md} \delta P_{02} = \pi {d_j}^2 P_{oj} \tag{5.8}$$

$$\Delta = \frac{\delta}{d_j} = \frac{P_{oj}}{4 P_{02} D_{Md}} \tag{5.9}$$

Using Pythagoras's theorem for geometry shown in Fig. 5.1 the distance x is ($X = x/d_j$) is calculated as:-

$$4X^2 = \left(D_{intf} - 2\Delta\right)^2 - D_{Md}^2 \tag{5.10}$$

Thus, knowing all the distances, distance of interface formed between jet and the freestream from stagnation point along the stagnation streamline can be evaluated as:-

$$\frac{l_{intf}}{d_{model}} = \frac{l_{Md}}{d_{model}} + \frac{d_{intf}}{2 d_{model}} - \frac{x}{d_{model}} \tag{5.11}$$

Considering ΔABC and Δ ADE in geometry as shown in Fig. 5.1, we have,

$$\frac{d_{model}}{d_{intf}} = \frac{\frac{d_{intf}}{2sin\theta} + \frac{1}{2} d_{model} + l_{Md} - x}{\frac{d_{intf}}{2sin\theta}} \tag{5.12}$$

After rearrangement, we can get,

$$D = \frac{D_{intf} + 2sin\theta.(L_{Md} - X)}{1 - sin\theta} \tag{5.13}$$

Here, D is the ratio of d_{model} and d_j. This Eqn 5.13 can be iteratively solved for local inclination angle θ. Here, the right hand side of this equation is the geometrical relation but it can be calculated using fluid dynamics expressions as given in Eqn. 5.3, 5.5, 5.6, 5.7, 5.9 and 5.10. Further, for steady state physical situation, we know that, their is a unique value of θ for any combination of jet exit and freestream condition. Thus evaluated value of θ helps to locate the position of interface blunt cone and various flow aspects like free stagnation point, Mach disk diameter and locations. This methodology of prediction of flow parameters is considered for various jet exit and freestream conditions such that their momentum ratio remains constant. These parameters are calculated using this analytical method and plotted in Fig. 5.3 with freestream Mach number for various momentum ratios. It clearly depicts minor increment in the interface location and Mach disk diameter with the increment in freestream Mach number. Moreover, the variation of Mach disk location and recirculation region pressure coefficient vary in narrow range. Hence, this study hints that momentum ratio is a vital parameter to govern the counter jet aerodynamics. This observation is examined numerically in the following section.

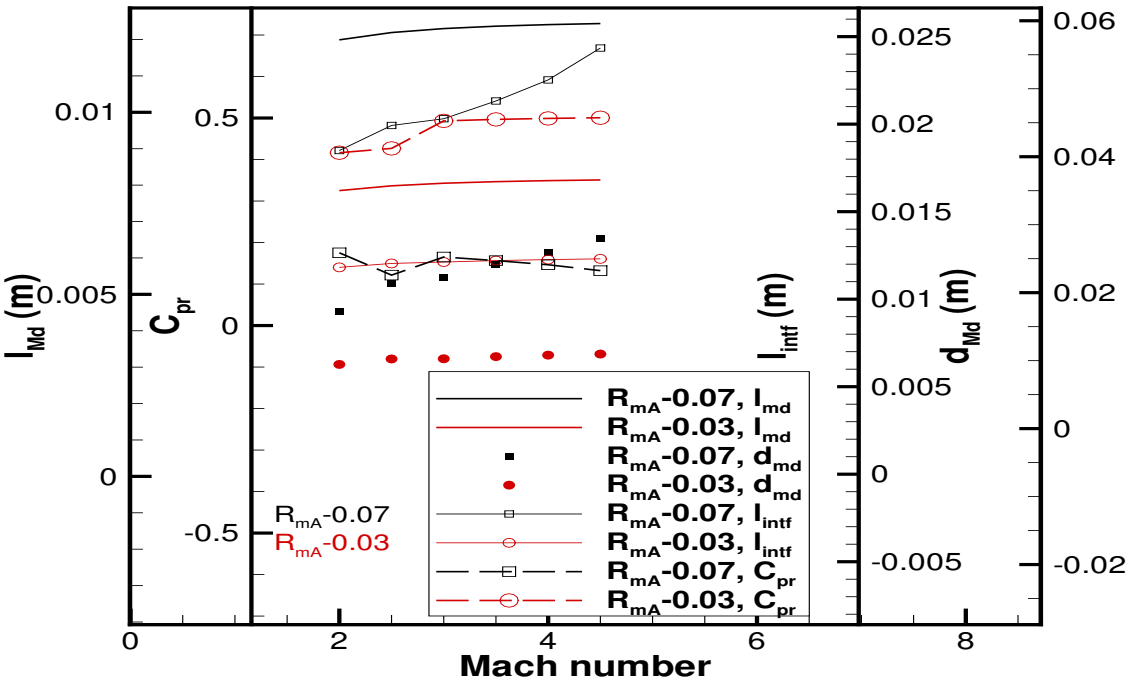

Figure 5.3: Variation of critical parameters with freestream Mach number for different R_{mA}

5.5 Results and discussions

This section deals with the computational studies which are performed to second the analytical results discussed in the earlier section. In this phase non-dimensional parameters other than momentum ratio are also assessed for their influence on the flowfield. Hence, various non-dimensional parameters are introduced. Simultaneously, their role on flowfield modification and wave drag reduction are also investigated. The parameters include, jet to freestream total pressure ratio (R_P), jet to body area ratio (A) and jet to freestream momentum ratio (R_{mA}). Among these, R_P is considered to be the most influential parameter as per earlier studies [73, 75]. With this thought, simulations are first planned to evaluate the dominance of total pressure ratio (R_P) for flow over a sphere (R-0.0254 m). Hence, two different R_P for the same freestream condition are considered in the initial set. The details of freestream and jet exit parameters are mentioned in Table 5.3 and Table 5.4 respectively. Throughout the study, the total temperature of opposing jet and freestream are kept same. The pressure contours obtained from these simulations are shown in Fig. 5.4(a). It is evident that all flow characteristics like bow shock, reattachment shock, Mach disk, recirculation region are captured very well. It can also be noted that high-pressure zone lies between the bow shock and Mach disk. Further, the increment in bow shock and Mach disk locations is obtained for the higher R_P case. For more insight, the surface pressure distribution over a sphere is plotted for both cases in Fig. 5.4(b). In general, it is observed that initially surface pressure shows minor decrement. After that, it starts to increase and attains peak due to reattachment. Beyond this, it again begins to reduce in the downstream region. Moreover, the higher overall surface pressure is noticed in case of low R_P compared to the high R_P case. The calculated angles from surface pressure distributions corresponding to minimum recirculation pressure and peak reattachment pressure are tabulated in Table 5.4. It demonstrates delayed appearance in both critical parameters in higher R_P case. In other words, it has a larger recirculation region with low pressure as compared to low R_P case. Hence, increment in R_P leads to increased shock stand-off, distant Mach disk location, large recirculation region, delayed reattachment and in turn the reduced drag force. Thus, these set of simulations support the fact that R_P is the governing parameter for the counter flow injection technique.

Table 5.3: Details of flow conditions for present investigations

M_∞	P_∞ (Pa)	T_∞ (K)	T_{wall} (K)	Y_{N_2}	Y_{O_2}
2.5	16141.34	130.86	300	0.765	0.235

Table 5.4: Details of investigated cases to examine the effect of R_P and their corresponding results

Case	R_P	M_j	A	Gas	$\theta_{p_{min}}$	$\theta_{p_{max}}$	C_d
1.1	2.6	1.0	0.01395	air	23.67^o	48.37^o	0.322
1.2	3.5	1.0	0.01395	air	26.76^o	51.07^o	0.243

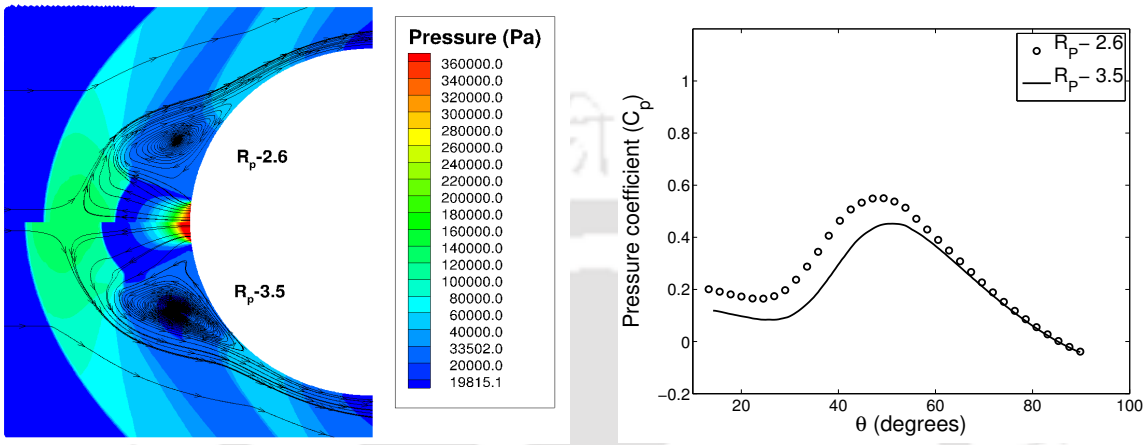

(a) Pressure contour (b) Surface pressure distribution

Figure 5.4: Effect of R_P on the shock structure and surface pressure distribution over sphere in different conditions

In the second set of numerical simulations, the R_P is kept constant, whereas the jet exit to body area ratio (A) is varied. Here, Table 5.5 shows the various jet parameters used in this study. The calculated drag coefficient, minimum and peak pressure angles from simulations are also mentioned in Table 5.5. Surprisingly, it portrays more effective opposing jet in case of higher area ratio despite the same R_P. To inspect this, pressure contours for both cases are shown in Fig. 5.5(a). Interestingly, dilated shock structure is seen in case of higher area ratio compared to lower area ratio. Thus, more recirculation, distant shock and Mach disk locations from stagnation point are obtained. Likewise, wider critical angles associated with the low and peak pressures along with low surface pressure are also apparent in Fig. 5.5(b). Consequently, lesser wave drag is achieved even for same R_P at higher area ratio. It implies that the wave drag reduction is not solely governed by jet to freestream total pressure ratio and jet exit to body area ratio.

Numerical simulations are continued to ascertain the combined effect of two different non-dimensional numbers, the total pressure ratio (R_P) and jet exit to body area ratio (A). Therefore, in this attempt a unified parameter R_{PA} ($R_P \times A$) is examined in different conditions. In order to do that the jet exit conditions like Mach number, total pressure, injection gas and jet exit area are varied while maintaining the same R_{PA} as detailed in Table 5.6. In these simulations, the synergistic interplay between the counter jet

Table 5.5: Details of investigated cases to examine the effect of A and their corresponding results

Case	R_P	M_j	A	Gas	$\theta_{p_{min}}$	$\theta_{p_{max}}$	C_d
2.1	3.5	1.0	0.00155	air	12.35^o	35.32^o	0.716
2.2	3.5	1.0	0.00620	air	21.37^o	45.23^o	0.447

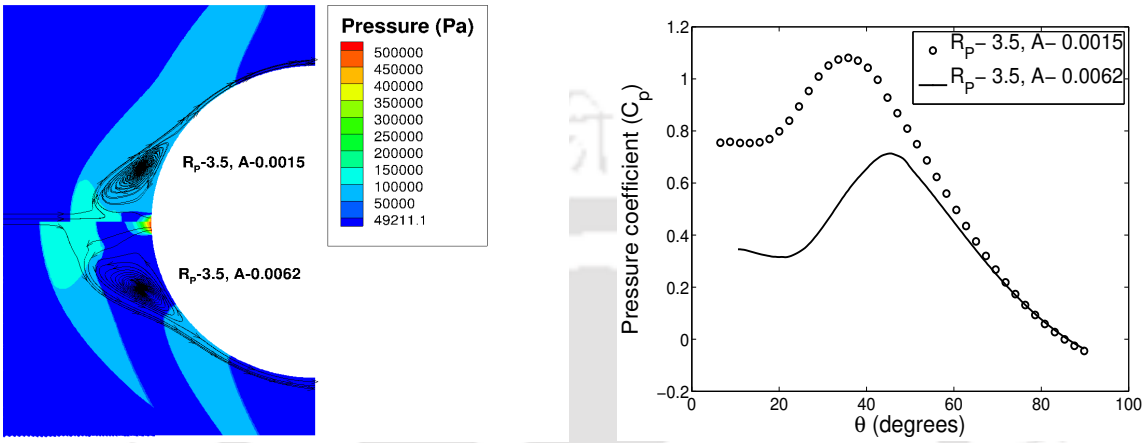

(a) Pressure contour

(b) Surface pressure distribution

Figure 5.5: Effect of the jet exit to body area ratio (A) on the shock structure and surface pressure distribution over sphere in different conditions

and mainstream leads to identical shock system for various opposing jet and freestream conditions. Similarly, angles corresponding to maximum surface pressure and minimum recirculation pressure are also positioned nearby. The same fact is enumerated using density gradients and surface pressure distribution for different conditions in Fig. 5.6(a) and Fig. 5.6(b). Since the overall aerodynamics is analogous, the same drag coefficient is achieved for various cases. A similar fact is evident in another simulation where helium replaces air as an injection gas. Further, simulations are conducted by changing the freestream Mach number to 4 while keeping the total pressure same as earlier. In this simulation, entirely different drag outcome is evident even for same R_{PA}. The shock structure and surface pressure distribution for this case is shown in Fig. 5.6(c) and Fig. 5.6(d) to confirms the same. The results of various simulations are given in Table 5.6. This study suggests that for a given freestream property, the said non-dimensional number (R_{PA}) uniquely alters the flowfield and results in same drag coefficient for same R_{PA} irrespective of jet exit conditions. But change in freestream conditions for same R_{PA} alters the flowfield largely. Hence, R_{PA} is not a unified governing parameter.

Table 5.6: Details of investigated cases to examine the effect of R_{PA} and their corresponding results

Case	R_{PA}	M_∞	R_P	M_j	A	Gas	$\theta_{p_{min}}$	$\theta_{p_{max}}$	Δ/R	C_d
3.1	0.0321	2.5	2.305	1.2	0.01395	air	23.18^o	47.03^o	0.76	0.358
3.2	0.0321	2.5	5.188	1.2	0.00620	air	23.18^o	47.94^o	0.78	0.353
3.3	0.030	2.5	2.215	1.2	0.01395	helium	21.82^o	44.45^o	0.81	0.342
3.4	0.0054	2.5	3.5	1.0	0.00155	air	12.35^o	35.32^o	0.50	0.716
3.5	0.0054	2.5	3.5	1.1	0.00155	air	12.41^o	35.31^o	0.50	0.715
3.6	0.0054	4.0	3.5	1.0	0.00155	air	19.58^o	41.69^o	0.60	0.484

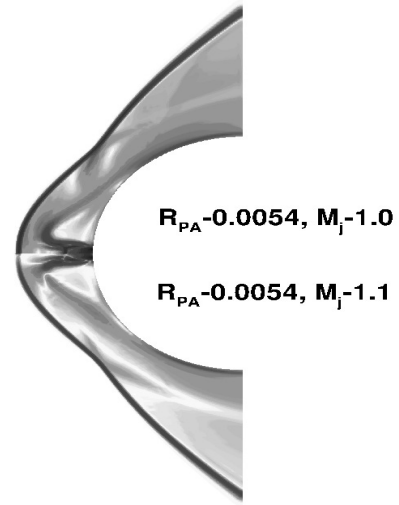

(a) Density gradient

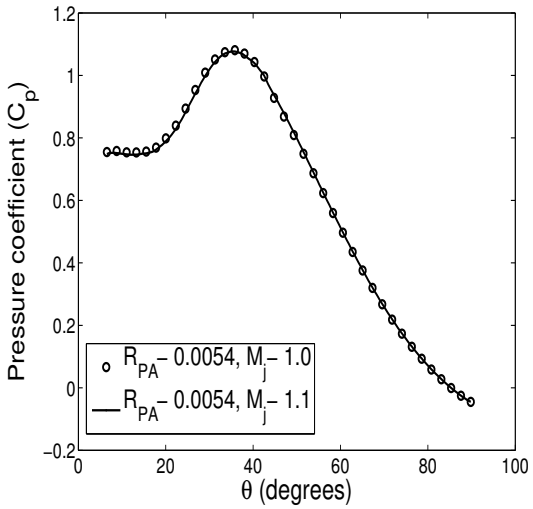

(b) Surface pressure distribution

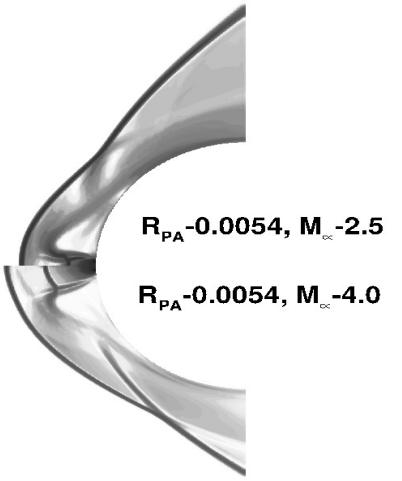

(c) Density gradient

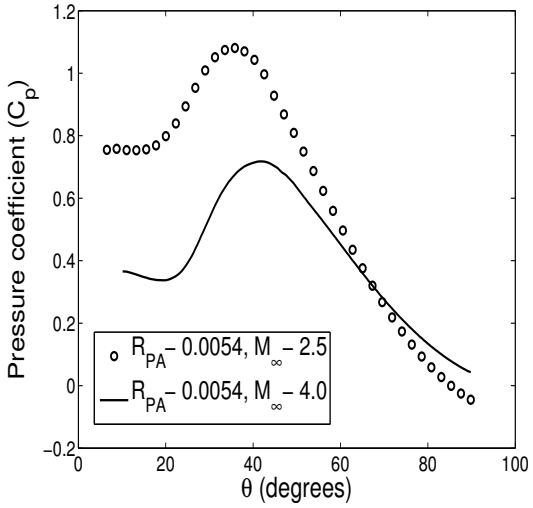

(d) Surface pressure distribution

Figure 5.6: Effect of R_{PA} on the shock structure and surface pressure distribution over sphere in different conditions

Further, the new non-dimensional number is introduced in an attempt to find out the universal governing parameter for opposing jet flowfield. The proposed number is defined by the ratio of jet outgoing momentum to the freestream incoming momentum ($R_{mA}=\frac{\rho_{jet}{V_{jet}}^2 A_{jet}}{\rho_\infty {V_\infty}^2 A_{body}}$). In present studies, many values of R_{mA} are considered by similarly varying different conditions as discussed earlier. The result obtained from these simulations show that drag coefficient inversely varies with the R_{mA}. Here, the increased R_{mA} intensifies the opposing jet by increasing its momentum. Therefore, the jet flow with higher momentum keeps the oncoming supersonic flow to much upstream from the blunt body. This upstream movement of jet augments the length of fluid spike ahead of the blunt body as depicted in Fig. 5.7(a). Consequently, the shock relocates away from stagnation point according to augmented spike body. Further, the size of toroidal recirculation region increases which is attributed to shock recasting. Hence, it reduces the overall surface pressure distribution over the sphere as shown in Fig. 5.7(b). Therefore, the lower drag force is noticed with the increment of R_{mA}. Moreover, in a case of same R_{mA}, the momentum provided to jets are same as those of freestream. This results in an equivalent length of attached fluid spike, hence, shock structure remains identical. As a result, drag coefficient also remains same in these cases. Further, the same drag coefficient is also noticed in different freestream Mach number cases for same R_{mA}. Here, at the high freestream Mach number condition, the incoming momentum is greater. Hence, for constant R_{mA}, opposing jet of higher absolute momentum is required as compared to low Mach number case. However, the base or reference drag coefficient is more in higher freestream Mach number condition. Therefore, the same drag coefficient is obtained at the expense of the greater momentum of opposing jet. In other words, higher base drag is modulated by drawing out opposing fluid of higher momentum as compared to low M_∞ case so as to maintain same drag coefficient after injection in both the cases. Subsequent shock reframing leads to major flow aspects like recirculation area, flow reattachment angle, surface pressure distribution to be in close agreement as seen in Fig. 5.7(c) and Fig. 5.7(d). Hence, it can be concluded that the R_{mA} is a vital deciding non-dimensional number to estimate the drag coefficient for a given condition. To further justify this observation, simulations are continued for counter jet cases with CO_2 freestream*. The flow properties and corresponding simulated results for various jet exit conditions are provided in Table 5.7 and Table 5.8 respectively. Here, Table 5.8 shows a narrow range of drag coefficient values for same R_{mA}. Additionally, encouraging match between the surface pressure distribution for various cases are apparent in Fig. 5.8. These findings are common to earlier observation. Furthermore, relative percentage error

*In-house developed solver for CO_2 case has chemical kinetics as given by Maciel and Pimenta [181], however rest of the formulation is similar to that of air case and discussed in chapter 2.

is estimated for the numerically obtained drag coefficient in all the cases. It is calculated as $\%Err=\frac{Cd_i-C_{d_{avg.}}}{C_{d_{avg.}}}$ where, $C_{d_{avg.}}=\sum_{i=1}^{N} Cd_i/N$. The largest estimated error is 5.89 and 6.54 for air and CO_2 as a freestream respectively. It summarises that the momentum ratio is a more fundamental governing non-dimensional number and universally dictates the aerodynamics of opposing jet in the presence of a supersonic stream.

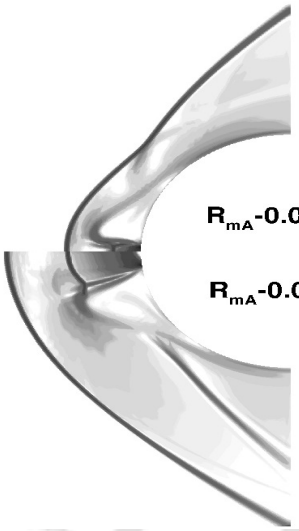

(a) Density gradient

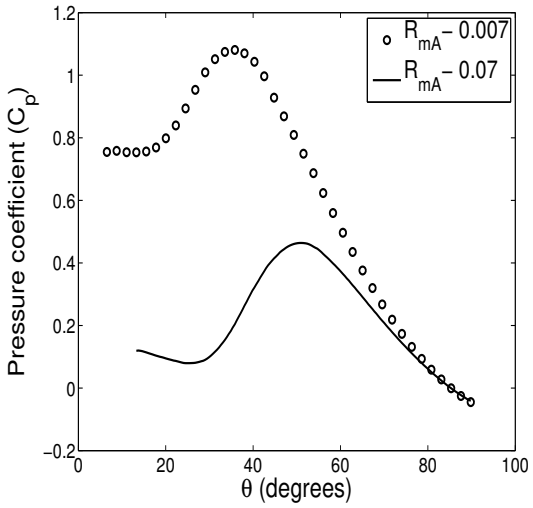

(b) Surface pressure distribution

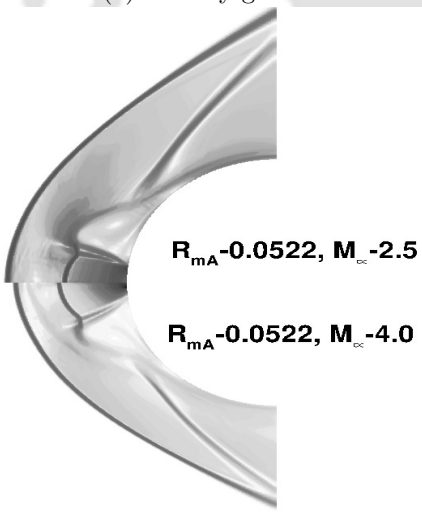

(c) Density gradient

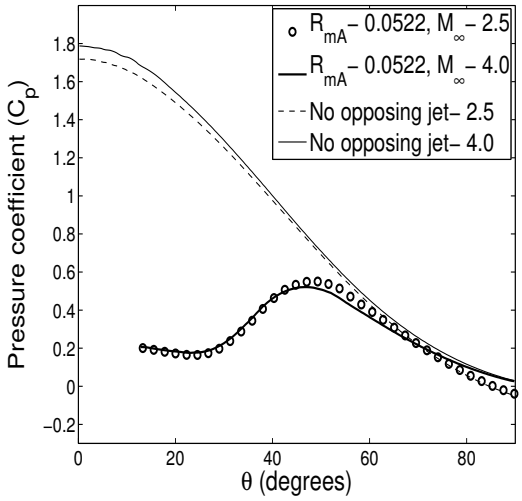

(d) Surface pressure distribution

Figure 5.7: Effect of R_{mA} on the shock structure and surface pressure distribution over sphere in different conditions

Table 5.7: Details of flow conditions for present investigations

M_∞	P_∞ (Pa)	T_∞ (K)	*Wall condition*	Y_{CO_2}
2.5	16141.34	130.86	adiabatic	1

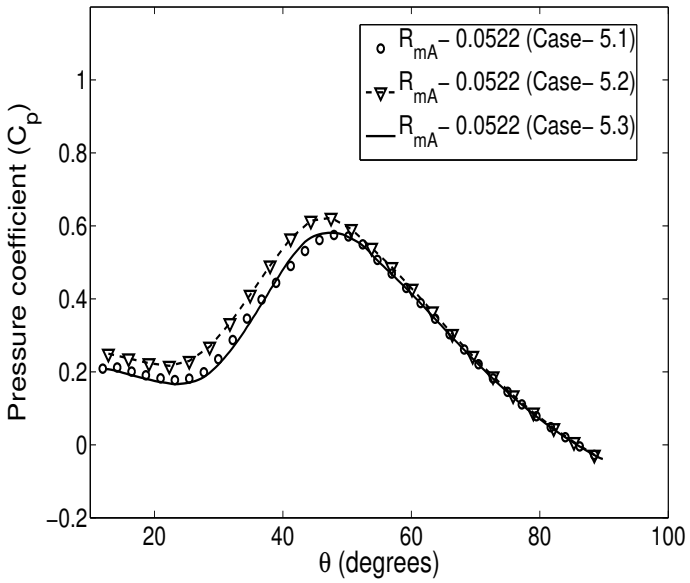

Figure 5.8: Effect of R_{mA} on the surface pressure distribution over sphere in different counter jet conditions in CO_2 freestream

Table 5.8: Details of investigated cases to examine the effect of R_{mA} and their corresponding results

Case	R_{mA}	M_∞	R_P	M_j	A	Gas	$\theta_{p_{min}}$	$\theta_{p_{max}}$	Δ/R	C_d	$\%Err$
I. *Freestream gas- Air (N_2+O_2)*											
4.1	0.0078	2.5	3.5	1.0	0.00155	air	12.35^o	35.32^o	0.5	0.716	0.09
4.2	0.0084	2.5	3.5	1.1	0.00155	air	12.41^o	35.31^o	0.5	0.715	0.09
4.3	0.0100	2.5	4.5	1.0	0.00155	air	14.61^o	36.67^o	0.51	0.686	-
4.4	0.0272	4.0	3.5	1.0	0.00155	air	19.58^o	41.69^o	0.605	0.484	-
4.5	0.0313	2.5	3.5	1.0	0.0062	air	21.37^o	45.23^o	0.68	0.447	1.67
4.6	0.0336	2.5	3.5	1.1	0.0062	air	20.95^o	44.35^o	0.68	0.45	2.56
4.7	0.0344	2.5	3.5	1.0	0.0062	helium	20^o	42.96^o	0.74	0.413	5.89
4.8	0.0348	2.5	3.45	1.2	0.0062	air	20.95^o	43.89^o	0.67	0.456	3.73
4.9	0.0362	2.5	3.323	1.2	0.0062	helium	19.58^o	42.95^o	0.73	0.430	2.07
4.10	0.0543	2.5	2.215	1.2	0.01395	helium	21.82^o	44.45^o	0.815	0.342	0.32
4.11	0.0522	2.5	2.305	1.2	0.01395	air	23.18^o	47.03^o	0.767	0.358	5.02
4.12	0.0522	4.0	5.188	1.2	0.0062	air	23.18^o	47.94^o	0.786	0.353	3.68
4.13	0.0522	2.5	2.59	1.0	0.01395	air	23.67^o	48.37^o	0.803	0.322	5.42
4.14	0.0522	4.0	6.72	1.0	0.00155	air	23.03^o	46.56^o	0.751	0.329	3.60
4.15	0.07	2.5	3.5	1.0	0.01395	air	26.76^o	51.07^o	0.90	0.243	0.67
4.16	0.07	2.5	3.5	1.1	0.01395	air	26.08^o	51.48^o	0.90	0.243	0.97
4.17	0.07	2.5	3.5	1.0	0.01395	helium	25.43^o	47.94^o	0.98	0.230	4.70
4.18	0.07	2.5	3.5	1.2	0.01395	air	25.33^o	51.05^o	0.9	0.248	3.05
II. *Freestream gas- Carbon di-oxide (CO_2)*											
5.1	0.0522	2.5	2.535	1.0	0.01395	CO_2	22.31^o	48.40^o	0.77	0.337	3.41
5.2	0.0522	2.5	2.250	1.2	0.01395	CO_2	21.82^o	47.07^o	0.73	0.372	6.54
5.3	0.0522	2.5	5.703	1.0	0.0062	CO_2	23.18^o	47.5^o	0.78	0.339	3.09

5.6 Conclusions

The numerical study has been successfully performed to find out the governing parameter of the counter jet based drag reduction technique. Initially, various aerodynamic influencing parameters are examined at the different steady-state conditions. Present investigations revealed their constraints in pre-estimation of vital details like shock stand-off distance, Mach disk diameter, Mach disk location, free stagnation point location, drag coefficient etc. In view of this, a newly introduced non-dimensional number (jet to freestream momentum ratio) is also analyzed at different conditions by performing theoretical as well as numerical studies. It is observed that the same value of jet to freestream momentum ratio yields same drag coefficient along with analogous shock structure. Further, simulations performed for CO_2 freestream conditions also led to similar conclusions. Apart from these, it has been marked that the largest relative error for obtained different drag coefficients at a fixed value of R_{mA} is only 5.89 % and 6.54 % for air and CO_2 freestream cases respectively. Thus, rigorous investigations clearly indicate that the importance of the jet to freestream momentum ratio. Therefore it must be considered to predict the characteristic flow features of the counter jet based drag reduction technique.

CHAPTER 6

SEPARATION MITIGATION USING PRESSURE FEEDBACK TECHNIQUE FOR HYPERSONIC SHOCK WAVE BOUNDARY LAYER INTERACTION

Overview

This chapter deals with the use of pressure feedback technique (PFT) as a separation control technique for ramp induced flow separation at hypersonic speed. Numerical simulations portrayed that though PFT can reduce the flow separation; further cooling of the feedback channel enhances its potential for separation control. Marginal cooling of channel walls to 175 K has reduced separation bubble size by 18.18 % while strong cooling of those walls to 50 K reduced the separation by 30 %. Such low enthalpy perfect gas flow simulations also showed the lower effectiveness of PFT with increased ramp angle. Further, it has been noticed from the perfect and reacting gas flow simulations that the cooling of pressure feedback channel introduces differential separation size for the same wall to total temperature ratio cases. Integration of cooled pressure feedback channel with blunt leading edge configuration showed reduced separation size for any bluntness radius. Effectiveness of this integration is seen in lowering the values of inversion and equivalent radii. Thus, use of cooled PFT in conjunction with leading edge bluntness is not only seen to have lower the intensity of shock wave boundary layer interaction (SWBLI) but also has enhanced the controllability of blunted leading edge without altering the entropy layer boundary layer interaction.

Desai, S., Kulkarni, V., Gadgil, H., 2018, "Separation mitigation using pressure feedback technique for hypersonic shock wave boundary layer interaction", ***The Proceedings of the Institution of Mechanical Engineers, Part G: Journal of Aerospace Engineering***, *(Online First)*.

6.1 Introduction

Shock wave boundary layer interaction (SWBLI) is a widely researched canonical problem in the field of supersonic/hypersonic aerodynamics. Presence of mazy shock patterns in this flow regime alter the flow behaviour and hence offer numerous challenges for investigation. Such interaction between the shock wave and boundary layer inevitably happens in many regions of the high speed vehicle like air breathing engine's intake, wing-body junction, afterbody tail, nozzle, deflected control surface and also in helicopter blades, missile components etc. Thus, rigorous investigation of flow complexities resulted by the SWBLI is highly essential before designing interaction prone systems or sub-systems or for improving the performance of existing design. In early days, active techniques like suction and injection were considered only for subsonic flows. But, further studies in supersonic flow regime have shown the possibility of its implementation for separation control. In line with this, Ball [182] concluded that size of the separation bubble can be diminished significantly by removing a small amount of dead air in case of compression corner. Similarly, mass transfer effect on the incoming boundary layer Mach number profile was also reported by Inger and Zee [137]. Later on, various control techniques have been reviewed by Delery [183]. McCormick [184] worked on reduction in the strength of lambda shock interaction. Faulker [140] used the ventilated wing surface, having common plenum under the region of shock formation, to reduce the wave drag. Recently, the use of such pressure feedback technique (PFT) was shown to prevent the separation in case of impinging shock and turbulent boundary layer interaction [139]. In this study, the suction location was varied around the separation region to reduce the turbulence effect. Another passive control technique of blunt leading edge has also been reported in the various literatures. Townsend [129] noted a decrement in separation bubble size for two dimensional geometry whereas Gray [185] found opposite behaviour with blunt axisymmetric models. Later on, Holden [186] experimentally concluded that small bluntness increases the separation while large values of bluntness reduce the extent of separation. Recently, John and Kulkarni [4] numerically showed that separation region widens with an increase in bluntness whereas it starts to reduce after attaining the maxima for both two dimensional and axisymmetric configurations [4, 134].

It is evident from the literature that PFT, which is a combination of injection and suction, bears the potential of separation control for appropriate feedback arrangement. But, it can be noticed from the literature that there is limited attention to assess PFT for ramp induced SWBLI (R-SWBLI). Therefore, it is highly desirable to study the effect of PFT on different states of R-SWBLI. Special characteristic features of R-SWBLI include increment in its strength with an increment in ramp angle and dependence of separation bubble size upon the wall temperature to freestream total temperature ratio. Therefore,

it is essential to examine the alteration in these characteristic features of R-SWBLI in the presence of PFT. The chapter is further focused on R-SWBLI in the presence of leading edge bluntness and PFT. A major reason for this exploration lies in the fact that leading edge bluntness based passive control technique does not guarantee separation control for smaller radii. But, it is possible to achieve the larger reduction in separation size with higher leading edge bluntness. Thus it is evident that, though PFT assures separation control, it has limitation on the amount of separation size decrement. On the other hand, blunt leading edge configurations help in separation control if the leading edge bluntness is more than certain critical value. These shortcomings of both the techniques provide an impetus to investigate the effect of their simultaneous use. A possibility of the reduction in minimum radius required for separation control will be explored through this integration. Hence, the present chapter is focused on the isolated effect of PFT in different conditions and the combined effect of leading edge bluntness and PFT for R-SWBLI.

6.2 Validation of in-house solvers

Prior to detailed investigations, validation of viscous version of the perfect and reacting flow solvers are performed for R-SWBLI case. Here, the choice of geometry of the test model is the 50 mm long flat plate attached with a ramp of 15^o angle as considered by Marini [187]. Freestream conditions used by Marini [187] as mentioned in the Table 6.1 are employed in the present case. These flow conditions are specified in the inlet of the domain while the outlet is considered to be supersonic. No-slip boundary condition is ensured at the wall. In perfect and reacting gas cases, inviscid fluxes are computed using second order AUSM scheme while viscous flux computations are carried out as mentioned in chapter 2. Results obtained from both the solvers are compared for the freestream conditions specified in Table 6.1. Thus, obtained wall pressure (C_p) and skin friction coefficient(C_f) variations are shown in Fig. 6.1(a) and Fig. 6.1(b). It can be noticed here that, for a given geometry and freestream conditions, all fundamental features of SWBLI like upstream influence, plateau pressure and separation bubble size are correctly captured using both the solvers. In this case, the temperature rise is up to 782 K which is insufficient to trigger chemical reactions as well as the significant change in specific heats value. Hence, both perfect gas and reacting gas solvers show similar wall property profiles. Thus, these figures not only provide the verification of the solvers but also confirm their accuracy in comparison with the experimental measurements which have 5-7 % uncertainty [187]. Both the solvers are then used to achieve present objectives. The computational domain is meshed judiciously for all the simulations to ensure better

capturing of vital flow features like leading edge shock, upstream influence, separation bubble size, boundary layer thickness etc. The final choice of mesh in each case which provides the mesh independent results is comprised of quadrilateral cells with their clustering near different sensitive regions. Details of typical mesh independence studies are given in next section.

Table 6.1: Details of freestream conditions and various leading edge radii for present simulations

Mach number	Pressure (Pa)	T_∞ (K)	T_{wall} (K)	Re (m^{-1})	Leading edge radii (mm)
6	199.4345	131.7	300	8×10^5	0.0, 0.3, 0.5, 1.0

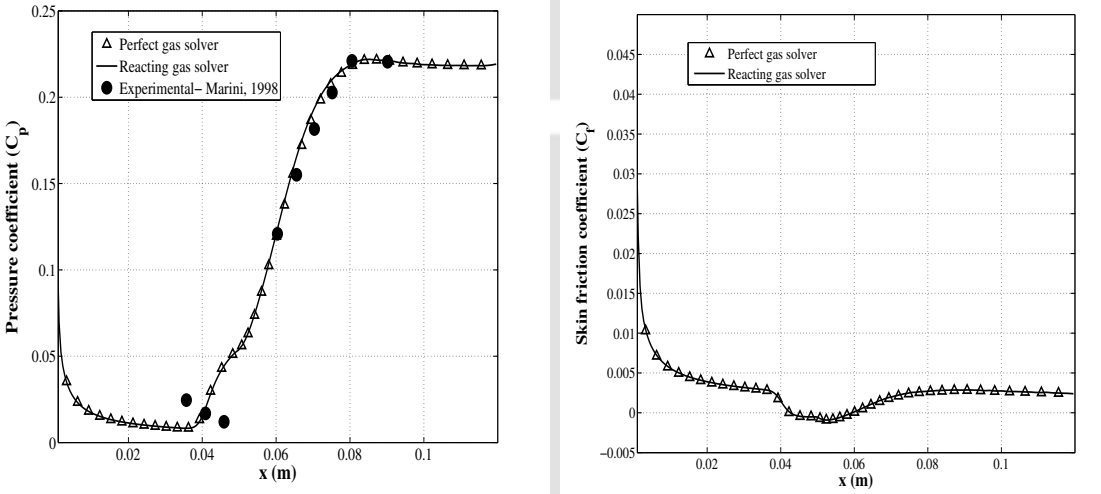

(a) Wall pressure coefficient distribution (b) Wall skin friction coefficient distribution

Figure 6.1: Validation of reacting gas solver

6.3 Grid independent study

This section deals with the grid refinement study for R-SWBLI case with sharp and blunt leading edge provided on the present baseline ramp geometry discussed in earlier section. Therefore, various grid configurations comprised of quadrilateral cells are accounted herein as detailed in Table 6.2. The freestream parameters mentioned in Table 6.1 are considered to assess these grids. The heat flux and pressure coefficient distributions obtained from simulations are plotted in Fig. 6.2 and Fig. 6.3 for both types of leading edge cases. Further, separation bubble size obtained for various simulations using

different grids are mentioned in Table 6.2. It is evident that no significant modification in the distribution of wall properties and separation bubble size are obtained with the grid finer than 260×120 and 415×120 for sharp and blunt configurations respectively. Such mesh independence studies are performed to arrive at the best choice of mesh for all the necessary simulations to achieve present objectives.

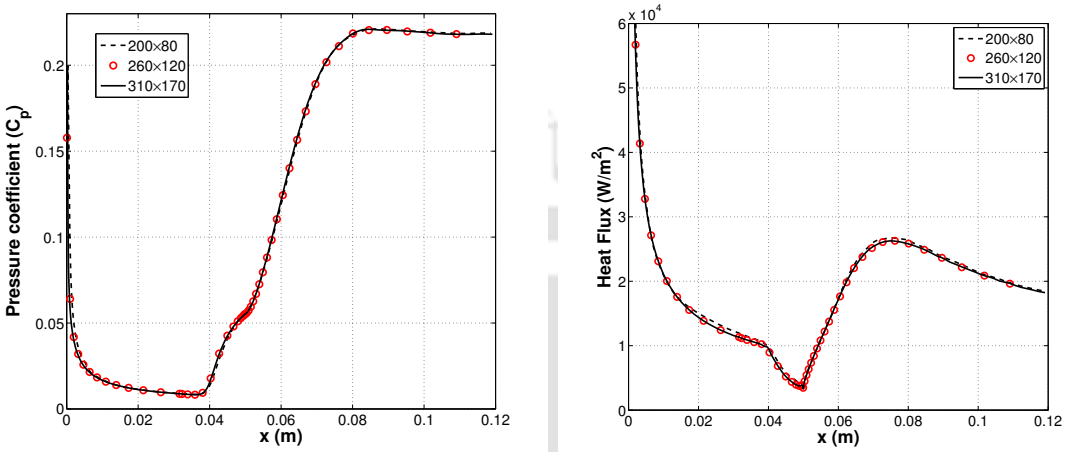

(a) Wall pressure coefficient distribution (sharp)

(b) Wall heat flux distribution (sharp)

Figure 6.2: Grid independent study for sharp leading edge configuration provided on a ramp model

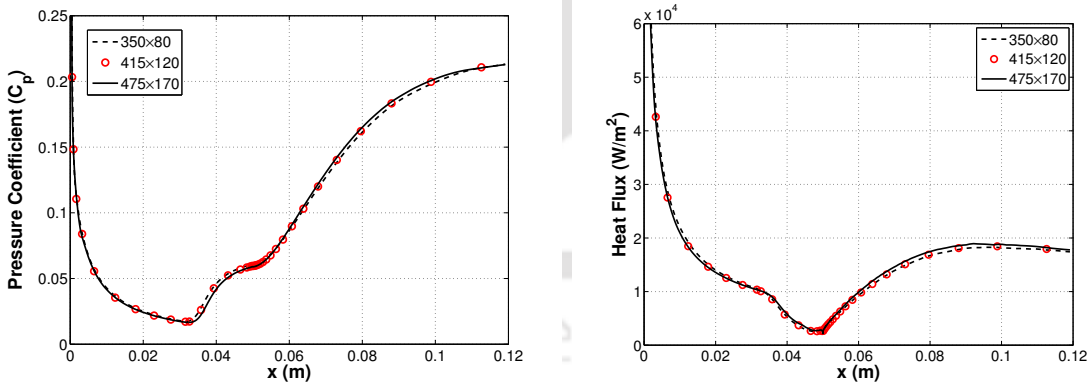

(a) Wall pressure coefficient distribution (R-0.5mm)

(b) Wall heat flux distribution (R-0.5mm)

Figure 6.3: Grid independent study for blunt leading edge configuration provided on a ramp model

Table 6.2: Details of grid independent study

Case	Grid size	Separation bubble size (mm)
Sharp leading edge	200×80	16.2
	260×120	17.6
	310×170	17.5
Blunt leading edge (0.5 mm)	350×80	30.9
	415×120	30.6
	475×170	29

6.4 Results and discussions

6.4.1 Studies with pressure feedback separation control system

Baseline simulation for the configuration and freestream conditions of Marini [187] is carried out to acquire the reference SWBLI interaction parameters using perfect gas solver. Therefore, a body-fitted mesh (260×120) comprised of quadrilateral cells is used for the same. It has been noted that the separation bubble is 17.6 mm wide, plateau pressure is 394 Pa, peak heat flux is 26.2 KW/m^2 and extent of upstream influence is 14.0 mm upstream of the ramp foot. On account of this information, simulations are performed to study the influence of PFT on the boundary layer separation. The schematic of this system is demonstrated in Fig. 6.4. Figure 6.5 shows the final choice of grid used in the simulation of the present case. Here, a feedback channel is attached to the ramp foot and upstream of separation. For the current study, injection and suction points are respectively kept at 32 mm and 50 mm away from the leading edge. It has been reported in the literature that choice of the injection station should be in the vicinity of upstream influence location [139] which actually corresponds to a low pressure zone. Further, requirement of a suction station is the high pressure region from the separation bubble; hence the ramp foot remains an obvious choice (Fig. 6.1(a)). As a result of these choices, the maximum amount of trapped fluid would naturally pass through the channel from high-pressure ramp foot region to the low-pressure upstream location. Thus, a feedback channel provides both suction and injection at the same time. The suggestion is also given for the width of the feedback channel [139] and that should be of the order of boundary layer thickness. In view of these points, the final choice of a grid used in the

simulation of present case is given in Figure 6.5. Here, the effects of different channel wall temperature conditions are investigated and wall conditions considered for this purpose are 50 K, 175 K, 300 K and adiabatic wall respectively. However, the thermal boundary condition for the flat plate and ramp is prescribed as isothermal wall of temperature 300 K.

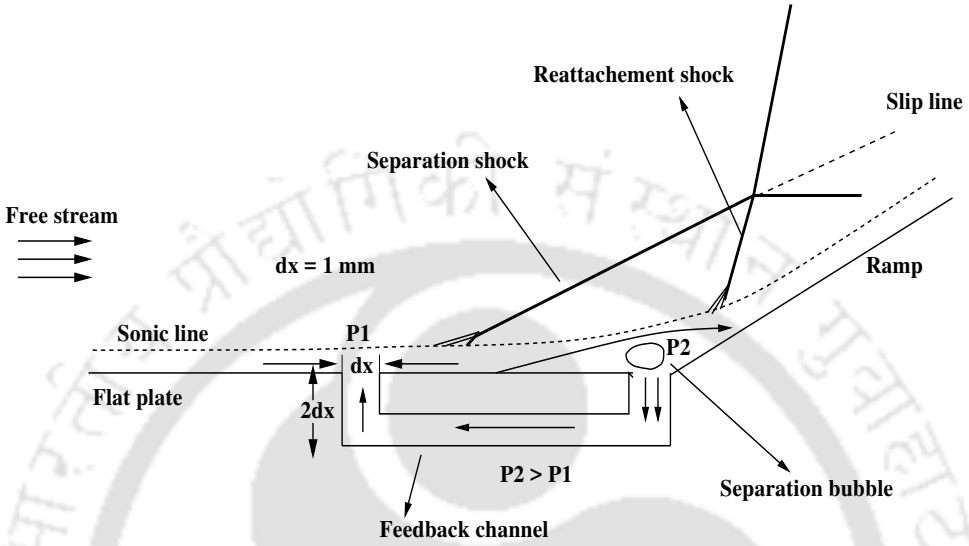

Figure 6.4: Schematic of pressure feedback technique

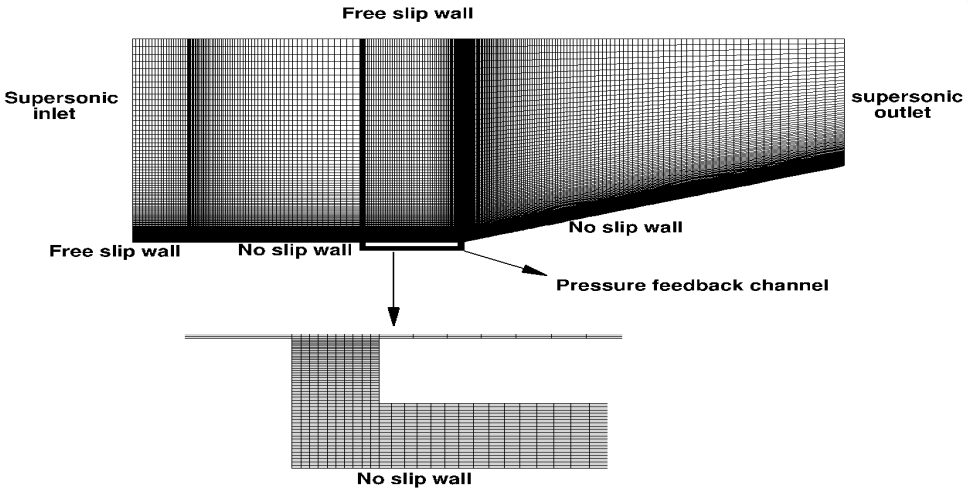

Figure 6.5: Computational domain used for simulation of ramp with sharp leading edge and pressure feedback case

Numerically obtained pressure coefficient and density gradient contours (numerical Schlieren) for pressure feedback case with 50 K channel wall temperature, in comparison

with reference sharp leading edge ramp case without PFT, are given in Fig. 6.6. Presence of weak shock (Fig. 6.6(a) and Fig. 6.6(b)) due to injection and reduction in size of separation bubble (Fig. 6.6(c)) are evident from these figures. These figures also confirm less upstream influence and small recirculation region (Fig. 6.6(c)) due to weaker SWBLI with PFT as compared to the reference case. Same facts are illustrated using plots in terms of various channel conditions in Fig. 6.7. Here, Fig. 6.7(a) shows a small jump in pressure near fluid injection point as a consequence of weak shock wave formed due to pressure feedback channel. Low upstream influence and low plateau pressure are evident from the figure in feedback cases. This alteration in flowfield helps to delay the boundary layer separation. Here, Fig. 6.7(a) also depicts that, modifications in the flow structure are more prominent with the decrease in channel wall temperature. A sudden change in skin friction coefficient (C_f) and heat flux near to fluid injection and suction locations can be noticed in Fig. 6.7(b) and Fig. 6.7(c) for all pressure feedback cases. More importantly, C_f distribution indicates a smaller separation region for all PFT cases as compared to the reference case without PFT. This C_f distribution is used to evaluate the separation size and the same is given in Table 6.3. Here, smallest bubble size is obtained with 50 K channel case; which is 30.68 % less from the reference case. It has relevance with the maximum mass flux for this channel wall condition, though it requires extreme cooling. Apart from this, it has been noticed that marginal cooling of the wall to 175 K also provides sufficient reduction up to 18.18 %. However, in other feedback cases, the nominal reduction is observed. Moreover, it is noticed that adiabatic and isothermal channel of 300 K conditions show similar temperature profiles inside the feedback channel. Consequently, both channel conditions lead to the same amount of separation bubble size.

Table 6.3: Details of separation bubble size obtained for various sharp leading edge ramp cases

Case	Separation bubble size (mm)	Percentage reduction	Mass flux (kg/m^2s)
Reference case	17.6	-	-
Pressure feedback (50 K)	12.2	30.68	3.99
Pressure feedback (175 K)	14.4	18.18	2.76
Pressure feedback (300 K)	15.9	9.65	1.7
Pressure feedback (adiabatic wall)	15.9	9.65	1.7

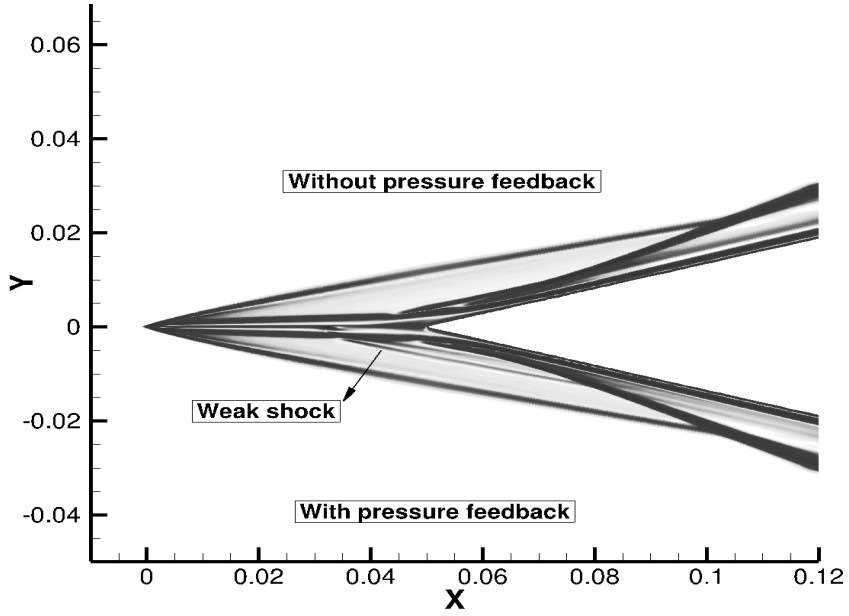

(a) Density gradient contours with (lower) and without PFT (upper)

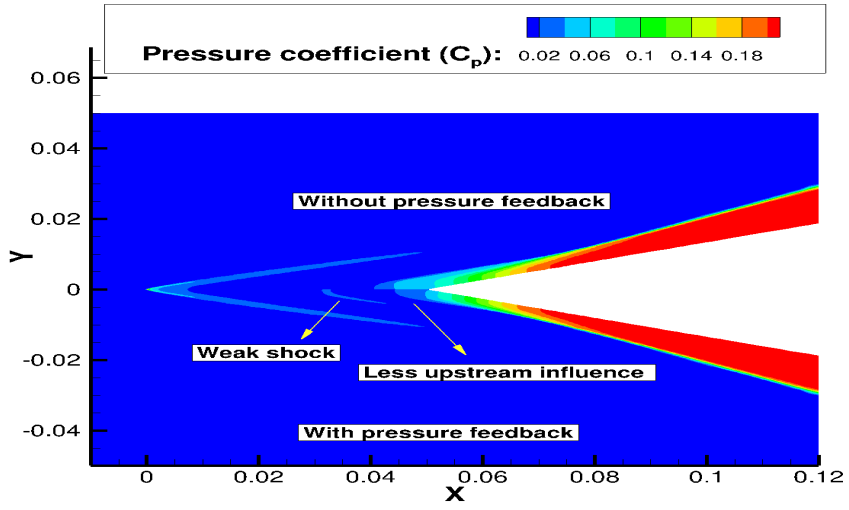

(b) Pressure coefficient contours with (lower) and without PFT (upper)

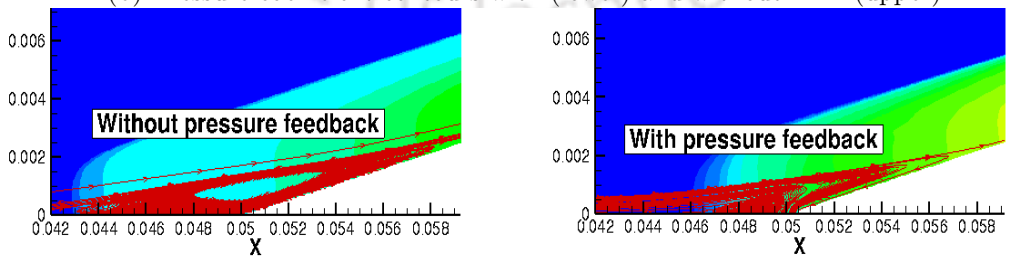

(c) Zoomed view of pressure coefficient contours with (right) and without PFT (left)

Figure 6.6: Pressure coefficient (C_p) and density gradient contours of flow over a plate-ramp configuration

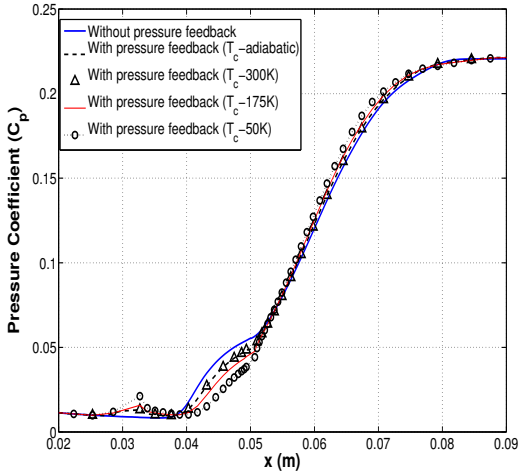

(a) Wall pressure coefficient distribution

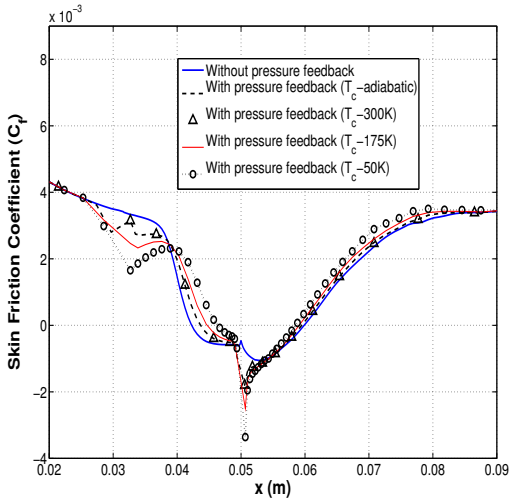

(b) Wall skin friction coefficient distribution

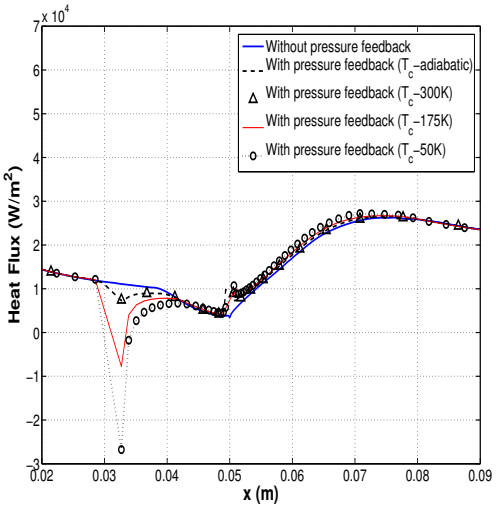

(c) Wall heat flux distribution

Figure 6.7: Comparison of wall property distributions with and without pressure feedback for flow over a sharp leading edge ramp

This discrimination in separation bubble sizes for various cases can be understood by plotting profile of different properties in the direction normal to the wall at a location near the injection station. For this purpose, velocity, Mach number and temperature variation in the direction normal to the wall at 35 mm and 45 mm from leading edge are plotted in Fig. 6.8. Choice of these locations is based on the fact that the injection point of the feedback channel is 32 mm downstream from the leading edge. This injection location and consequently the fluid injected from this location do not lead to any change in the flow properties upstream of the fluid injection location (32 mm). This fact is very much noticeable from Fig. 6.6 and Fig. 6.7 where wall property variation is identical at any location upstream of the injection location (before 32 mm) for both (with and

without PFT) cases. From Fig. 6.8, the increment in velocity and temperature boundary layer thickness is very much evident in stream wise direction for all cases. Moreover, fluid injection is seen to provide momentum to the flow, with pressure feedback cases, so as to earn fuller velocity profiles in comparison to reference case without PFT.

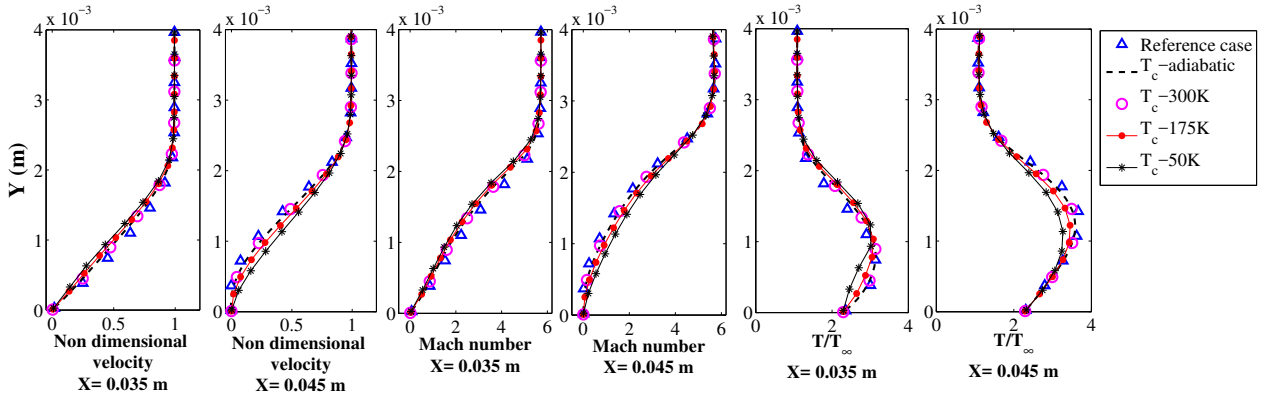

Figure 6.8: Variation of properties in the boundary layer at different locations for different feedback channel temperature

Further, all the velocity profiles with PFT corresponding to 35 mm location do not portray flow separation. But, except for 50 K case, other velocity profiles depict flow separation at 45 mm. This observation is in line with the fact displayed in Fig. 6.7(b) where separation locations are 42.3, 43.6, 44.7, 46.3 and 43.6 mm for reference, 300 K, 175 K, 50 K and adiabatic cases respectively. The major reason for decreased separation with cooled channels (50 K, 175 K) lies in the fact that, ingested fluid from the separated region attains lower temperature and in turn lower viscosity. This low temperature fluid, when gets injected and further convected downstream, reduces the temperature of fluid in the boundary layer and increases the ramp approach Mach number of the flow (Fig. 6.8). Further, low-temperature channel wall results in high recirculated mass flow rate through the channel and leads to lower separation region than other cases since it bears larger potential for suction of retarded air. Thus, lowering of channel temperature raises its suction potential of retarded air and increases recirculated mass flow rate through the channel. Hence, cooled PFT channel leads to a lower separation region than other cases. However, the adiabatic and 300 K isothermal cases deal with fluid of same properties and mass flux at suction and injection stations. Therefore, both the cases portray the same boundary layer variation and in turn the separation bubble size. Thus, these cases also project the consistency in simulation results. Thus, studies for the effect of channel wall conditions have revealed that reduction of channel wall temperature lowers the separation bubble size.

6.4.2 Effect of ramp angle on pressure feedback separation control system

Simulations are carried out to analyse the effect of ramp angle on the performance of PFT. Hence, different ramp angles of 14^o, 15^o and 17^o are considered herein for parametric analysis. Along with the no-slip boundary condition, isothermal wall condition of 175 K and 300 K are considered for channel and plate-ramp parts of the configuration, respectively. It is well known that the high ramp angle imposes greater adverse pressure gradient on the incoming flow. Figure 6.9 also shows enhancement in parameters like upstream influence, plateau pressure, heat flux and separation length with an increment in ramp angle. On the other hand, high plateau pressure fetches a higher driving pressure difference between the suction and injection locations of PFT. Therefore, it is expected to have enhanced recirculated mass flow rate through the feedback channel. Hence, the possibility of higher mass flow through the channel is expected to boost the controllability of PFT with an increment in ramp angle. However, on the contrary, Table 6.4 indicates a lesser decrement in separation bubble size with increase in ramp angle. To investigate it, numerically obtained Mach number contours of 14^o and 17^o ramp geometries, without PFT, are shown in Fig. 6.10. In this figure, the large separation area and higher amount of entrapped mass are noted for high ramp angle case. Thus, relatively higher channel mass flux is found to be less efficient in reducing the separation as that for lower ramp angles. Moreover, Fig. 6.11 portrays the existence of higher temperature in the boundary layer along with thicker hydrodynamic and thermal boundary layers for higher angle case. Thus, stronger impedance against separation control and accordingly lower suction rate of dead mass are the major observations for lesser reduction in bubble size with the increment in ramp angle for a cooled PFT attachment.

Table 6.4: Details of separation bubble size obtained for various ramp angle cases

Case	Separation bubble size without PFT (mm)	Separation bubble size with PFT (mm)	Percentage reduction	Mass flux (kg/m^2s)
14^o	13.9	11.2	19.42	2.34
15^o	17.6	14.4	18.18	2.76
17^o	24.9	21.9	12.04	3.56

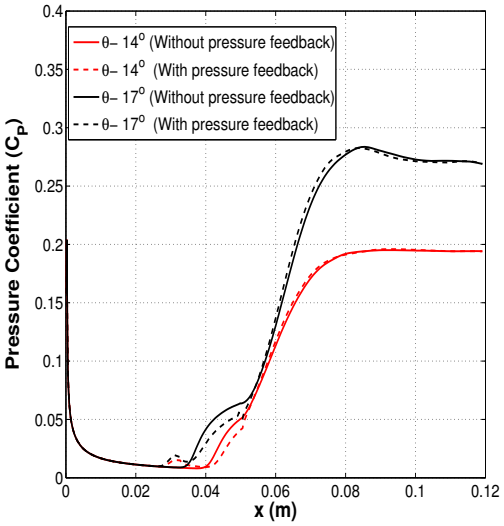

(a) Wall pressure coefficient distribution

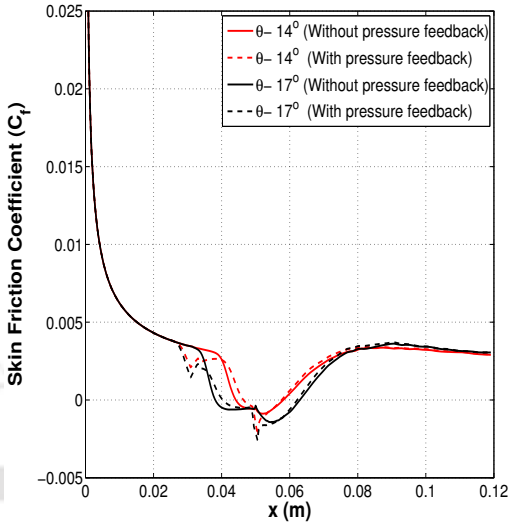

(b) Wall skin friction coefficient distribution

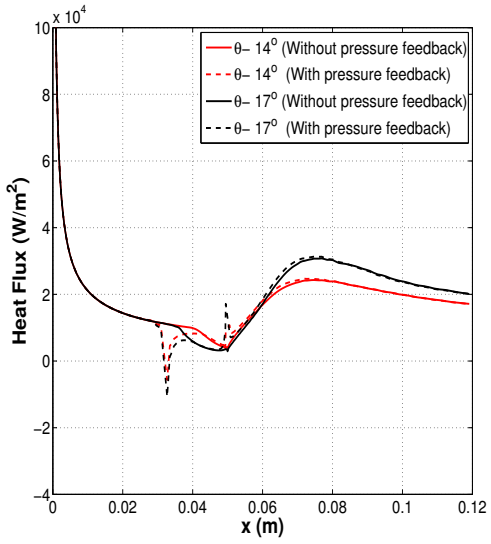

(c) Wall heat flux distribution

Figure 6.9: Effect of ramp angle on wall property distributions with and without pressure feedback for flow over a sharp leading edge ramp

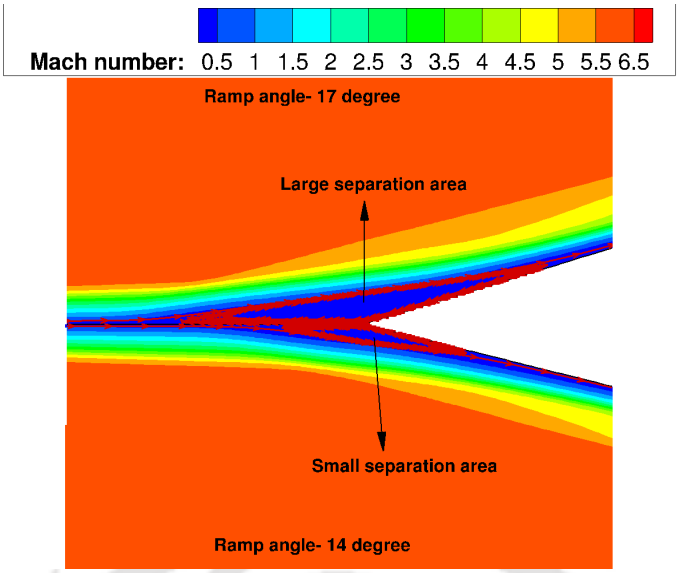

Figure 6.10: Mach number contours of flow over a plate-ramp configuration for different ramp angles without pressure feedback

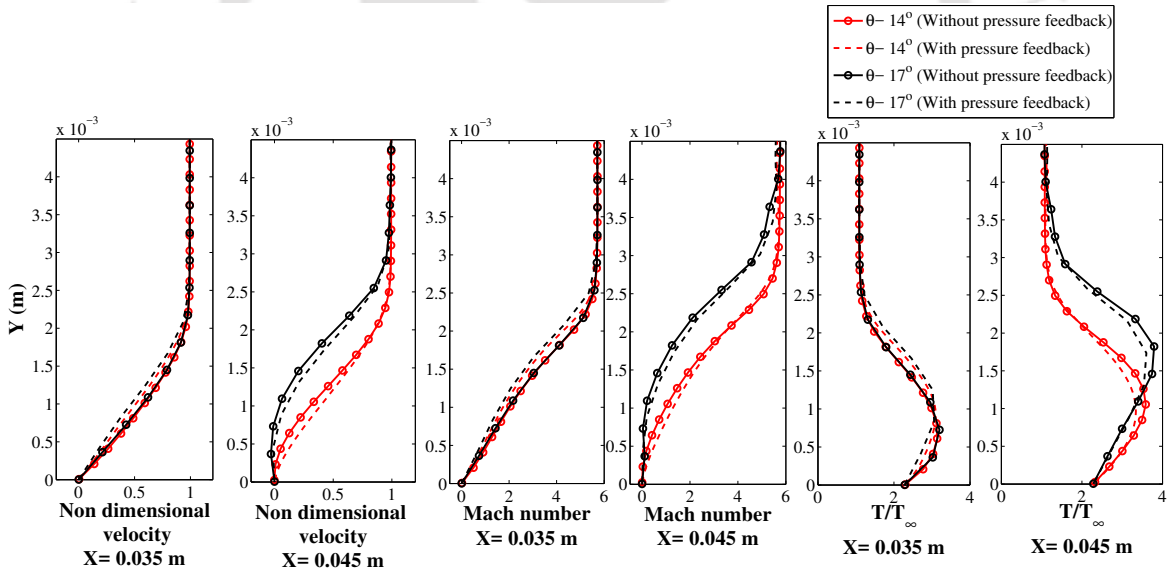

Figure 6.11: Variation of properties in the boundary layer at different locations for different ramp angles

6.4.3 Effect of wall and freestream total temperature on the pressure feedback separation control system

It has been observed in the literature [120, 123] that increased wall temperature for a given freestream condition increases the extent of separation. Further, higher freestream total temperature is found to reduce the separation bubble size for same wall conditions. But,

the wall temperature to total temperature ratio is noted to be the governing parameter since separation dynamics is found to be dependent on this ratio rather on the individual temperatures. In view of this, simulations are planned to evaluate the effect of T_{wall}/T_0 on the PFT with 15^o ramp model (reference case). In the present investigation, three freestream total temperatures viz 1080, 1800 and 3000 K, are considered as detailed in Table 6.5. Here as well, the channel condition (175 K) is taken as mentioned in the previous section. Key parameters like wall temperature to total temperature ratio, Mach number and Reynolds number are kept the same as 0.278, 6 and 8×10^5 m^{-1} respectively. Further, the in-house developed reacting solver is also wielded herein to simulate the high enthalpy flowfield (total temperature- 3000 K). Separation bubble size obtained for all the wall and total temperature conditions are found to be same (17.6 mm) without PFT. This can be confirmed from Fig. 6.13 which demonstrates equal separation area for different freestream stagnation enthalpy conditions. Further, high-density fluid inside recirculation region is also noted for high enthalpy case. Interestingly, the use of cooled PFT (175 K) provides the greater mass flow rate (8.72 kg/m^2s) through the feedback channel for the high enthalpy case as compared to low enthalpy simulation (2.76 kg/m^2s). Thus, it has more separation decrement (31.25 %) as that of low enthalpy cases (Fig. 6.12(b)). Hence, removal of more dead air at high enthalpy condition, for same T_{wall}/T_0, in the presence of cooled PFT channel, leads to more separation decrement.

Table 6.5: Details of wall and freestream total temperature cases

Case	T_{wall} (K)	T_0 (K)
1	300	1080
2	500	1800
3	834	3000

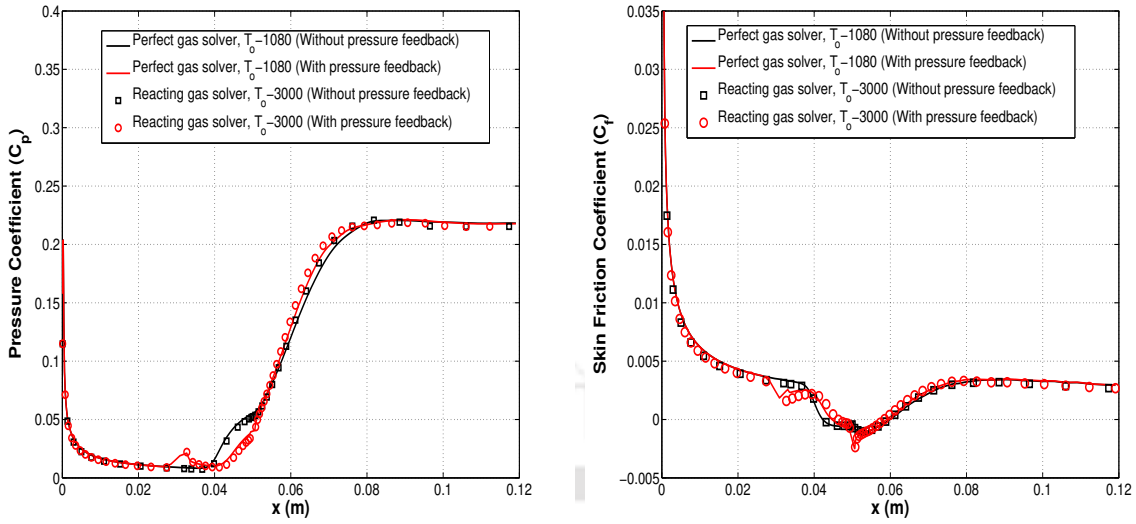

(a) Wall pressure coefficient distribution (b) Wall skin friction coefficient distribution

Figure 6.12: Effect of freestream enthalpy on wall property distributions with and without pressure feedback for flow over a sharp leading edge ramp

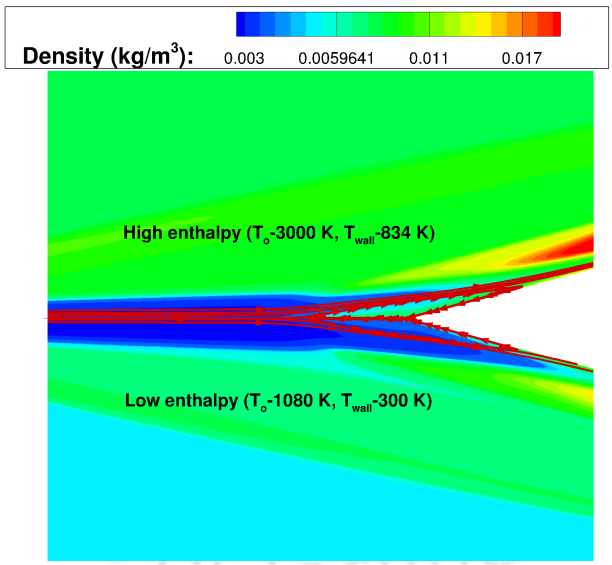

Figure 6.13: Density contours of flow over a plate-ramp configuration for different freestream enthalpies without pressure feedback

6.4.4 Studies for combined effect of leading edge bluntness and pressure feedback system

Before performing simulations with simultaneous use of both the techniques, computations are performed only with leading edge bluntness radius. Here as well, along with no-slip boundary condition, isothermal wall boundary condition of 300 K is considered for

plate-ramp parts of configuration. These simulations are performed using the freestream conditions given in Table 6.1. Four leading edge radii viz. 0.0, 0.3, 0.5 and 1.0 mm are considered to examine the effects of leading edge bluntness [186]. Here, a grid of size 415×120 along with the same numerical strategy as described in the validation section is used for the baseline blunt leading edge simulations. Presence of leading-edge bluntness alters the shock structure by changing attached leading edge shock with the detached bow shock. Therefore, properties like pressure, temperature, density, Mach number get altered at any section downstream of leading edge which in turn change the SWBLI pattern at the ramp and flat plate junction. Separation bubble sizes, evaluated using C_f distribution for sole leading edge bluntness technique, are given in Table 6.6. This table also hints at the existence of inversion and equivalent blunt radii. Here, radius 0.5 mm is the inversion radius since it corresponds to maximum separation bubble size. On the other hand, separation bubble size approaches an equal value as that of the reference sharp leading edge at the equivalent blunt radius of 1 mm. These values and associated tags are in agreement with the one reported by John and Kulkarni [4]. For radius lower than the equivalent radius, swallowing of entropy layer by the boundary layer is dominant. This phenomenon leads to the presence of high temperature fluid in the boundary layer. Therefore, higher viscosity of the fluid makes it more separation prone than the corresponding baseline case. Besides, for radii higher than the equivalent radius, entropy layer remains thicker than the boundary layer which provides strong vorticity above the boundary layer. This inviscid vorticity and the favourable pressure gradient together stabilize the boundary layer more than the baseline case. Thus, present studies with simultaneous use of two control techniques are centered on the assistance of PFT in reduction of the equivalent radius and also the intensity of interaction for all radii. The schematic of this arrangement is shown in Fig. 6.14.

Table 6.6: Details of separation bubble size obtained for various blunt leading edge radii

Case	Separation bubble size (mm)
0.0 mm (Reference case)	17.6
0.3 mm	28.6
0.5 mm	30.6
1 mm	20.1

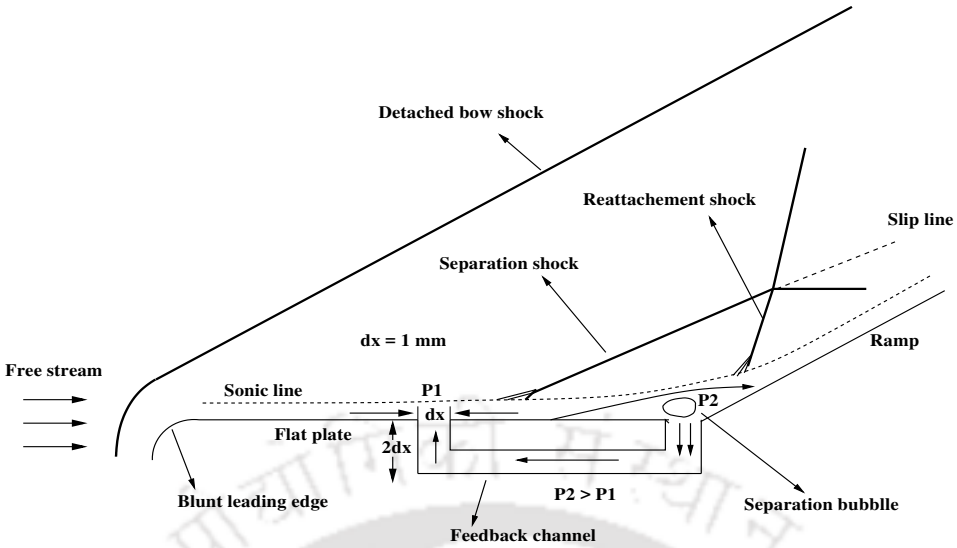

Figure 6.14: Schematic of an integrated arrangement of blunt leading edge and pressure feedback technique

Simulations for the integrated effect of both the control techniques are carried out for the reference plate-ramp geometry with 0.0, 0.3, 0.5 (inversion radius) and 1.0 mm (equivalent radius) leading edge radii along with the pressure feedback system. The pressure feedback channel is maintained at 175 K for all the simulations while ramp and plate are maintained at 300 K. Same freestream conditions, given in Table 6.1, are used for these computations. Numerically obtained pressure, skin friction and heat flux distributions for the inversion and equivalent radii are shown in Fig. 6.15. It is clear from the figure that the plateau pressure region and the separation size decrease for all radii in the presence of a pressure feedback system. It is clearly visible that coupling of pressure feedback system with blunt leading edge radius pushes separation point further downstream. The corresponding alteration in wall heat flux is also evident herein. Figure 6.16 portrays a remarkable reduction in separation size using both the control systems compared to sole blunt leading edge technique. Here, the use of cooled PFT (175 K) along with blunt leading edge provides mass flow rate of 4.47, 4.64 and 3.79 kg/m^{2}s through the feedback channel for the blunt leading edge cases of 0.3, 0.5 and 1.0 mm respectively. As a consequence the decrement in equivalent radius and intensity of interaction for any radius below it are the major achievements of the proposed integration. Thus, present simulations show that it is possible to reduce the minimum leading edge radius (equivalent radius) above which separation control is guaranteed with the provision of a cooled pressure feedback channel.

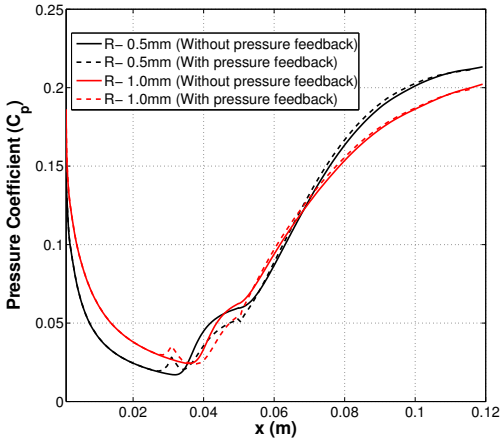

(a) Wall pressure coefficient distribution

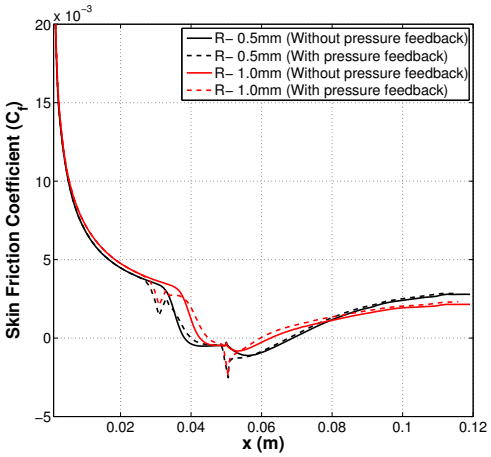

(b) Wall skin friction coefficient distribution

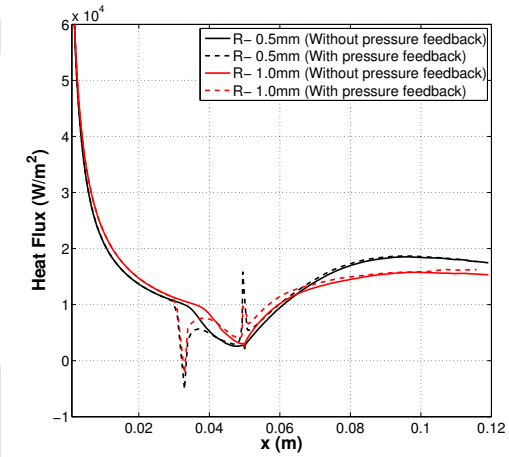

(c) Wall heat flux distribution

Figure 6.15: Wall property distributions with leading edge bluntness alone and with PFT

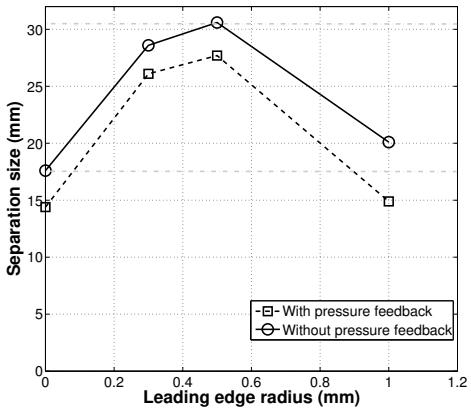

Figure 6.16: Separation bubble size for different leading edge radii with and without PFT

Variation of velocity in the direction normal to the wall for equivalent and inversion radii with and without PFT is shown for two locations in Fig. 6.17(a) and Fig. 6.17(b). This figure also provides the information of entropy layer in the velocity boundary layer plot. Due to unaltered upstream, in the presence of PFT, no change in the thickness of entropy boundary layer is noticed. It is mainly due to the fact that entropy layer thickness is dependant on the height of the curved portion of the standing shock. Shape and position of the bow shock, being upstream of the pressure feedback arrangement, remains unaltered due to integration of two control techniques. Thus, PFT does not alter the entropy layer thickness; hence, the inviscid vorticity above the boundary layer is not responsible for reduction in equivalent radius. Therefore, PFT based changes in the boundary layer due to suction and injection of the fluid are responsible for reduced magnitude of the critical radius and associated intensity. This phenomenon can be illustrated using near wall profiles of velocity at various locations for 0.5 mm and 1 mm blunt radii as shown in Fig. 6.17(a) and Fig. 6.17(b). Here, in the presence of PFT, more stable boundary layer against separation can be seen. This analysis supports the reduction in separation region by 15 % (Fig. 6.15(b)), as compared to the sharp edge reference case, for the equivalent radius (1 mm). Hence, it is clear that coupling of control techniques improves the performance of the blunt leading edge of any size by weakening SWBLI strength as shown in Fig. 6.16. Therefore, a proposition of a three dimensional configuration of a feedback channel, close to the interaction zone, is given in Fig. 6.18, for maximum reduction in SWBLI intensity.

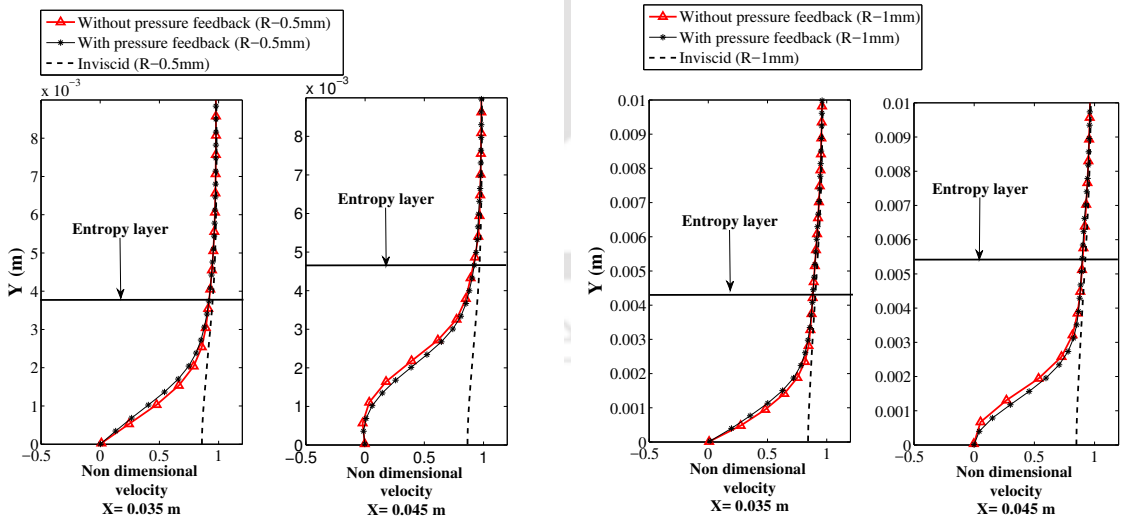

(a) Non dimensional velocity profile (R-0.5mm)

(b) Non dimensional velocity profile (R-1mm)

Figure 6.17: Non-dimensional velocity variation in the boundary layer at different locations for R-0.5mm and R-1mm leading edge cases

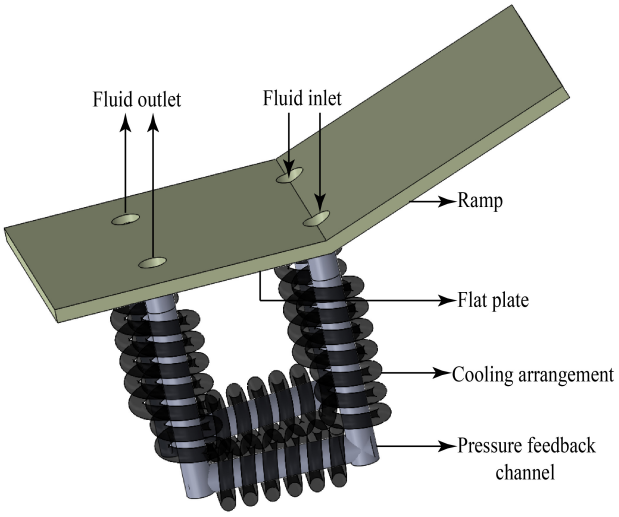

Figure 6.18: Proposed pressure feedback arrangement

6.5 Conclusion

Numerical simulations are successfully carried out using perfect and reacting in-house flow solvers for assessment of PFT in lowering the intensity of SWBLI at the ramp foot. It has been noticed that cooling of the feedback channel reduces the intensity of SWBLI by removing more amount of dead air mass. Marginal cooling of the channel to 175 K has helped to reduce the separation bubble size by 18.18 %. An extremely cooled channel of 50 K temperature is found effective in reducing separation by 30 %. Studies with different ramp angles showed that the effectiveness of PFT decreases with an increase in ramp angle in spite of higher mass flow rate through the cooled pressure feedback circuit. Simulation with high enthalpy reacting flow solver revealed that the cooled PFT channel is more effective in reducing separation than that of low enthalpy perfect simulation for same wall temperature to total temperature ratio. Investigations are then performed with the blunt leading edge and cooled pressure feedback arrangement since the perfect gas flow simulations for PFT have proved that the cooled channel has higher potential in reducing the separation bubble size. Reduction in intensity of SWBLI for all radii, in the presence of PFT, is one of the prominent observations of present investigations. This integrated arrangement has reduced the magnitude of inversion and equivalent radii. Here, instead of the boundary layer and entropy layer interaction, suction and injection in the presence of appropriate pressure feedback arrangement have been accounted for this enhanced control. Thus, present studies recommend the use of cooled PFT with leading edge bluntness for effective control of boundary layer separation.

CHAPTER 7

PROBING REAL GAS AND LEADING EDGE BLUNTNESS EFFECTS ON SHOCK WAVE BOUNDARY LAYER INTERACTION AT HYPERSONIC SPEEDS

Overview

Present chapter is centered on understanding the discrepancies in shock wave boundary layer interaction (SWBLI) for perfect and real gas flows. In order to perform numerical studies, the in-house developed CFD solvers are integrated with a gradient based optimization algorithm to predict the critical radii of SWBLI in case of perfect and real gas flows. Presently developed high fidelity approach has been observed to be useful in precise estimation of critical radii of bluntness. Further, studies for SWBLI revealed that the real gas effects reduce the extent of separation in comparison with perfect gas flow and also necessitate lower magnitudes of critical radii. It has been noted that reduced requirement of high entropy layer thickness and upstream over pressure region pose need of lower value of inversion and equivalent radii for reacting flow conditions. Therefore, larger estimate of equivalent radius of SWBLI, obtained for perfect gas flow conditions, or any radius larger than that would definitely provide the necessary separation control for flows with real gas effects.

7.1 Introduction

Supersonic or hypersonic flows face major impediment of shock wave boundary layer interaction (SWBLI). Such interaction is evident in laminar as well as turbulent flows. Any spacecraft or aircraft component, which either encounters sudden turning due to ramp like disturbances or receives shock impingement, gets affected due to SWBLI. As noted earlier, former type of interaction is called as ramp induced SWBLI (R-SWBLI)

while the later is termed as impingement based SWBLI (I-SWBLI). In the presence of any of these SWBLI types, control surfaces or engine parts encounter adverse effects such as flow separation, boundary layer transition, higher surface heating or vortex shedding. Hence, it is highly desirable, primarily, to understand the basics of interaction [120, 123], predict the interaction parameters [102, 106, 124] and then to control or lessen the harm incurred to various engineering systems or sub-systems [188–190] in its presence. Such control would not only enhance the performance of the associated components but also would ensure safety of the space flight. Therefore, it necessitates to device techniques or methods to control the SWBLI.

The leading edge bluntness based passive separation control method has been noticed to have an anomalous trait since the necessary separation control is not possible for all the leading edge radii. It has been found that, initial increment in leading edge radius, provided with the intention of separation control, actually enlarges the length of separation bubble size. As a consequence of this, extent of separation reaches its peak at a specific (inversion) radius. Further increment of leading edge bluntness decreases the separation bubble size. But, still it needs to have a critical value of bluntness (equivalent radius), so as to experience the separation bubble as that of the sharp leading edge configuration. Thus, there are two special or critical radii, viz. inversion radius and equivalent radius, and value of those should be identified in advance. Prediction of inversion radius is essential since it corresponds to maximum separation bubble size. It is advisable to know the equivalent radius since any radius of magnitude higher than this would only be considered for separation control.

Since leading edge bluntness need not always decrease the separation size in comparison with reference sharp leading edge case, it is essential to predict the critical radii (inversion and equivalent) associated with this passive control technique. In view of this requirement, present chapter focuses on development of high fidelity methodology for estimating the critical radii of R-SWBLI for perfect gas and high enthalpy flows. Such detailed investigations are essential since some of the literature reported findings have either dealt with only inversion radius [133, 186] and/or explored for both the radii but without considering the standard optimization techniques [4]. As an outcome of those studies, a wide range of radii would be recommended between which it can be expected to have the critical radius. Hence, it is better to integrate the CFD solver with an optimization procedure to arrive at the precise value of critical radii or to narrow their range of prediction. Further, there have been suggestions about prediction of critical radii for a given freestream condition and ramp angle [119]. As per this suggestion, thickness of entropy layer becomes equal to the boundary layer around the upstream influence location for inversion radius. And the upstream over pressure region or favorable pressure

gradient reaches the upstream influence location when the leading edge radius becomes equal to equivalent radius. Having these informations, it is still difficult to predict the critical radii for a given hypersonic flow and plate-ramp configuration, since it demands information of the entire flowfield. Further, these observations are made specifically for a perfect gas flow only; therefore a revisit is required for a high enthalpy flow condition. So, one of the milestones of present investigations is to crosscheck the validity of hints about the flowfield around the critical radii for a high enthalpy flow. This process also puts forth the observation of real gas effect on SWBLI. Effect of enthalpy has been mentioned in the literature [135] but the consideration of real gas effects remains unattained. Therefore a methodology, suitable for low and high enthalpy flows, is not only planned for obtaining estimates of critical radii of SWBLI but also to verify the resemblance in the flow features around the critical radii in either cases. In view of these objectives, an in-house developed high temperature reacting flow solver, integrated with an optimization procedure, is used for formalizing the philosophy of critical radii prediction for R-SWBLI. Details of these results and associated analysis are discussed in this chapter.

7.2 Validation

Reacting flow solver is also used for simulating the low enthalpy freestream hypersonic flow over a plate-ramp configuration with different leading edge radii as considered by John and Kulkarni [4]. Typical computational domain and associated boundary conditions are shown in Figure 7.1. Same freestream conditions given in Table 7.1 are also employed for this part of the study as taken by John and Kulkarni [4]. The convective fluxes are computed using AUSM scheme while viscous fluxes are computed as discussed in chapter 2. The final choice of mesh with total number of cells close to 40000 are taken, where the grid along the blunt leading edge, the flat plate and the ramp surface is maintained at a first cell height close to 3×10^{-5} m, for sharp and blunt leading edge cases, after elaborate mesh-independent studies. Thus obtained skin friction coefficient and pressure coefficient plots for leading edge radius of 0.3 mm are shown in Figure 7.2(a) and (b). It is evident here that the real gas effects are not prominent and therefore the results reported by John and Kulkarni [4] for perfect gas flow portray encouraging match with the present real gas flow. Skin friction variation can be used to predict the separation length. This prediction of separation length for sharp as well as blunt leading edge case are same in magnitude for perfect and real gas flows as mentioned in Table 7.2. Thus, from this test of total temperature (1080 K) and isothermal wall boundary condition (300 K), it is clear that absence of chemical reactions and least variation of specific heats make no difference in SWBLI for perfect as well as real gas flows.

Table 7.1: Details of freestream conditions and various leading edge radii considered for validation

Mach number	Pressure (Pa)	T_∞ (K)	T_{wall} (K)	Re (m^{-1})	Leading edge radii (mm)
6	199.4345	131.7	300	8×10^5	0.3, 0.5

Table 7.2: Details of result for validation of present reacting gas solver with John and Kulkarni [4]

Case	Separation point (mm)	Reattachment point (mm)	Plateau pressure (Pa)
0.3 mm			
Perfect gas	38.10	67.18	505.27
Reacting gas	37.60	67.50	504.07
0.5 mm			
Perfect gas	38.28	68.84	527.41
Reacting gas	38.00	69.20	526.60

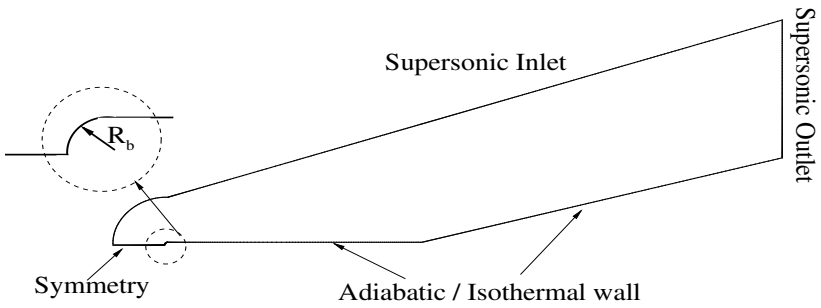

Figure 7.1: Schematic diagram for the computational domain and associated boundary conditions

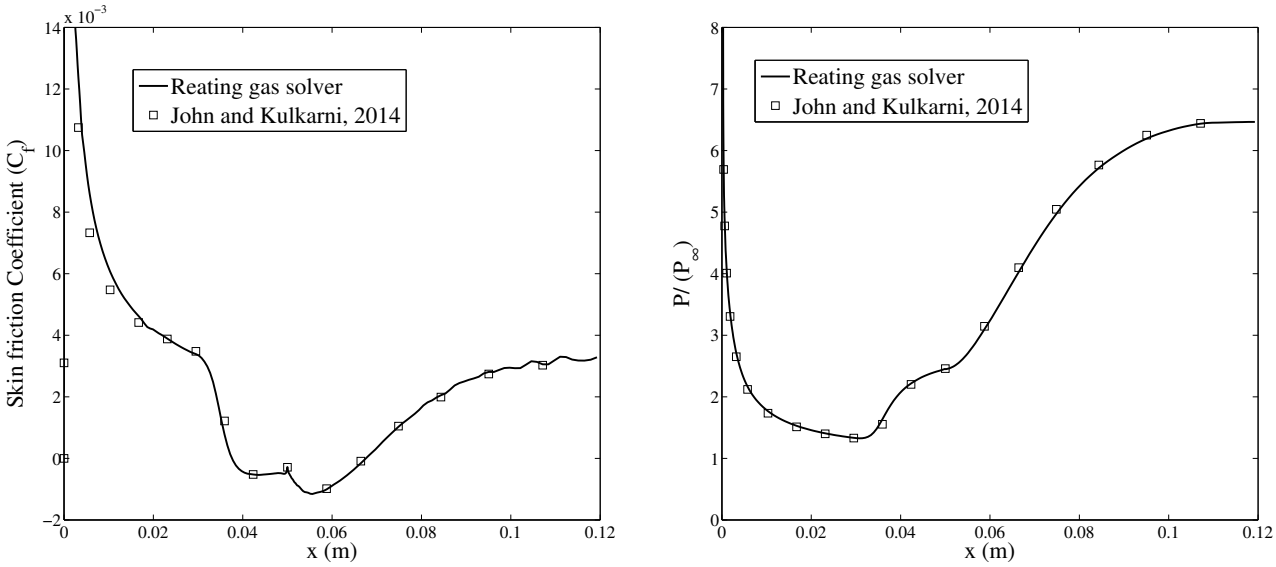

Figure 7.2: Comparison of (a) skin friction coefficient C_f and (b) surface pressure P/P_∞ with John and Kulkarni [4]

7.3 Integration of CFD solver and gradient method

A standard optimization procedure yields significant leverage by maximizing or minimizing certain objective functions or generating feasible solutions for hard combinatorial optimization problems, however it is also plagued by its limitations. One such limitation is the computational time involved in the process from initial guess to final optimal solution, especially when the optimization technique employed relies on Computational Fluid Dynamics (CFD) for the function evaluations [191]. Therefore, the greedy algorithm like Gradient method, which is known for its fast convergence for unimodal problems, is employed for present investigations. In this section, the various segments that are an integral part of such optimization framework are discussed. Particularly, the objective function for the present study, the optimization algorithm employed and the flow-solver used to evaluated the cost function are highlighted herein.

Gradient based method (GM) is opted here for integration with in-house CFD solvers. The flow-chart depicting the algorithm behind the optimization methods is shown in Figure 7.3. For the GM based optimization technique, process is initiated with an initial guess and then its sensitivities are obtained using finite forward difference approximation. Each optimization cycle consists of two function evaluations i.e. one each for the gradient estimation, $\nabla f(x^k)$ and the perturbed decision variable, x^{k+1}. The perturbed decision variable is obtained as shown in Figure 7.3, where λ^k is the adaptive step function at a particular optimization iteration k, used to control the rate of convergence and is defined

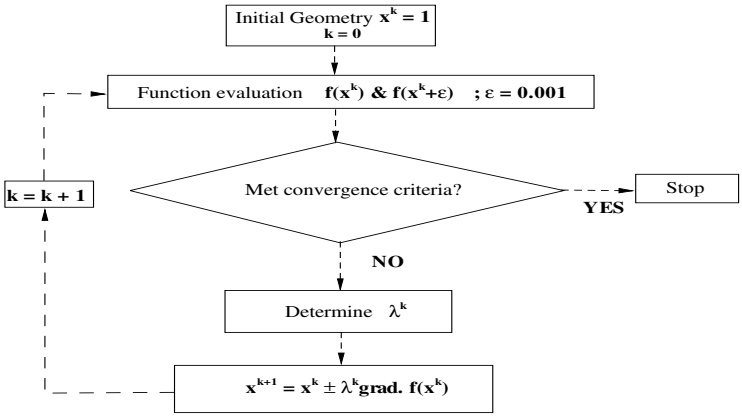

Figure 7.3: Schematic diagram describing a typical Gradient Method based algorithm

as,

$$\lambda^k = \begin{cases} A\lambda^{k-1} & ;\text{if } f(x)^k < f(x)^{k-1} \\ B\lambda^{k-1} & ;\text{otherwise} \end{cases}$$

where, A and B are constants whose values depend on the test case, with the inequality sign reversed for steepest ascent. These constants are used to accelerate the convergence towards final optimal solution.

Major objective of present chapter is to predict the critical radii of bluntness for R-SWBLI using perfect and reacting gas flow solvers to understand the real gas effect. This study is undertaken by evaluating dual critical radii R_b and hence R_b forms the decision variable for this test case with bounds [0,0.003]m. Basic sharp leading edge geometry for which leading edge bluntness based separation control is to be investigated is same as discussed in previous section. One of the critical radius, inversion radius, $R_{b,inv}$ corresponds to maximum extent of separation. Therefore the first objective function (f(x)) for prediction of $R_{b,inv}$ is L_{R_b}=$L_{R_b,max}$, where L_{R_b} is the separation length of the bubble formed at the ramp foot, with subscript R_b signifying the corresponding radius of the blunt leading edge. In case of, equivalent radius $R_{b,eq}$, the separation bubble size is same as that of the sharp leading edge. Hence the objective function in that case is such that the $|L_{R_b=0} - L_{R_b}|$<=10^{-03}. Further, it is known that inversion radius is smaller than the equivalent radius. Therefore, separation details of sharp leading edge case are used to start the optimization procedure for predicting the inversion radius in either cases. But, any radius higher than inversion radius can be thought as initial guess for prediction of equivalent radius for both cases. Figure 7.4 describes the schematic of the algorithm considered to couple to CFD code with Gradient Method procedure.

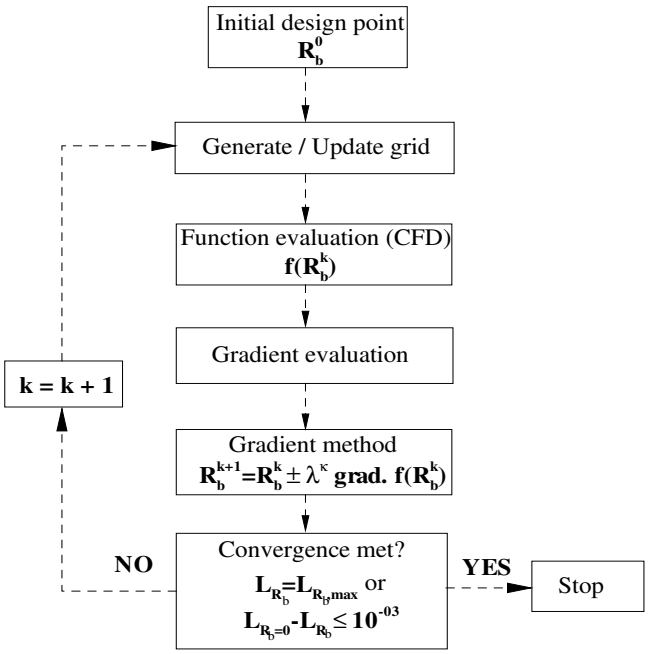

Figure 7.4: Schematic behind the algorithm used to couple the in-house CFD solvers and Gradient Method technique

7.4 Results and discussions

Freestream conditions used to study the real gas effects in R-SWBLI are given in Table 7.3. These conditions are given as inlet boundary conditions for both, perfect as well as reacting gas flow solvers, while integrating with the above mentioned optimization procedure. Adiabatic wall boundary condition is employed specifically to enhance the high temperature effects for these freestream conditions of total temperature 3000 K. As an outcome of this, for sharp leading edge case itself, 0.0381 mm and 0.0308 mm separation bubble sizes are noted for perfect and real gas flow simulations, respectively. With this initial guess, optimization is processed for predicting inversion radius. Results obtained at an intermediate state are used to analyze the real gas effects. Figure 7.5 portrays the separating streamline and separation bubble and clearly depicts the higher separation length for perfect gas flow condition. Variation of specific heats and possibility of chemical reactions have lessened the maximum temperature in the domain for reacting flow case. Viscosity of the fluid is also less which in turn leads to lower boundary layer thickness. Therefore, extent of separation is expected to be less with real gas effect. One of the major objective of the present studies is to highlight and quantify this effect for R-SWBLI. Therefore, skin friction coefficient has been obtained as an outcome of CFD simulations for each optimization cycle and it is shown in Figure 7.6 for two sample cases,

along with the reference sharp leading edge case. From the Figure 7.6, separation bubble size is estimated for different radii. It is evident from the figure that the prediction of separation bubble size is higher with perfect gas flow simulations. As mentioned earlier, lower increment of viscosity due to rise of specific heats and endothermic chemical reactions are accounted for lower separation length in the reacting flow simulations. Variation of surface pressure coefficient C_p distribution along the wall surface is shown in Figure 7.7. Observations like lower separation length, lesser upstream influence, lower plateau pressure etc., in case of reacting gas flow, can also be made from pressure variation.

Table 7.3: Freestream conditions for the given study

Parameter	Freestream condition
M_∞	6
T_∞	365.85 (K)
P_∞	406.63 (Pa)

Separation length obtained for each intermediate radius is plotted as a result of complete optimization procedure in Figure 7.8. A noticeable observation over here is the lower value of inversion radius with real gas effects. Optimization procedure then continued for equivalent radius with both the solvers. Thus obtained separation bubble size for intermediate and final radii is also given in Figure 7.8. As per the definition of equivalent radius, it was needed to match the separation bubble size with sharp leading edge case. At this reference state itself, reacting solver has showed lower separation than the perfect gas flow solver, hence the extent of separation at equivalent radius from reacting gas flow solver is lower than the perfect gas flow solver. Therefore, the radius, at which the equivalent separation is noticed, is also lower in case of reacting flow simulations.

Detailed flowfield analysis at respective critical radii can help in understanding the difference between the results obtained from both the solvers. Initially, entropy layer boundary layer interaction is considered to inspect for the inversion radius. Here as well, high entropy layer is defined using the streamline which passes through the edge of the curved bow shock. Height of this streamline at the leading edge is taken to be twice of the leading edge radius [4]. Thickness of HEL is 1.68 mm for perfect gas flow case at the leading edge while the same for the reacting gas flow is 1.562 mm at the same location. This difference is mainly due to lower shock stand-off distance in case of flow with real gas effects. Decrement of shock stand-off distance for reacting flow in comparison with the perfect gas flow has been reported earlier in chapter 3 as well. Velocity variation normal to the wall at a reference location for different radii is plotted in the Figure 7.9 and Figure 7.10. for both the cases. This figure includes variation for inviscid as well as

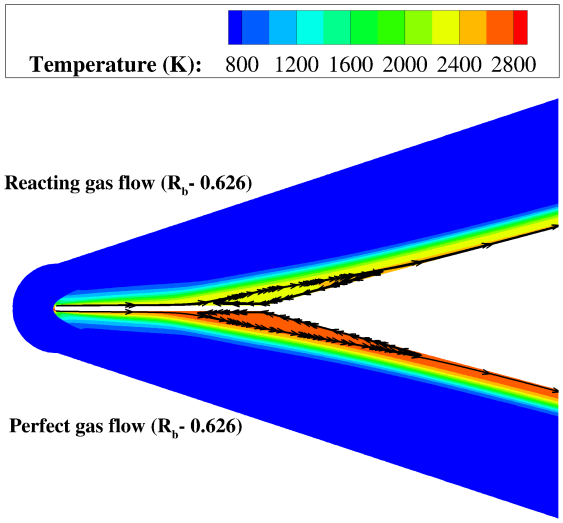

Figure 7.5: Temperature contour for leading edge radius $R_b = 0.626$ mm, for perfect gas and reacting flow simulations

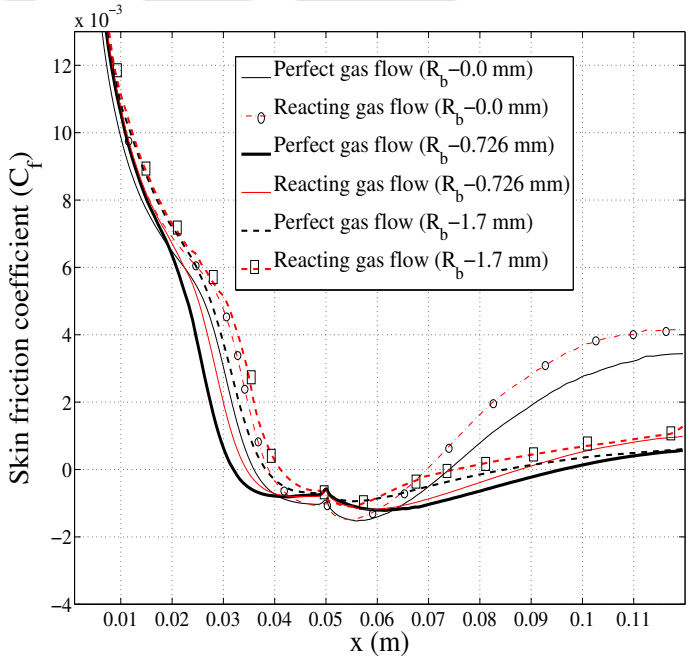

Figure 7.6: Skin-friction coefficient for sample leading edge radii

viscous simulations in order to estimate the boundary layer thickness for the flow with stream-wise pressure gradient. Asymptotic match between inviscid and viscous velocity profiles gives the thickness of boundary layer in this figure. Edge of HEL at corresponding location is also shown in the same figure. Therefore, Figure 7.9 and Figure 7.10 clearly depict that the boundary layer thickness is lower than the HEL at the location upstream

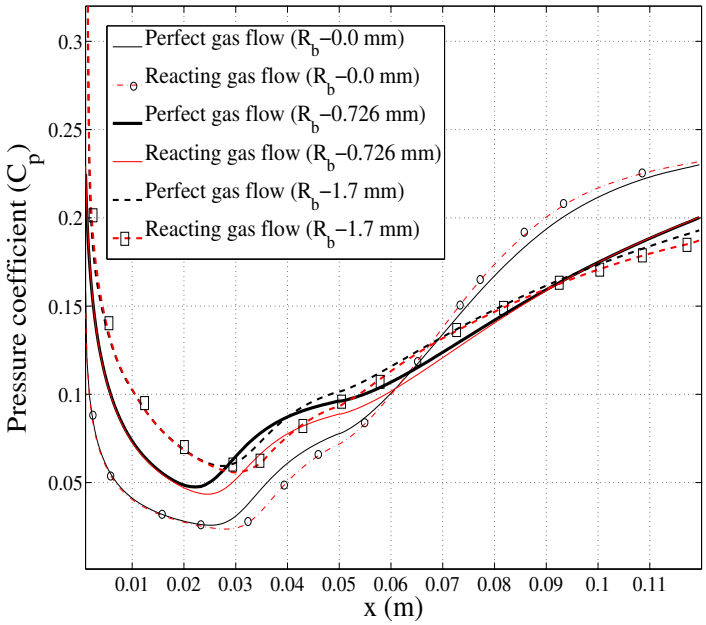

Figure 7.7: Surface pressure distribution for sample leading edge radii

of upstream influence location. Further, the thickness of boundary layer approaches the thickness of HEL around the upstream influence location for inversion radius. Matching of the boundary layer and HEL thickness at the reference upstream influence station has been reported as the indication for the leading edge radius to be the inversion radius in case of perfect gas flow [4]. But, the present studies reassert this truth for the reacting flow as well. Therefore, the indication of match of HEL and boundary layer thicknesses is noted to be the characteristic trait of inversion radius. It must be marked here that the inversion radius is slightly lower for real gas flow than the perfect gas flow. Lower shock stand-off distance in case of reacting flow is accounted for this observation.

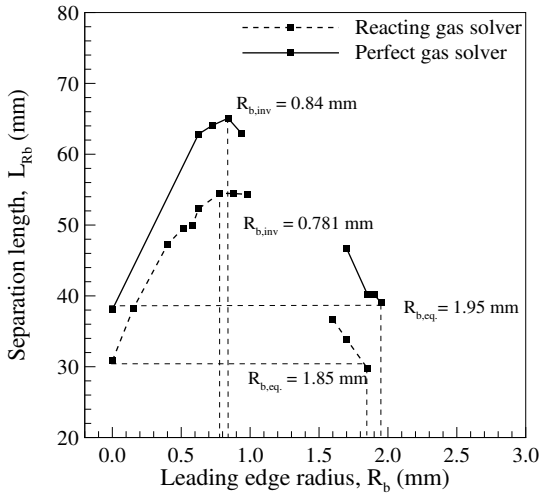

Figure 7.8: Separation bubble length for different leading edge radius

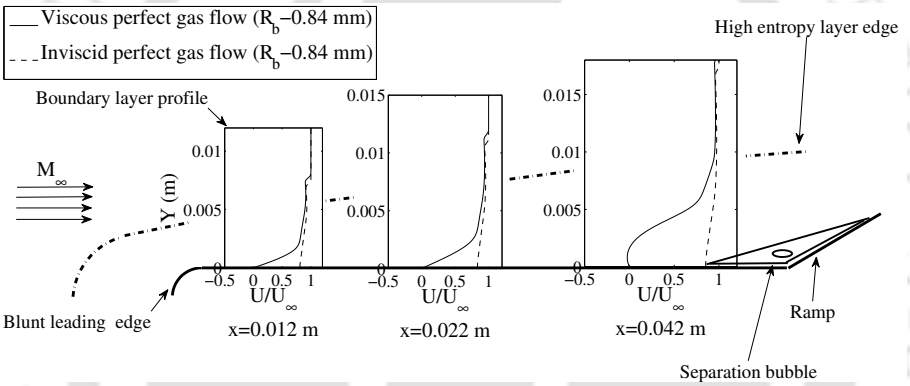

Figure 7.9: Variation of boundary layer and entropy layer thickness at three different locations for perfect gas flow with inversion radius (upstream influence location-0.022 m)

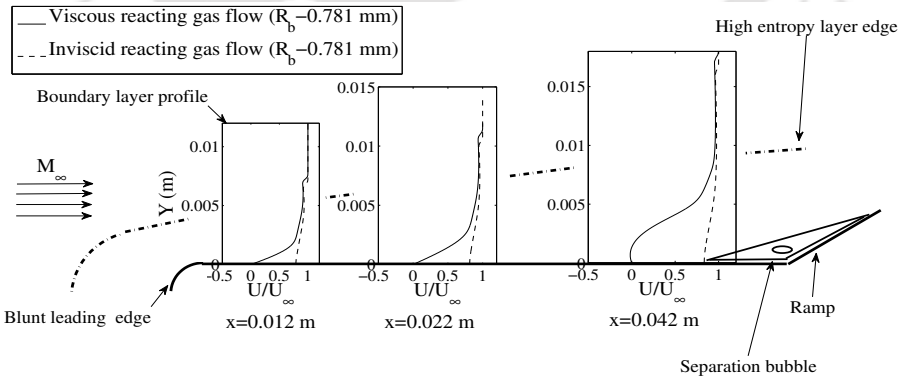

Figure 7.10: Variation of boundary layer and entropy layer thickness at three different locations for reacting flow with inversion radius (upstream influence location-0.022 m)

For radii, lower than the inversion radius, entropy layer is thinner (Figure 7.9 and Figure 7.10); therefore it leads to lower HEL thickness than the thickness of boundary

layer at the SWBLI station. But beyond the inversion radius, HEL remains thicker than the boundary layer around and upstream of SWBLI (Figure 7.11 and Figure 7.12). Such thicker HEL above the boundary layer remains a source for stream-wise vorticity as per Crocco's theorem. Further, every elemental increment in leading edge bluntness leads to thicker HEL. For any radius between inversion and equivalent radii, thick HEL does exist but its support is insufficient for reducing the separation since the surface pressure variation has small over pressure region. Blast wave theory (BTW) based prediction of wall pressure for different radii is shown in Figure 7.13(a) and (b). It is evident in this figure that the size of over pressure region or favorable pressure gradient increases with increase in leading edge bluntness. Difference in wall pressure variation is noted to be negligible for both the equivalent radii (1.85 mm and 1.95 mm). But, favorable pressure gradient for both the radii reaches the upstream influence location corresponding to the sharp leading edge case. Hence favorable pressure gradient provides the critical support to the thick HEL to equate the separation length as that of sharp leading edge case. Besides, small difference in reference separation sizes is expected to have the marginal difference in corresponding equivalent radius. But the need of favorable pressure gradient at the reference upstream influence location remains a valid judgment to choose leading edge bluntness as equivalent radius for perfect as well as reacting flows.

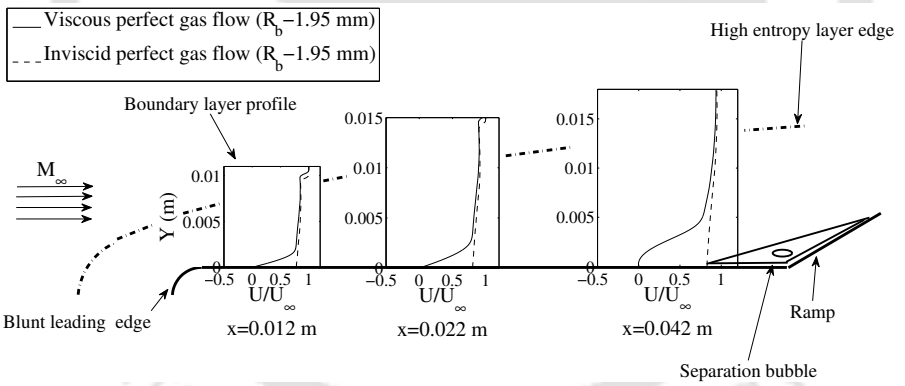

Figure 7.11: Variation of boundary layer and entropy layer thickness at three different locations for perfect gas flow with equivalent radius (upstream influence location-0.022 m)

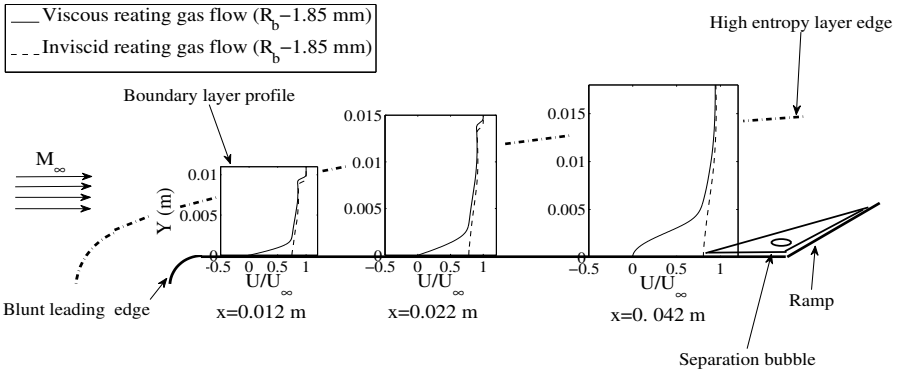

Figure 7.12: Variation of boundary layer and entropy layer thickness at three different locations for reacting flow with equivalent radius (upstream influence location-0.022 m)

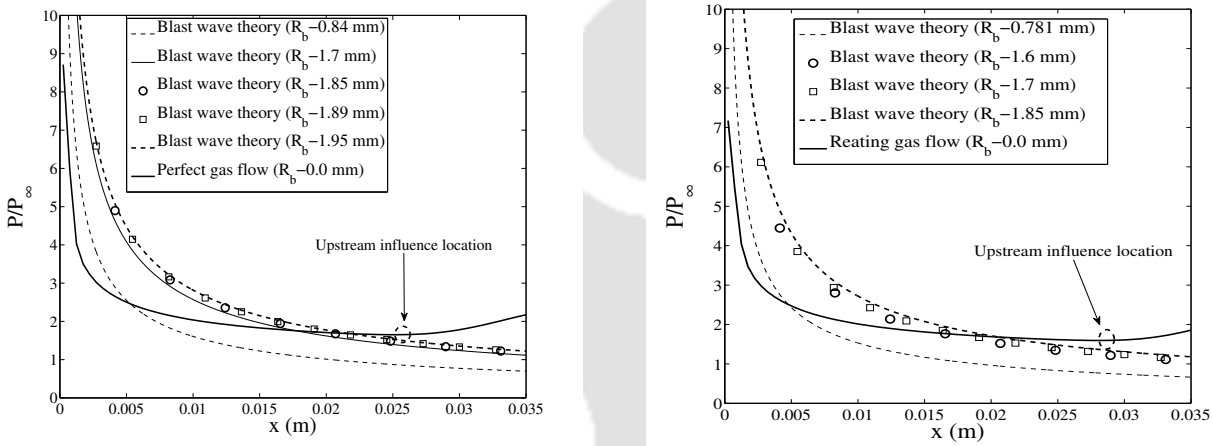

Figure 7.13: Comparison of surface pressure distribution from blast wave theory with (a) perfect gas flow (b) reacting flow

7.5 Conclusions

Shock wave boundary layer interaction control using leading edge bluntness is investigated herein for prediction of two critical radii through optimization process. Further, an optimization strategy has been developed to integrate the gradient based optimization technique and the in-house developed CFD solvers for perfect and reacting gas flows. As an outcome of this integration, inversion and equivalent radii for perfect gas flow are found to be 0.84 mm and 1.85 mm while the same for reacting flow accounting real gas effects are noted to be 0.781 mm and 1.95 mm. Real gas effects are initially accounted for decrement in separation size and then for the lowered requirement of leading edge bluntness for separation control. Further, the trait of inversion radius to have thicker high entropy layer around the upstream influence location than the local boundary layer thickness is marked to be necessary for perfect as well as reacting gas flow situation.

Other valuable remark is about the equivalent radius; it is worth to note that streamwise favorable pressure gradient in conjunction with thick HEL is highly desirable to reduce the separation length for separation control. It has been noted that the real gas effects reduce the extent of separation due to SWBLI in comparison with perfect gas flow. Thus, reduced requirement of high entropy layer thickness and upstream over pressure region lead to need of lower value of critical radii of bluntness for reacting flow conditions. Present investigations also revealed that the special gas dynamic features at the critical radii are independent type of gas flow. Further, the critical radii predicted for perfect gas flow would have same functionality in reacting flow situation as well. Thus only perfect gas simulations are sufficient to predict the critical radii to ensure separation control.

CHAPTER 8

CONCLUSIONS AND FUTURE WORKS

8.1 Conclusions

The present thesis work focuses on the numerical investigation of drag reduction techniques, high temperature effects and mitigation of boundary layer separation provoked by ramp-induced SWBLI. Therefore, a cell-centred the finite volume based multi species laminar unstructured coupled Navier-Stokes and species continuity equations solver has been developed to simulate these hypersonic flow concerns. Initially, the in-house developed solver is validated for the variety of literature reported problems including 2-D flow past a cylinder, 2-D axisymmetry flow over a sphere, unsteady shock tube flows, counter jet drag reduction, R-SWBLI etc. Later on, the solver has been employed for the detailed investigations of low to high enthalpy flow simulations. Additionally, perfect and frozen versions of solver have also been wielded to highlight the role of real gas effects in flowfield alteration as well as to simulate low enthalpy flowfield. The major outcomes of the present investigations are as follows:-

- **Delusive influence of non-dimensional numbers in canonical hypersonic non-equilibrium flows**
  Numerical assessment of reacting gas flows demonstrate the uncertainty involved with the conventional non-dimensional numbers in deciding the flow characteristics for different cases. In unsteady shock tube case, the absolute pressures in the driver and driven sections (ratio being constant) are found to influence the wave propagation speed. Similarly, in case of cylinders and spheres, the shock shape and shock stand-off distance are observed to be sensitive to the freestream enthalpy instead of Mach number alone. However, in perfect gas flows, these non-dimensional numbers (pressure ratio and Mach number) are known to govern the flow features

of mentioned test cases. Further, four convective flux computation schemes, viz. AUSM, Vanleer, Rusanov and AUSM+, with suitable modifications are successfully incorporated to compute high enthalpy test cases. Here, the diffusive nature of extended Rusanov scheme is also exposed for high enthalpy flows.

- **Aerothermodynamic considerations for energy deposition based drag reduction technique**
  The drag reduction approach using energy deposition has been analysed for perfect gas, frozen and reacting flow models. The performance of this technique has been assessed at various energy strength and intensity as well as for different freestream stagnation enthalpies. Here, the perfect gas model is observed to provide more power effectiveness whereas real gas effects restrict the performance output of frozen and reacting flows. In the investigation, it is also marked that the higher energy intensities lead to more drag reduction and differential prediction of power effectiveness for all gas models. Further, at higher enthalpies, reacting gas flow model show the reduction in power effectiveness due to the dominance of real gas effects compared to perfect gas flows. It is also observed that the absolute critical energy deposited to obtain maximum power effectiveness is independent of gas models. Moreover, the peak power effectiveness attained at different stagnation enthalpies is obtained in a narrow range of non-dimensional energy deposition.

- **Understanding the dynamics of counter jet drag reduction technique**
  Investigations are performed to find out the governing parameter of the counter jet based drag reduction technique. In order to achieve this objective, different influencing parameters are reviewed at various conditions. The limitation of these parameters in predicting all the flow features of the counter jet based drag reduction technique are revealed. Therefore a new non-dimensional number (jet to freestream momentum ratio) is introduced which is also examined by performing theoretical as well as numerical studies. It is observed that the jet to freestream momentum ratio is the vital parameter of the counter jet based drag reduction technique which also governs the aerodynamic features like shock stand-off distance, Mach disk diameter, Mach disk location, free stagnation point location, drag coefficient etc.

- **Separation mitigation using pressure feedback technique for hypersonic shock wave boundary layer interaction**
  Further, numerical investigations have been performed to mitigate the R-SWBLI induced separation using pressure feedback channel. It is observed that the performance of PFT can be enhanced significantly by cooling the feedback channel. Moreover, the performance degradation of PFT is noted at higher ramp angle cases

in spite of higher mass flow rate through it. Studies with the same wall to freestream total temperature at different enthalpies revealed that percentage separation reduction increases with the increment in enthalpy using cooled PFT. Simulation with integrated PFT and blunt leading edge techniques show enhancement in separation controllability. It is also observed that this arrangement reduces the inversion and equivalent radius values at same freestream condition without disturbing the boundary layer and entropy layer interaction.

- **Probing real gas and leading edge effects on flow separation in hypersonic flows via optimization and high fidelity computations**
  The blunt leading edge flow separation control technique has also been reviewed in presence of real gas effects. In order to do an accurate calculation of the inversion and equivalent radius, gradient based optimization technique is integrated with the CFD solver. It is noted that real gas effects are responsible for the less separation size and lowering the critical radii. Further, the requirement of thicker entropy layer in comparison with boundary layer thickness at upstream influence location is noted to be valid for perfect and reacting flows. On the other hand, the need of prolonged over-pressure region along with thicker high entropy layer edge to reduce the separation size is found to be reduced by real gas effects. Thus, critical radii prediction can be done with only perfect gas simulations to guarantee the lower separation size.

8.2 Future work

Although the present work provides the useful insight into various aspects of hypersonic flow, still there are few gaps which need to be filled. Some of the directions required to explore are as follows:-

- The present work is limited to the steady state investigation of R-SWBLI and counter jet drag reduction technique. However, the presence of turbulence may lead to unsteadiness in the flowfield. Therefore, in future studies, incorporation of turbulent models into the present solver could be of great significance to investigate the various unsteady phenomenon.

- The present solver can simulate 2-D axisymmetry flows efficiently. Its capability can be enhanced with the extension of the solver for the 3-D domain. This would make convenient to investigate various 3-D aspects in hypersonic flows.

- The SWBLI induced separation control strategies involve the use of pressure feedback channel in the present work. Efforts can be extended to assess its performance

at different injection angles, injection/suction locations, feedback channel width etc. which may help to enhance its controllability. Further, the effectiveness of energy deposition techniques must also be examined in the separation control. This active technique can be integrated with the other passive separation reduction strategies to improve the overall performance.

- In the study of high enthalpy flows, only chemical equilibrium/non-equilibrium is considered. Addition of thermal non-equilibrium would be helpful to obtain more detailed and precise results of high enthalpy flows.

- Present work considers the use of energy deposition and counter jet for drag reduction in high-speed flows. The performance of energy deposition technique is strongly dependent upon the various parameters like energy source strength, location and size. Therefore, optimization studies can be done in order to obtain the maximum power effectiveness along with the minimum drag using energy deposition. Further, the proposed universal governing parameter (momentum ratio) for counter jet injection is assessed in low enthalpy supersonic flows only and thus, it is required to test its validity in the high enthalpy flows as well. Apart from these, there are many other drag reduction techniques like hot gas injection, structural spike, forward facing step etc are found in the literature. The combinatorial approach of these techniques must be examined in order to obtain maximum drag reduction in presence of the hypersonic stream.

Publications

Journals

1. **Desai, S.**, Prakash, V., Gadgil, H., Kulkarni, V., "Momentum ratio as a scaling parameter for counter jet drag mitigation technique in supersonic flows", *(Under Review).*
2. **Desai, S.**, Brahmachary, S., Gadgil, H., Kulkarni, V., "Probing real gas and leading edge effects on flow separation in hypersonic flows via optimization and high fidelity computations", *(Under Review).*
3. **Desai, S.**, Kulkarni, V., Gadgil, H., 2018, "Separation mitigation using pressure feedback technique for hypersonic shock wave boundary layer interaction", ***The Proceedings of the Institution of Mechanical Engineers, Part G: Journal of Aerospace Engineering***, *(Accepted).*
4. **Desai, S.**, Kulkarni, V., Gadgil, H. and John, B., 2017, "Aerothermodynamics considerations for energy deposition based drag reduction technique", ***Applied Thermal Engineering***, vol. 122, pp. 451-460.
5. Agarwal, S., Sahoo, N., Irimpan, K.J., Menezes, V. and **Desai, S.**, 2017, "Comparative performance assessments of surface junction probes for stagnation heat flux estimation in a hypersonic shock tunnel", ***International Journal of Heat and Mass Transfer***, vol. 114, pp. 748-757.
6. **Desai, S.**, Kulkarni, V., Gadgil, H., 2016, "Delusive influence of non-dimensional number in canonical hypersonic non-equilibrium flows", ***Journal of Aerospace Engineering***, vol. 25, 04016030.

Conferences

1. Vanarase, P., **Desai, S.**, Gadgil H., and Kulkarni, V., 2017, "Numerical study of real gas effects in external hypersonic flow for mars environment", Paper No: IHMTC2017-01-1143, ***Proceedings of the 24th National and 2nd International ISHMT-ASTFE Heat and Mass Transfer Conference***, BITS-Pilani, Hyderabad, India.
2. Prakash, V., **Desai, S.**, Gadgil, H. and Kulkarni, V., 2017, "Dynamics of counterflow injection for wave drag reduction", Paper No: IHMTC2017-14-1233, ***Proceedings of the 24th National and 2nd International ISHMT-ASTFE Heat and Mass Transfer Conference***, BITS-Pilani, Hyderabad, India
3. **Desai, S.**, Kulkarni, V.and Gagdil, H., 2016, "High enthalpy simulations for shock wave boundary layer interaction", ***6th International Congress on Computational Mechanics and Simulations***, IIT Bombay, Mumbai, India.
4. **Desai, S.**, Gagdil, H. and Kulkarni, V., 2016, "Consideration of high temperature effect for bench mark test cases in supersonic/hypersonic aerodynamics", ***4th National Symposium on Shock Waves***, Karunya Institute of Technology and Science, Coimbatore, India
5. **Desai, S.**, Kulkarni, V.and Gagdil, H., 2015, "Shock wave boundary layer interaction with real gas effects", ***Conference on Computational PDE***, TIFR-CAM, Bangalore, India.

APPENDIX

Table A: Formulations of different flux computation schemes with suitable modifications

Scheme	**Flux formula**	**Terms**
	Interface flux, $H_{I_\perp} = {H_I}^+ + {H_I}^-$	$${M_L}^+ = \begin{cases} M_L, & \text{if, } M_L \geq 1 \\ \frac{1}{4}(M_L+1)^2 & \text{if, } \lvert M_L \rvert < 1 \\ 0 & \text{if, } M_L \leq -1 \end{cases}$$
Van-Leer	${H_I}^+ = H_{I_\perp},\ {H_I}^- = 0$ if, $M_\perp \geq 1$	
FVM	${H_I}^- = H_{I_\perp},\ {H_I}^+ = 0$ if, $M_\perp \geq -1$	
Van Leer B [1]	$H_{I\perp} = H_I^+ + {H_I}^-$ if, $-1 < M_\perp < 1$	

Continued on next page

Table A – *Continued from previous page*

Scheme	Flux formula	Terms
Van-Leer FVM Van Leer B [1]	$H_{I_\perp} = \begin{bmatrix} \rho u_\perp \\ \rho u u_\perp + p n_x \\ \rho v u_\perp + p n_y \\ (\rho e + p) u_\perp \\ C_i u_\perp \end{bmatrix}$ i=1,2,...,N-1 if $\lvert M_\perp \rvert < 1$ $H_I^\pm = \begin{bmatrix} {f_{mass}}^\pm \\ {f_{mass}}^\pm \left[u + n_x \left(-u_\perp \pm 2a \right) \frac{p}{\rho a^2} \right] \\ {f_{mass}}^\pm \left[v + n_y \left(-u_\perp \pm 2a \right) \frac{p}{\rho a^2} \right] \\ {f_{mass}}^\pm \left[H + m \left(-u_\perp \pm a \right)^2 \right] \\ {f_{mass}}^\pm C_i / \rho] \end{bmatrix}$	$M_R{}^- = \begin{cases} 0 & \text{if, } M_R \geq 1 \\ \frac{1}{4}(M_R + 1)^2 & \text{if, } \lvert M_R \rvert < 1 \\ M_R & \text{if, } M_R \leq -1 \end{cases}$ $M_{\perp L} = \frac{u_{\perp L}}{a_L}, \quad M_{\perp R} = \frac{u_{\perp R}}{a_R}$ $f^+_{mass} = +\rho_L a_L \frac{(M_L + 1)^2}{4}$ $f^-_{mass} = -\rho_R a_R \frac{(M_R - 1)^2}{4}$ $m = \frac{h}{a^2 + 2h}$ h is specific enthalpy and H is total enthalpy.

Continued on next page

Table A – *Continued from previous page*

Scheme	Flux formula	Terms
AUSM-delta Hybrid	Interface flux, $H_{I_\perp} = (M_n)_{I+\frac{1}{2}} \begin{bmatrix} \rho a \\ \rho a u \\ \rho a v \\ (\rho e + p) a \\ C_i a \end{bmatrix}_{L/R} + \begin{bmatrix} 0 \\ p n_x \\ p n_y \\ 0 \\ 0 \end{bmatrix}_{I+\frac{1}{2}}$ where $(M_n)_{I+\frac{1}{2}} = {M_L}^+ + {M_R}^-$ $(p)_{I+\frac{1}{2}} = {p_L}^+ + {p_R}^-$ $(M_n)_{I+\frac{1}{2}} = {M_L}^+ + {M_R}^-$ $(\cdot)_{L/R} = \begin{cases} (\cdot)_L & \text{if, } M_{n_{I+\frac{1}{2}}} \geq 0 \\ (\cdot)_R & Otherwise \end{cases}$ Interface flux,	$p_L^+ = \begin{cases} p_L & \text{if, } M_L \geq +1 \\ \frac{p_L}{4}(M_L+1)^2(2-M_L) & \text{if, } \lvert M_L \rvert < 1 \\ 0 & \text{if, } M_L \leq -1 \end{cases}$ $p_R^- = \begin{cases} 0 & \text{if, } M_R \geq +1 \\ \frac{p_R}{4}(M_R-1)^2(2+M_R) & \text{if, } \lvert M_R \rvert < 1 \\ p_R & \text{if, } M_R \leq -1 \end{cases}$ To avoid zero advection Mach number $(M_n)_{I+\frac{1}{2}}$ is modified in AUSM-delta as, $\lvert M_{n_{I+\frac{1}{2}}} \rvert = \begin{cases} \lvert M_{n_{I+\frac{1}{2}}} \rvert & \text{if, } \lvert M_{n_{I+\frac{1}{2}}} \rvert > \delta \\ \frac{{M_{n_{I+\frac{1}{2}}}}^2 + \delta^2}{2\delta} & \text{if, } \lvert M_{n_{I+\frac{1}{2}}} \rvert \leq \delta \end{cases}$

Continued on next page

Table A – *Continued from previous page*

Scheme	Flux formula	Terms
AUSM + Hybrid	$H_{I_\perp} = m_{I+\frac{1}{2}}{}^{+}(a)_{I+\frac{1}{2}} \begin{bmatrix} \rho a \\ \rho a u \\ \rho a v \\ (\rho e + p)a \\ C_i a \end{bmatrix}_L$	$M^{\pm}_{L/R} = \begin{cases} \frac{1}{2}\left(M_{L/R} \pm +\lvert M_{L/R}\rvert\right) & \text{if, } \lvert M_{L/R} > 1 \\ \pm\frac{1}{2}\left(M_{L/R} \pm 1\right)^2 \pm \beta\left({M_{L/R}}^2 - 1\right)^2 & \\ & \text{Otherwise} \end{cases}$
	$+m_{I+\frac{1}{2}}{}^{-}(a)_{I+\frac{1}{2}} \begin{bmatrix} \rho a \\ \rho a u \\ \rho a v \\ (\rho e + p)a \\ C_i a \end{bmatrix}_R + \begin{bmatrix} 0 \\ p n_x \\ p n_y \\ 0 \\ 0 \end{bmatrix}_{I+\frac{1}{2}}$	where, $-\frac{1}{6} \le \beta \le \frac{1}{2}$
	$m_{I+\frac{1}{2}} = {M_L}^{+} + {M_R}^{-} \qquad a_{I+\frac{1}{2}} = \sqrt{a_L a_R}$	$p_{I+\frac{1}{2}} = {p_L}^{+} + {p_R}^{-}$
	$m^{\pm}_{I+\frac{1}{2}} = \frac{1}{2}\left(m_{I+\frac{1}{2}} + \lvert m_{I+\frac{1}{2}}\rvert\right)$	$p_{L/R} = \begin{cases} \frac{1}{2}\left(1 \pm sign(M_{L/R})\right) & \text{if, } \lvert M_{L/R} \ge 1 \\ \frac{1}{4}\left(M_{L/R} \pm 1\right)^2\left(2 \mp M_{L/R}\right) \pm \alpha M_{L/R} & \\ \quad \times \left(M^2_{L/R} - 1\right)^2 & \text{Otherwise} \end{cases}$
		where $-\frac{2}{4} \le \alpha \le \frac{3}{16}$
	Interface flux, $H_{I_\perp} = \frac{1}{2}(H_{I_L} + H_{I_R}) - \frac{1}{2}S^{+}(U_R - U_L)$	$S^{+} = max\left(V_L + S_L, V_L - S_L, S_L, V_R + S_R V_R - S_R, S_R\right)$

Continued on next page

Table A – *Continued from previous page*

Scheme	**Flux formula**	**Terms**
Rusanov FDM	$H_{L/R} = \begin{bmatrix} \rho u_\perp \\ \rho u u_\perp + p n_x \\ \rho v u_\perp + p n_y \\ (\rho e + p) u_\perp \\ C_i u_\perp \end{bmatrix}_{L/R}$	S_L and S_R can be calculated either from equation given below or can be approximated as corresponding sonic velocity at left and right of the face $S = \sqrt{{\lambda_0}^2 + \beta},\ \lambda_0 = u n_x + v n_y$ β = pseudo-compressibility parameter

REFERENCES

[1] J. S. Shuen, M. S. Liou, B. V. Leer, Inviscid flux-splitting algorithms for real gases with non-equilibrium chemistry, Journal of Computational Physics 90 (1990) 371–395.

[2] R. Joarder, Demonstration of supersonic combustion in a combustion driven shock-tunnel, PhD thesis, Indian Institute of Science Bangalore, 2009.

[3] F. Billig, Shock-wave shapes around spherical and cylindrical nosed bodies, Journal of Spacecraft and Rockets 4 (6) (1967) 822–823.

[4] B. John, V. Kulkarni, Effect of leading edge bluntness on the interaction of ramp induced shock wave with laminar boundary layer at hypersonic speed, Computers and Fluids 96 (2014) 177–190.

[5] R. K. Lobb, Chapter 26 - experimental measurement of shock detachment distance on spheres fired in air at hypervelocities, in: The High Temperature Aspects of Hypersonic Flow, Vol. 68 of AGARDograph, Elsevier, 1964, pp. 519 – 527.

[6] P. H. Rose, J. O. Stankevic, Stagnation-point heat-transfer measurements in partially ionized air, AIAA Journal 1 (12) (1963) 2752 – 2763.

[7] H. G. Hornung, Non-equilibrium dissociating nitrogen flow over spheres and circular cylinders, Journal of Fluid Mechanics 53 (1) (1972) 149–176.

[8] D. J. Kewley, H. G. Hornung, Non-equilibrium dissociating nitrogen flow over a wedge, Journal of Fluid Mechanics 64 (4) (1974) 725–736.

[9] P. Subrahmanyam, Development of an interactive hypersonic flow solver framework for aerothermodynamic analysis, Engineering Applications of Computational Fluid Mechanics 2 (4) (2008) 436–455.

[10] A. Viviani, G. Pezzella, Nonequilibrium aerothermodynamics for a capsule reentry vehicle, Engineering Applications of Computational Fluid Mechanics 3 (4) (2009) 543–561.

[11] B. Grossman, P. Cinnela, Flux-split algorithms for flows with nonequilibrium chemistry and vibrational relaxation, Journal of Computational Physics 88 (1990) 131–168.

[12] G. Tchuen, Y. Burtschell, D. E. Zeitoun, Computation of non-equilibrium hypersonic flow with artificially upstream flux vector splitting (AUFS) schemes, International Journal of Computational Fluid Dynamics 22 (4) (2008) 209–220.

[13] J. N. Moss, G. A. Bird, Direct simulation of transitional flow for hypersonic reentry conditions, Journal of Spacecraft and Rockets 40 (5) (2003) 830–843.

[14] G. V. Candler, I. D. Boyd, D. A. Levin, S. Moreau, P. W. Erdman, Continuum and dsmc analysis of bow shock flight experiments, 31st Aerospace Sciences Meeting Exhibit, Reno NV, 1993.

[15] J. S. Shuen, Effects of chemistry in nonequilibrium hypersonic flow around blunt bodies, Journal of Computational Physics 99 (1992) 233–250.

[16] R. N. Gupta, J. M. Yos, R. A. Thompson, K. Lee, A review of reaction rates and thermodynamic and transport properties for an 11-species air model for chemical and thermal nonequilibrium calculations to 30000 K, NASA RP-1232, 1990.

[17] S. Gordon, B. J. McBride, Computer program for calculation of complex chemical equilibrium composition and applications, NASA RP-1311, 1994.

[18] S.-T. Yu, B. J. McBride, K.-C. Hsieh, J.-S. Shuen, A chemical equilibrium method for hypersonic flow simulations, Computers Fluids 23 (1) (1994) 143 – 155.

[19] K. Sawada, E. Dendou, Validation of hypersonic chemical equilibrium flow calculations using ballistic-range data, Shock Waves 11 (1) (2001) 43–51.

[20] C. A. R. Pimentel, A. Hetem Jr., Computation of air chemical equilibrium composition until 30000 K - part i, Journal of Aerospace Technology and Management 3 (2) (2011) 111–126.

[21] C. Wen, H. G. Hornung, Non-equilibrium dissociating flow over spheres, Journal of Fluid Mechanics 299 (1995) 389–405.

[22] H. Olivier, A theoretical model for the shock stand-off distance in frozen and equilibrium flows, Journal of Fluid Mechanics 413 (2000) 345–353.

[23] N. Belouaggadia, H. Olivier, R. Brun, Numerical and theoretical study of the shock stand-off distance in non-equilibrium flows, Journal of Fluid Mechanics 607 (2008) 167–197.

[24] M. G. Dunn, S. W. Kang, Theoretical and experimental studies of reentry plasmas, NASA CR, No.2232, 1973.

[25] J. L. Shinn, J. N. Moss, A. L. Simmonds, Viscous-shock-layer heating analysis for the shuttle windward-symmetry plane with surface finite catalytic recombination rates, 3rd Joint Thermophysics, Fluids, Plasma and Heat Transfer Conference, St. Louis, MO, U.S.A., 1982.

[26] C. Park, Assessment of a two temperature kinetic model for dissociating and weakly ionizing nitrogen, Journal of Thermophysics and Heat Transfer 2 (1) (1987) 8–16.

[27] C. Park, Review of chemical-kinetic problems of future nasa mission, i: Earth entries, Journal of Thermophysics and Heat Transfer 7 (3) (1993) 385–398.

[28] C. Park, R. L. Jaffe, H. Partridge, Chemical-kinetic parameters of hyperbolic earth entry, Journal of Thermophysics and Heat Transfer 15 (1) (2001) 76–90.

[29] G. Tchuen, D. E. Zeitoun, Effects of chemistry in nonequilibrium hypersonic flow around blunt bodies, Journal of Thermophysics and Heat Transfer 23 (3) (2009) 433–442.

[30] X. Wang, C. Yan, Y. Zheng, E. Li, Assessment of chemical kinetic models on hypersonic flow heat transfer, International Journal of Heat and Mass Transfer 111 (2017) 356 – 366.

[31] B. Hassan, G. V. Candler, D. R. Olynick, Thermo-chemical nonequilibrium effects on the aerothermodynamics of aerobraking vehicles, Journal of Spacecraft and Rockets 30 (6) (1993) 647 – 655.

[32] S. G. Mallinson, S. L. Gai, N. R. Mudford, The boundary layer on a flat plate in hypervelocity flow, The Aeronautical Journal 100 (994) (1996) 135–141.

[33] S. G. Mallinson, S. L. Gai, N. R. Mudford, High-enthalpy, hypersonic compression corner flow, AIAA Journal 34 (6) (1996) 1130–1137.

[34] F. Grasso, M. Marini, G. Ranuzzi, S. Cuttica, S. Doraiswamy, B. Chanetz, Shock-wave/turbulent boundary-layer interactions in nonequilibrium flows, AIAA Journal 39 (11) (2001) 2131 – 2140.

[35] P. Sagnier, J.-L. Vérant, On the validation of high enthalpy wind tunnel simulations, Aerospace Science and Technology 2 (7) (1998) 425 – 437.

[36] S. Nonaka, H. Mizuno, K. Takayama, Ballistic range measurement of shock shapes in intermediate hypersonic regime, 37th Aerospace Sciences Meeting and Exhibit, Reno, NV, U.S.A., 1999.

[37] D. D. Knight, Y. F. Kolesnichenko, V. Brovkin, D. Khmara, High speed flow control using microwave energy deposition, 16th Australasian Fluid Mechanics Conference Crown Plaza, Gold Coast, Australia, 2007.

[38] Z. Xiao-yuan, Q. Li-zi, L. Yu, Numerical study of chemical non-equilibrium flow in hydrocarbon scramjet nozzle, Proceedings of International Conference on Mechanical Engineering and Material Science, 2012.

[39] M. Ajith, L. A. Pillai, K. Dileep, N. Sreenivas, Chemical non-equilibrium flow simulation of plasma wind tunnel test of hsp crew module, Applied Thermal Engineering 111 (2017) 1603 – 1610.

[40] I. D. Boyd, Modeling of associative ionization reactions in hypersonic rarefied flows, Physics of Fluids 19 (9) (2007) 096102.

[41] R. D. Braun, R. M. Manning, Mars exploration entry, descent, and landing challenges, Journal of Spacecraft and Rockets 44 (2) (2007) 310–323.

[42] H. Fei, J. Xu-hong, L. Jun-ming, C. Xiao-li, Impact of martian atmosphere parameter uncertainties on entry vehicles aerodynamic for hypersonic rarefied conditions, AIP Conference Proceedings 1786 (1) (2016) 190006.

[43] G. Candler, Computation of thermo-chemical nonequilibrium martian atmospheric entry flows, AIAA/ASME 5th Joint Thermophysics and Heat Transfer Conference, Seattle, WA, U.S.A., 1990.

[44] R. A. Mitcheltree, P. A. Gnoffo, Wake flow about a mesur mars entry vehicle, 6th Joint Thermophysics and Heat Transfer Conference, Fluid Dynamics and Co-located Conferences, Colorado Springs, CO, U.S.A., 1994.

[45] M. Sharma, A. B. Swantek, W. Flaherty, J. M. Austin, S. Doraiswamy, G. V. Candler, Experimental and numerical investigations of hypervelocity carbon dioxide

flow over blunt bodies, Journal of Thermophysics and Heat Transfer 24 (2010) 673 – 683.

[46] J. Hao, J. Wang, Z. Gao, C. Jiang, C. Lee, Comparison of transport properties models for numerical simulations of mars entry vehicles, Acta Astronautica 130 (2017) 24 – 33.

[47] W. E. Moeckel, Flow separation ahead of blunt bodies at supersonic speeds, NASA TN-2418, 1951.

[48] D. S. Miller, H. W. Carlson, A study of application of heat or force fields to the sonic boom minimization problem, NASA TN-5582, 1969.

[49] L. N. Myrabo, Y. P. Raizer, Laser-induced air spike for advanced transatmospheric vehicles, 25th AIAA Plasmadynamics and Lasers Conference Colorado Springs, U.S.A., 1994.

[50] S. O. Macheret, M. N. Shneider, R. B. Miles, Scramjet inlet control by off-body energy addition: A virtual cowl, 41st AIAA Aerospace Sciences Meeting and Exhibit, Nevada, 2003.

[51] D. Riggins, H. F. Nelson, E. Johnson, Blunt body wave drag reduction using focused energy deposition, AIAA Journal 37 (4) (1999) 460–504.

[52] V. A. Levin, V. G. Gromov, N. E. Afonina, Numerical analysis of the effect of local energy supply on the aerodynamic drag and heat transfer of a spherically blunted body in a supersonic air flow, Journal of Applied Mechanics and Technical Physics 41 (5) (2000) 915–922.

[53] A. A. Zheltovodov, E. A. Pimonov, D. D. Knight, Effect of concentrated energy deposition on the aerodynamic drag of a blunt body in hypersonic flow, 45th AIAA Aerospace Sciences Meeting and Exhibit, Reno, Nevada, 2007.

[54] V. A. Lashkov, I. C. Mashek, I. Y. Anisimov, V. I. Ivanov, Gas dynamic effect of microwave discharge on supersonic cone-shaped bodies, 42nd AIAA Aerospace Sciences Meeting and Exhibit, Reno, Nevada, 2004.

[55] C. S. Hartley, T. W. Portwood, M. V. Filippelli, L. N. Myrabo, H. T. Nagamatsu, M. N. Shneider, Y. P. Razier, Experimental and computational investigation of drag reduction by electricarc airspikes at Mach 10, AIP Conference Proceedings 766 (1) (2005) 499–513.

[56] K. Kremeyer, K. Sebastian, C. Shu, Computational study of shock mitigation and drag reduction by pulsed energy lines, AIAA Journal 44 (6) (2006) 1720–1730.

[57] K. Satheesh, G. Jagadeesh, Effect of concentrated energy deposition on the aerodynamic drag of a blunt body in hypersonic flow, Physics of Fluids 19 (031701) (2007) 1–4.

[58] V. Kulkarni, G. M. Hegde, G. Jagadeesh, E. Arunan, K. P. J. Reddy, Aerodynamic drag reduction by heat addition into the shock layer for a large angle blunt cone in hypersonic flow, Physics of Fluids 20 (081703) (2008) 1–4.

[59] Y. Ogino, N. Ohnishi, S. Taguchi, K. Sawada, Baroclinic vortex influence on wave drag reduction induced by pulse energy deposition, Physics of Fluids 21 (066102) (2009) 1–11.

[60] A. Markhotok, A mechanism of wave drag reduction in the thermal energy deposition experiments, Physics of Plasmas 22 (6) (2015) 063512.

[61] M. A. Ganesh, B. John, Concentrated energy addition for active drag reduction in hypersonic flow regime, Acta Astronautica 142 (2018) 221 – 231.

[62] D. R. Gutiérrez, J. Poggie, Effects of power deposition on the aerodynamic forces on a slender body, AIAA Journal (Article in Advance).

[63] H. M. MacMahon, An experimental study of the effect of mass ejection at the stagnation point of a blunt body, California Institute of Technology Guggenheim Aeronautial Laboratory Hypersonic Research Project Memorandum-42, 1958.

[64] C. H. E. Warren, An experimental investigation of the effect of ejecting a coolant gas at the nose of a bluff body, Journal of Fluid Mechanics 8 (1960) 400–417.

[65] P. J. Finley, The flow of a jet from a body opposing a supersonic free stream, Journal of Fluid Mechanics 26 (2) (1966) 337–368.

[66] F. O. Jarvinen, R. H. Adams, The effects of retrorockets on the aerodynamic characteristics of conical aerbshell planetary entry vehicles, 8th Aerospace Sciences Meeting, Aerospace Sciences Meetings, New York, 1970.

[67] K. Hayashi, S. Aso, Effect of pressure ratio on aerodynamic heating reduction due to opposing jet, 33rd AIAA Fluid Dynamics Conference and Exhibit, Orlando, Florida, 2003.

[68] Y. Y. Zheng, N. A. Ahmed, A novel means of dissipation of shock wave induced heat in a high speed flow, 43rd Fluid Dynamics Conference, Fluid Dynamics and Co-located Conferences, San Diego, CA, 2013.

[69] J. Fox, Counterflow sonic nosejet into a supersonic stream, 4th Applied Aerodynamics Conference, Fluid Dynamics and Co-located Conferences, San Diego, CA, U.S.A., 1986.

[70] M. Fujita, Axisymmetric oscillations of an opposing jet from a hemispherical nose, AIAA Journal 33 (10) (1995) 1850–1855.

[71] J. F. Debiéve, J. P. Ardissone, J. P. Dussauge, Shock motion and state of turbulence in a perturbed supersonic flow around a sphere, Journal of Turbulence 4 (2003) N26.

[72] L. W. Chen, G. L. Wang, X. Y. Lu, Numerical investigation of a jet from a blunt body opposing a supersonic flow, Journal of Fluid Mechanics 684 (2011) 85–110.

[73] B. Venukumar, G. Jagadeesh, K. P. J. Reddy, Counterflow drag reduction by supersonic jet for a blunt body in hypersonic flow, Physics of Fluids 18 (11) (2006) 118104.

[74] V. Kulkarni, K. P. J. Reddy, Enhancement in counterflow drag reduction by supersonic jet in high enthalpy flows, Physics of Fluids 20 (1) (2008) 016103.

[75] R. Yisheng, Drag reduction research in supersonic flow with opposing jet, Acta Astronautica 91 (Supplement C) (2013) 1 – 7.

[76] C. Zhou, W. Ji, A three-dimensional numerical investigation on drag reduction of a supersonic spherical body with an opposing jet, Proceedings of the Institution of Mechanical Engineers, Part G: Journal of Aerospace Engineering 228 (2) (2014) 163–177.

[77] S. bin Li, Z. guo Wang, W. Huang, J. Liu, Effect of the injector configuration for opposing jet on the drag and heat reduction, Aerospace Science and Technology 51 (2016) 78 – 86.

[78] S. bin Li, Z. guo Wang, W. Huang, J. Liu, Drag and heat reduction performance for an equal polygon opposing jet, Journal of Aerospace Engineering 30 (1) (2017) 04016065.

[79] A. Bibi, A. Maqsood, S. Sherbaz, L. Dala, Drag reduction of supersonic blunt bodies using opposing jet and nozzle geometric variations, Aerospace Science and Technology 69 (Supplement C) (2017) 244 – 256.

[80] N. Sahoo, V. Kulkarni, S. Saravanan, G. Jagadeesh, K. P. J. Reddy, Film cooling effectiveness on a large angle blunt cone flying at hypersonic speed, Physics of Fluids 17 (3) (2005) 036102.

[81] K. Hayashi, S. Aso, Y. Tani, Experimental study on thermal protection system by opposing jet in supersonic flow, Journal of Spacecraft and Rockets 43 (1) (2006) 233–235.

[82] B. Meyer, H. F. Nelson, D. W. Riggins, Hypersonic drag and heat-transfer reduction using a forward-facing jet, Journal of Spacecraft and Rockets 38 (4) (2001) 680–686.

[83] J. Stalder, H. V. Nielsen, Heat transfer from a hemisphere-cylinder equipped with flow separation on spikes, NASA TN-3287, 1955.

[84] D. J. Maull, Hypersonic flow over axially symmetric spiked bodies, Journal of Fluid Mechanics 8 (4) (1960) 584–592.

[85] V. Menezes, S. Saravanan, G. Jagadeesh, K. P. J. Reddy, Experimental investigations of hypersonic flow over highly blunted cones with aerospikes, AIAA Journal 41 (10) (2003) 1955–1966.

[86] J. S. Shang, Plasma injection for hypersonic blunt-body drag reduction, AIAA Journal 40 (6) (2002) 1178–1186.

[87] V. Menezes, S. Kumar, K. Maruta, K. Reddy, K. Takayama, Hypersonic flow over a multi-step afterbody, Shock Waves 14 (5/6) (2005) 421–424.

[88] Z. Jiang, Y. Liu, G. Han, W. Zhao, Experimental demonstration of a new concept of drag reduction and thermal protection for hypersonic vehicles, Acta Mechanica Sinica 25 (3) (2009) 417–419.

[89] M. B. Gerdroodbary, Numerical analysis on cooling performance of counterflowing jet over aerodisked blunt body, Shock Waves 24 (5) (2014) 537–543.

[90] X. Sun, W. Huang, Z. yun Guo, L. Yan, Multiobjective design optimization of hypersonic combinational novel cavity and opposing jet concept, Journal of Spacecrafts and Rockets (Article in Advance).

[91] Y. He, H. Yin, H. Huang, D. Yu, Numerical study on dynamic characteristics for sharp opening procedure of boundary-layer suction slot, Acta Astronautica 137 (Supplement C) (2017) 145 – 156.

[92] W. T. Hou, W. Y. Qiao, H. L. Luo, Shock-wave/boundary-layer interaction in a transonic turbine cascade, Proceedings of the Institution of Mechanical Engineers, Part G: Journal of Aerospace Engineering 225 (1) (2011) 77–85.

[93] D. Ono, T. Handa, M. Masuda, Three-dimensional normal shock-wave/boundary-layer interaction in a diffuser, ASME. Journal of Fluids Engineering 135 (4) (2013) 041105.

[94] H. A. Schreiber, H. Starken, An investigation of a strong shock-wave turbulent boundary layer interaction in a supersonic compressor cascade, ASME. Journal of Turbomachinery 114 (3) (1992) 494–503.

[95] M. J. Lighthill, On boundary layers and upstream influence. ii. supersonic flows without separation, Proceedings of the Royal Society, London A 217 (1953) 478–507.

[96] N. Curle, The effects of heat transfer on laminar-boundary-layer separation in supersonic flow, Aeronautical Quarterly 12 (4) (1961) 309–336.

[97] M. H. Bertram, T. A. Blackstock, Some simple solutions to the problem of predicting boundary-layer self-induced pressures, NASA TN D-798, 1961.

[98] J. Ackeret, F. Feldemann, N. Rott, Investigations of compression shocks and boundary layers in gasses moving at high speed, NACA TN-1113, 1947.

[99] K. Stewartson, On the interaction between shock waves and boundary layers, Proceedings of the Cambridge Philosophical Society 47 (1951) 545–553.

[100] G. E. Gadd, D. W. Holder, J. D. Regan, An experimental investigation of the interaction between shock waves and boundary layers, Proceedings of the Royal Society, London Ser. A226 (1954) 227–253.

[101] K. Stewartson, P. G. Williams, Self-induced separation, Proceedings of the Royal Society London A 312 23 (1969) 3181–206.

[102] D. R. Chapman, D. M. Kuehn, H. K. Larson, Investigation of separated flows in supersonic and subsonic streams with emphasis on the effect of transition, NACA TN-3869, 1957.

[103] R. J. Hakkinen, I. Greber, L. Trilling, S. S. Abarbanel, The interaction of an oblique shock wave with a laminar boundary layer, NASA Memo 2-18-59W, 1959.

[104] D. M. Kuehn, Experimental investigation of the pressure rise required for the incipient separation of turbulent boundary layers in two-dimensional supersonic flow, NASA Memo 1-21-59A, 1959.

[105] D. A. Needham, A heat-transfer criterion for the detection of incipient separation in hypersonic flow, AIAA Journal 3 (1965) 781–783.

[106] D. A. Needham, J. L. Stollery, Boundary-layer separation in hypersonic flow, AIAA paper (1966) 66–455.

[107] J. B. Anders, Wedge-induced laminar-boundary-layer separation on a flat plate in low-density, hypervelocity flow, NASA TN D-5791, 1970.

[108] G. M. Elfstrom, Turbulent hypersonic flow at a wedge-compression corner, Journal of Fluid Mechanics 53 (1) (1972) 113–127.

[109] F. T. Hung, D. O. Barnett, Shock wave boundary layer interference heating analysis, AIAA Paper (1973) 72–0327.

[110] J. E. Carter, Numerical solutions of the supersonic, laminar flow over a two-dimensional compression corner, Proceedings of the Third International Conference on Numerical Methods in Fluid Mechanics, 1973.

[111] R. MacCormack, B. Baldwin, A numerical method for solving the navier-stokes equations with application to shock-boundary layer interactions, 13th Aerospace Sciences Meeting Pasadena, CA, U.S.A., 1975.

[112] D. P. Rizzetta, O. R. Burggraf, R. Jenson, Triple-deck solutions for viscous supersonic and hypersonic flow past corners, Journal of Fluid Mechanics 89 (3) (1978) 535–552.

[113] C. M. Hung, R. W. MacCormack, Numerical solutions of supersonic and hypersonic laminar compression corner flows, AIAA Journal 14 (4) (1976) 475–481.

[114] J. C. L. Balleur, R. Peyret, H. Viviand, Numerical studies in high reynolds number aerodynamics, Computers and Fluids 8 (1980) 1–30.

[115] E. Katzer, On the lengthscales of laminar shock/boundary-layer interaction, Journal of Fluid Mechanics 206 (1989) 477–496.

[116] D. Rudy, J. L. Thomas, A. Kumar, P. A. Gnoffo, S. R. Chakravarthy, Computation of laminar hypersonic compression-corner flows, AIAA Journal 29 (7) (1991) 1108–1113.

[117] J. F. Fay, J. Sambamurthi, Laminar hypersonic flow over a compression corner using the hana code, AlAA 27th Thermophysics Conference Nashville, TN , 1992.

[118] F. Grasso, G. Leone, J. M. Delery, Validation procedure for the analysis of shock-wave/boundary-layer interaction problems, AIAA Journal 32 (1994) 1820–1827.

[119] F. Grasso, M. Marini, Analysis of hypersonic shock-wave laminar boundary-layer interaction phenomena, Computers & Fluids 25 (1996) 561–581.

[120] M. Marini, Analysis of hypersonic compression ramp laminar flows under sharp leading edge conditions, Aerospace Science and Technology 5 (4) (2001) 257 – 271.

[121] J. P. Davis, B. Sturtevant, Separation length in high-enthalpy shock/boundary-layer interaction, Physics of Fluids 12 (10) (2000) 2661–2687.

[122] N. R. Deepak, S. L. Gai, A. J. Neely, Aerothermodynamics of hypersonic shock wave boundary layer interactions, Proceeding of 17th Australian Fluid Mechanics Conference, Auckland, New Zealand, 2010.

[123] B. John, V. Kulkarni, G. Natarajan, Investigation of ramp-induced shock wave boundary layer interactions in laminar hypersonic flows, International Journal of Heat and Mass Transfer, 70 (2014) 81–90.

[124] B. John, V. Kulkarni, Numerical assessment of correlations for shock wave boundary layer interaction, Computers and Fluids 90 (2014) 42–50.

[125] P. Ashill, J. Fulker, K. Hackett, Research at dera on sub boundary layer vortex generators (sbvgs), 39th Aerospace Sciences Meeting and Exhibit, Reno, Nevada, 2001.

[126] L. J. Souverein, J.-F. Debiève, Effect of air jet vortex generators on a shock wave boundary layer interaction, Experiments in Fluids 49 (5) (2010) 1053–1064.

[127] T. Osuka, E. Erdem, N. Hasegawa, R. Majima, T. Tamba, S. Yokota, A. Sasoh, K. Kontis, Laser energy deposition effectiveness on shock-wave boundary-layer interactions over cylinder-flare combinations, Physics of Fluids 26 (9) (2014) 096103.

[128] E. Erdem, K. Kontis, T. Osuka, R. Majima, T. Tamba, A. Sasoh, Laser energy deposition for shock wave boundary layer control at supersonic speeds, 29th International Symposium on Shock Waves, 2015.

[129] J. C. Townsend, Effects of leading edge bluntness and ramp deflection angle on laminar boundary layer separation in hypersonic flow, NASA TN D-3290, 1966.

[130] M. S. Holden, Boundary-layer displacement and leading-edge bluntness effects on attached and separated laminar boundary layers in a compression corner. part ii: Experimental study, AIAA Journal 9 (1971) 84–93.

[131] J. D. Gray, R. W. Rhudy, Effects of blunting and cooling on separation of laminar supersonic flow, AIAA Journal 11 (9) (1973) 1296–1301.

[132] M. Coët, B. Chanetz, Experiments on shock wave/boundary layer interaction in hypersonic flow, Rech Aerosp (English edition), 1993.

[133] T. Neuenhahn, H. Olivier, Numerical study of wall temperature and entropy layer effects on transitional double wedge shock wave/boundary layer interactions, Shock Waves, Berlin, Heidelberg, 2009.

[134] B. John, S. Surendranath, G. Natarajan, V. Kulkarni, Analysis of dimensionality effect on shock wave boundary layer interaction in laminar hypersonic flows, International Journal of Heat and Fluid Flow 62 (2016) 375 – 385.

[135] B. John, V. Kulkarni, Alterations in critical radii of bluntness of shock wave boundary layer interaction, Journal of Aerospace Engineering 30 (5) (2017) 04017022.

[136] J. E. Lewis, T. Kubota, L. Lees, Experimental investigation of supersonic laminar, two-dimensional boundary-layer separation in a compression corner with and without cooling, AIAA Journal 6 (1) (1968) 7–14.

[137] G. R. Inger, S. Zee, Transonic shockwave/turbulent-boundary-layer interaction with suction or blowing, Journal of Aircraft 15 (11) (1978) 750–754.

[138] K. O. W. Ball, Further results on the effects of suction on boundary-layer separation, AIAA Journal 8 (2) (1970) 374–375.

[139] V. Pasquariello, M. Grilli, S. Hickel, N. A. Adams, Large-eddy simulation of passive shock-wave/boundary-layer interaction control, International Journal of Heat and Fluid Flow 49 (2014) 116–127.

[140] J. Fulker, The Euroshock programme (a European programme on active and passive control of shock waves), 17th Applied Aerodynamics Conference, American Institute of Aeronautics and Astronautics, Norfolk, Virginia, 1999.

[141] B. V. Leer, Flux-vector splitting for the euler equations, 8th International Conference on Numerical Methods in Fluid Dynamics, Achen, Germany, 1982.

[142] M. S. Liou, C. J. Steffen, A new flux splitting scheme, Journal of Computational Physics 107 (1) (1993) 23–39.

[143] M. S. Liou, A sequel to ausm, Journal of Computational Physics 129 (2) (1996) 364–382.

[144] V. V. Rusanov, Calculation of interaction oh non-steady shock waves with obstsacles, Journal of Computational Mathematics and Physics 1 (2) (1961) 267–279.

[145] T. Barth, D. Jespersen, The design and application of upwind schemes on unstructured meshes, AIAA Paper, 89-0366, 1989.

[146] J. Blazek, Computational Fluid Dynamics: Principles and Applications, Elsevier, 2001.

[147] T. Poinsot, S. Lelef, Boundary conditions for direct simulations of compressible viscous flows, Journal of Computational Physics 101 (1) (1992) 104 – 129.

[148] T. R. A. Bussing, E. M. Murman, Finite volume method for the calculation of compressible chemically reacting flows, AIAA Journal 26 (5) (1987) 1070–1078.

[149] W. Sutherland, Lii. the viscosity of gases and molecular force, The London, Edinburgh, and Dublin Philosophical Magazine and Journal of Science 36 (223) (1893) 507–531.

[150] V. W. R Gehre, R. Boyce, Computational investigation of thermal non-equilibrium effects in scramjet engines, Journal of propulsion and Power 29 (3) (2013) 648–660.

[151] R. Starkey, Effect of chemistry modelling modeling on scramjet engine design, 4th AIAA/ASME/SAE/ASEE Joint Propulsion Conference and Exhibit, Reston, VA, 2009.

[152] B. Hassan, G. Candler, D. Olynick, The effect of thermo-chemical non-equilibiurm on the aerodynamics of aerobraking vehicles, Journal of Spacecraft and Rockets 30 (6) (1993) 647–655.

[153] G Candler and D Kelley and S Macheret and M Shneider and I Adamovich, Effects of vibrational excitation, thermal non-uniformities , and unsteady phenomena on supersonic blunt bodies, AIAA Journal 40 (9) (2002) 1803–1810.

[154] A. Viviani, G. Pezzella, C. Golia, Effects of thermochemical modelling and surface catalyticity on an earth re-entry vehicle, Proceedings of the Institution of Mechanical Engineers, Part G: Journal of Aerospace Engineering 225 (5) (2011) 523–540.

[155] J. D. Anderson Jr., Hypersonic and High Temperature Gas Dynamics, McGraw-Hill International Editions, 1989.

[156] S. T. Yu, B. J. Mcbride, K. C. Hsief, J. S. Shuen, A chemical equilibrium method for hypersonic flow simulations, Computers Fluids 23 (1) (1994) 143–155.

[157] J. Yang, Y. Tang, S. Lee, A high order streamline godunov scheme for steady supersonic/hypersonic equilibrium flows, Computer Methods in Applied Mechanics and Engineering 159 (3-4) (1998) 261–289.

[158] J. Vaassen, P. Wautelet, J. Essers, Application of a third order reconstruction scheme to hypersonc reacting flows using unstructured meshes and multigrid techniques, Journal of Computational and Applied Mathematics 168 (1-2) (2004) 481–489.

[159] K. Hejranfar, V. Esfahanian, R. Kamali-Moghadam, Dual code solution procedure for efficient computing equilibrium hypersonic axisymmetric transitional/turbulent flows, Aerospace Science and Technology 21 (1) (2012) 64–74.

[160] U. Riedel, U. Maas, J. Warnatz, Detailed numerical modeling of chemical and thermal non-equilibrium in hypersonic flows, Computer Fluids 22 (2) (1993) 285–294.

[161] D. Giordano, V. Bellucci, G. Colonna, M. Capitelli, I. Armenis, C. Bruno, Vibrationally relaxing flow of n past an infinite cylinder, Journal of Thermophysics and Heat Transfer 11 (1) (1997) 27–35.

[162] G. Colonna, M. Capitelli, The influence of atomic and molecular metastable in high enthalpy nozzle expansion nitrogen flows, Journal of Physics, D: Applied Physics 34 (12) (2001) 1812–1818.

[163] R. Pepe, A. Bonfiglioli, A. D'Angola, G. Colonna, R. Paciorri, Shock-fitting versus shock-capturing modeling of strong shocks in non-equilibrium plasmas, IEEE Transactions on Plasma Science 42 (10) (2014) 2526–2527.

[164] R. Pepe, A. Bonfiglioli, A. D'Angola, G. Colonna, R. Paciorri, An unstructured shock fitting solver for hypersonic plasma flows in chemical non-equilibrium, Computer Physics Communications 196 (2015) 179–193.

[165] G. Colonna, Problems and perspectives of state to state kinetics for high enthalpy plasma flows, 29th International Symposium on Rarefied Gas Dynamics, Melville, NY, 2014.

[166] I. Nompelis, T. Drayna, G. Candler, A parallel unstructured implicit solver for hypersonic reacting flow simulation, 17th AIAA Computational Fluid Dynamics Conference, Reston, VA, 2004.

[167] G. Sarma, Physio-chemical modeling in hypersonic flow simulation, Progress in Aerospace Science 36 (3-4) (2000) 281–349.

[168] B. John, G. Sarath, V. Kulkarni, G. Natarajan, Performance comparison of flux schemes for numerical simulation of high speed inviscid flows, Progress in Computational Fluid Dynamics 14 (2) (2014) 83–96.

[169] J. S. Shuen, Upwind differencing and LU factorization for chemical nonequilibrium navier-stokes equations, Journal of Computational Physics 99 (1992) 233–250.

[170] T. Ji, R. Zhang, B. Sunden, G. Xie, Investigation on thermal performance of high temperature multilayer insulations for hypersonic vehicles under aerodynamic heating condition, Applied Thermal Engineering 70 (1) (2014) 957 – 965.

[171] X. W. Zhu, J. Q. Zhao, Study on helium impingement cooling for a sharp leading edge subject to aerodynamic heating, Applied Thermal Engineering 107 (2016) 253 – 263.

[172] R. Kalimuthu, R. C. Mehta, E. Rathakrishnan, Drag reduction for spike attached to blunt-nosed body at Mach 6, Journal of Spacecraft and Rockets 47 (1) (2010) 219–222.

[173] B. John, V. Kulkarni, Investigation of energy depositon technique for drag reduction at hypersoinc speeds, Applied Mechanics and Materials 90 (367) (2013) 222–227.

[174] E. Josyula, M. Pinney, W. B. Blake, Applications of a counterflow drag reduction-technique in high-speed systems, Journal of Spacecraft and Rockets 39 (4) (2002) 605–614.

[175] V. Menezes, S. Kumar, K. Maruta, K. P. J. Reddy, K. Takayama, Hypersonic flow over a multi-step afterbody, Shock Waves 14 (5) (2005) 421–424.

[176] M. Fujita, Axisymmetric oscillations of an opposing jet from a hemispherical nose, 32nd Aerospace Sciences Meeting and Exhibit, Reno, NV, U.S.A., 1994.

[177] N. Sahoo, V. Kulkarni, S. Saravanan, G. Jagadeesh, K. P. J. Reddy, Film cooling effectiveness on a large angle blunt cone flying at hypersonic speed, Physics of Fluids 17 (3) (2005) 036102.

[178] P. L. O. Thornhill, C. K. Thornhill, The Flow in an Axially-symmetric Supersonic Jet from a Nearly-sonic Orifice Into a Vacuum, Aeronautical Research Council. Reports and Memoranda. no. 2616, 1952.

[179] E. S. Love, C. E. Rigsby, L. P. Lee, M. J. Woodling, Experimental and theoretical studies of axisymmetric free jets, NASA TR, no. R-6, 1959.

[180] E. S. Love, A re-examination of the use of simple concepts for predicting the shape and location of detached shock waves, NACA TN , no. 4170, 1957.

[181] E. S. G. Maciel, A. P. Pimenta, Thermochemical non-equilibrium entry flows in mars in two-dimensions –part i, WSEAS Transactions on Applied and Theoretical Mechanics 8.

[182] K. O. W. Ball, R. H. Korkegi, An investigation of the effect of suction on hypersonic laminar boundary-layer separation, AIAA Journal 6 (2) (1968) 239–243.

[183] J. Délery, Shock wave/turbulent boundary layer interaction and its control, Progress in Aerospace Science 22 (11) (1985) 209–280.

[184] D. C. McCormick, Shock/boundary-layer interaction control with vortex generators and passive cavity, AIAA Journal 31 (1993) 91–96.

[185] J. D. Gray, Nose bluntness effects on axisymmetric laminar reattaching flows at Mach 19, Arnold Engineering Development Center, Tenn, TR-67-16, 1967.

[186] M. S. Holden, Boundary-layer displacement and leading-edge bluntness effects on attached and separated laminar boundary layers in a compression corner. *ii* - experimental study, AIAA Journal 9 (1) (1971) 84–93.

[187] M. Marini, Effects of flow and geometry parameters on shock-wave boundary-layer interaction phenomena, AIAA Paper, (1998) 98–1570.

[188] M. Piotrowicz, P. Flaszyński, Numerical investigations of shock wave interaction with laminar boundary layer on compressor profile, Journal of Physics: Conference Series 760 (1) (2016) 012023.

[189] I. Hataue, Computational study of the shock-wave/boundary-layer interaction in a duct, Fluid Dynamics Research 5 (3) (1989) 217 – 234.

[190] P. Kaczyński, R. Szwaba, Influence of cooling intensity on shock wave boundary layer interaction region in turbine cascade, Journal of Physics: Conference Series 760 (1) (2016) 012007.

[191] D. Thévenin, G. Janiga, Optimization and Computational Fluid Dynamics, Springer Verlag, Berlin, 2008.